

NUREG/CR-0972
SAND79-1542
Vol. 11
R3

Light Water Reactor Safety Research Program Quarterly Report, January-March 1979

Volume 11

Marshall Berman

120555031837 2 ANR3
LS NRC
SECY PUBLIC OCCUPERT ROOM
BRANCH OFFICE 016
PST LUCY
WASHINGTON DocControl EC 20555

Printed December 1979



Sandia Laboratories

Prepared for
U. S. NUCLEAR REGULATORY COMMISSION

8005230428

NOTICE

This report was prepared as an account of work sponsored by an agency of the United States Government. Neither the United States Government nor any agency thereof, or any of their employees, makes any warranty, expressed or implied, or assumes any legal liability or responsibility for any third party's use, or the results of such use, or any information, apparatus, product or process disclosed in this report, or represents that its use by such third party would not infringe privately owned rights.

The views expressed in this report are not necessarily those of the U.S. Nuclear Regulatory Commission.

Available from
National Technical Information Service
Springfield, VA 22161

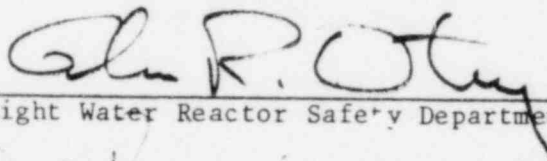
NUREG/CR-0972
SAND79-1542
R3

LIGHT WATER REACTOR SAFETY RESEARCH PROGRAM
QUARTERLY REPORT, JANUARY-MARCH 1979
Vol. 11

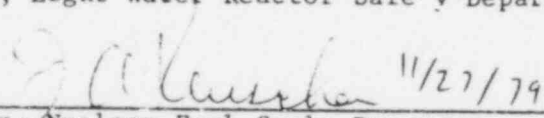
Person in Charge: Marshall Berman

Manuscript Submitted: July 1979
Date Published: December 1979

APPROVED:



Manager, Light Water Reactor Safety Department



Director, Nuclear Fuel Cycle Programs

Sandia Laboratories
Albuquerque, NM 87185
Operated by
Sandia Laboratories
for the
U.S. Department of Energy

Prepared for
Division of Reactor Safety Research
Office of Nuclear Regulatory Research
U.S. Nuclear Regulatory Commission
Washington, DC 20555

Under Interagency Agreement DOE 40-550-75
NRC FIN Nos. A-1019, -1030, -1205, -1207, -1216

CONTENTS

	<u>Page</u>
1. Molten Core/Concrete Interactions Study	11
1.1 Summary	11
1.2 Molten Core/Concrete Interaction Analytical Program	12
1.3 References	15
2. Steam Explosion Phenomena	17
2.1 Summary	17
2.2 Steam Explosion Triggering Phenomena	21
2.3 Open Geometry Tests	30
2.4 Fully Instrumented Test Series	30
2.5 Theoretical Analysis	35
2.6 Assessment of Containment Failure Capability by Steam Explosions	61
2.7 References	73
3. Statistical Analysis	75
3.1 Summary	75
3.2 Statistical Analysis of Blowdown Results	75
3.3 The Metal-Water Reaction	78
3.4 Pin Pressure Initialization	80
3.5 Reproducibility of Calculated Results	85
3.6 TRAC Progress	87
3.7 References	89
4. UHI Model Development	91
4.1 Summary	91
4.2 UHI RELAP Blowdown Calculations	92
4.3 UHI Reflood Calculations	109

CONTENTS (cont)

		<u>Page</u>
4.4	TRAC Progress	113
4.5	References	118
5.	Two-Phase Jet Loads	119
5.1	Summary	119
5.2	Break Flow Results Using TRAC-PIA	120
5.3	Steady-State Technique for Reaction Force	125
5.4	Steady-State TRAC Results for JAERI and KWU Data	126
5.5	Air-Jet Interaction Using CSQ	133
5.6	Proposed Future Work	135
5.7	References	136

ILLUSTRATIONS

<u>Figure</u>		<u>Page</u>
2-1	Peak Pressure as a Function of Water Subcooling for Hematite Starting Material	22
2-2	Peak Pressure as a Function of Water Subcooling for Corium-F Simulant Starting Material	23
2-3	Pressure Trace Recorded During Detonator-Driven Steam Explosion of Arc-Melted Iron Oxide as It Interacted With 20 K Subcooled Water	24
2-4	Laser Heating Arrangement for Single Drop Studies With Molten Prototypical Oxides	25
2-5a	Pressure Transducer Record of Explosion of Single 2.7-mm Diameter Drop of $\text{FeO}_{\approx 1.3}$ in Water	28
2-5b	Horizontal Width of the Bubble Blown During the Explosion of a Single 2.7-mm Diameter Drop of $\text{FeO}_{\approx 1.3}$ in Water	28
2-6	Pendant Drops in Different Atmospheres	29
2-7	Initial Problem Description	33
2-8	Molten Iron Incipient Fragmentation	33
2-9	Molten Iron: Dot Density Proportional to Pressure	34

ILLUSTRATIONS (cont)

		<u>Page</u>
2-10	Phase Diagram of FeO System	39
2-11	Schematic of the Fuel-Melt Interface	41
2-12	Small-Scale Triggering Experiments, Fe ₂ O ₃ * - Bridgewire Pulse Trigger - 0.83 bar	44
2-13	Vapor Film Growth Behavior (Water Temperature Dependence)	48
2-14	Vapor Film Growth Behavior (Ambient Pressure Dependent)	48
2-15	Comparison of the Equilibrium and the Non- equilibrium of Film Boiling Collapse	50
2-16	Vapor Film Pressure Behavior During Collapse	52
2-17	Vapor Film Pressure Behavior During Collapse	53
2-18	The Effect of Ambient Pressure on Taylor Instability Growth	53
2-19a	Numerical Simulation of Hydrodynamic Mercury Water Experiment (Time = 0.0 s)	56
2-19b	Numerical Simulation of Hydrodynamic Mercury Water Experiment (Time = 0.0004 s)	57
2-20	Conceptual View of the Expansion Phase Before Reactor Vessel Head Impact	62
2-21	Schematic of Solid-Vapor Heat Transfer Model	64
2-22	Schematic of Liquid-Vapor Heat Transfer Model	67
2-23	Schematic of Test C-003 Apparatus	68
2-24	Comparison of Model With SRI Experimental Data	69
2-25	Energetic Fuel-Coolant Interaction Expansion Phase	71
3-1	RELAP4 Nodalization for BE/EM Study	77
3-2	Clad Temperature, DS 84, Slab 15	80
3-3	Fuel Stored Energy, Effect of New Pin Pressure Initialization	82
3-4	Lower Plenum Pressure, Effect of New Pin Pressure Initialization	82
3-5	Middle Average Core Flow, Effect of New Pin Pressure Initialization	83
3-6	Temperature in Middle Average Core, Effect of New Pin Pressure Initialization	83

ILLUSTRATIONS (cont)

	<u>Page</u>
3-7 Slab 15 Surface Temperature, Effect of New Pin Pressure Initialization	84
3-8 Slab 14 Surface Temperature, Effect of New Pin Pressure Initialization	84
4-1 UHL, an Upper Head Injection Nodalization Scheme With Azimuthally Noded Downcomer	93
4-2 Midcore Heat Slab Temperature, Effect of Relaxed Quench Criterion	95
4-3 Top Core Slab Temperature, Effect of Relaxed Quench Criterion	95
4-4 Bottom Core Slab Temperature, Effect of Relaxed Quench Criterion	96
4-5 Total Fuel Stored Energy, Effect of Relaxed Quench Criterion	96
4-6 Volume Temperature, Middle Average Core Volume	97
4-7 Liquid Mass, Middle Average Core Volume	97
4-8 Support Column Flow, Effect of Relaxed Quench Criterion	98
4-9 Mass in Upper Head, Effect of Relaxed Quench Criterion	98
4-10 Mass in Upper Volume of Lower Plenum	99
4-11 Mass in Lower Volume of Lower Plenum	99
4-12 Clad Temperature, Bottom of Hot Assembly; Smoothed Westinghouse-Zuber Slip vs Generic Slip, Relaxed Quench Criterion	100
4-13 Midcore Hot Assembly Clad Temperature; Smoothed Westinghouse-Zuber Slip vs Generic Slip, Relaxed Quench Criterion	101
4-14 Top Hot Assembly Clad Temperature; Smoothed Westinghouse-Zuber Slip vs Generic Slip With Relaxed Quench Criterion	102
4-15 Total Fuel Stored Energy; Westinghouse-Zuber Slip vs Generic Slip, Relaxed Quench Criterion	103
4-16 Support Column Flow; Smoothed Westinghouse-Zuber Slip vs Generic Slip, Relaxed Quench Criterion	103

ILLUSTRATIONS (cont)

	<u>Page</u>
4-17 Upper Head Mass; Smoothed Westinghouse-Zuber Slip vs Generic Slip, Relaxed Quench Criterion	104
4-18 Mass in Upper Volume of Lower Plenum; Smoothed Westinghouse-Zuber Slip vs Generic Slip, Relaxed Quench Criterion	104
4-19 Mass in Lower Volume of Lower Plenum; Smoothed Westinghouse-Zuber Slip vs Generic Slip, Relaxed Quench Criterion	105
4-20 Flow at Top of Downcomer, Westinghouse-Zuber Slip vs MOD5 Slip	106
4-21 Flow at Bottom of Downcomer, Westinghouse-Zuber Slip vs MOD5 Slip	106
4-22 Flow Into Top Hot Assembly, Modified Void Fraction, Waterpack on at 10 s	108
4-23 Flow Into Top Hot Assembly, Waterpack on at 2 s	108
4-24 Temperature Transition Strategy	110
4-25 RELAP4/MOD5, FLOOD Nodalization	111
4-26 Lower Plenum to Downcomer (J4) and Lower Plenum to Core (J5) Junction Mass Flows	112
5-1 TRAC Four-Component Model for Initial Blowdown Studies	120
5-2 KWU EXperiment Test Facility	122
5-3 TRAC Break Flow for KWU NW 50, Test 6	123
5-4 TRAC Break Pressure for KWU NW 50, Test 6	123
5-5 TRAC Result for KWU NW 25, Test 3	127
5-6 TRAC Results for KWU NW 25, Test 5	127
5-7 TRAC Results for KWU NW 50, Test 6	128
5-8 TRAC Results for KWU NW 65, Test 3	128
5-9 TRAC Results for KWU NW 65, Test 4	129
5-10 TRAC Comparison to JAERI Data, Test 1	129
5-11 TRAC Comparison to JAERI Data, Test 2	130
5-12 TRAC Comparison to JAERI Data, Test 3	130
5-13 TRAC Comparison to JAERI Data, Test 4	131
5-14 Impingement Target	134
5-15 Effect of Air Density on Plate Pressure	134

TABLES

Table

2-I	Major Experimental Findings	36
2-II	Summary of Known Thermophysical Properties for Iron-Oxygen System	38
2-III	Ambient Pressure Cutoff Results	45
2-IV	Results of Analysis for Dimensionless Breakup Times	60
3-I	Input Variables and Values	76
3-II	Metal-Water Reaction, "Star Points"	79
5-I	Initial Conditions for KWU Tests	121
5-II	TRAC-PLA and KWU Test Comparisons	124
5-III	Coefficients of Resistance for KWU Tests	125
5-IV	Pressure Measurement Location for KWU Tests	132

LIGHT WATER REACTOR SAFETY RESEARCH PROGRAM
QUARTERLY REPORT, JANUARY-MARCH 1979

1. Molten Core/Concrete Interactions Study

1.1 Summary

The Molten Core/Concrete Interactions Study was begun on July 15, 1975 to provide a qualitative, extensive exploration of the phenomena associated with contact between molten-core materials and concrete. The experimental elements of this study are divided into four categories:

- Deposition of corium-type melts onto concrete
- Kinetics and stoichiometry of the thermal decomposition of concrete
- Response of concrete to high heat fluxes at one surface
- Simulation experiments which explore phenomena at the interface between a melt and a decomposing solid

Experimental results are being incorporated in a computer model and a scaling analysis. They will establish scaling parameters for the system and identify key elements of the melt/concrete interaction. A complete project description of the study was issued in October 1975.¹

Efforts during the quarter were devoted primarily to the analytical portion of the program. These activities emphasized phenomenological model development and computer programming for the improved molten core/concrete interaction code, CORCON. The Concrete Ablation and Shape Change (CASC) program developed by ACUREX/Aerotherm Corporation, was completed and delivered to Sandia. The code was made operational on the CDC7600 and checked out using the sample problems provided. Following a detailed examination of the listing, the process of modifying the program and incorporating it into CORCON was begun. Development efforts continued

on several convective heat transfer models and a model describing the anticipated melt/gas chemical reactions.

Programming activities concentrated on implementing the CASC program mentioned above, ancillary efforts included inserting concrete property data into CORCON, and miscellaneous code debugging and clean-up activities. CORCON is approximately 60% completed at this time.

1.2 Molten Core/Concrete Interaction Analytical Program

(J. F. Muir)

Development of the improved core/concrete interaction model, CORCON, continued. CORCON is a user-oriented computer program written in a modular structure in which most computational units are contained in separate subroutines. Maximum use is being made of existing codes and subroutines. Phenomenological models are being developed as required with a heavy reliance on existing techniques, and data and correlations available in the literature. Numerous input options provide a flexibility that enables a variety of problems to be solved by merely changing input data. Efforts during the present quarter concentrated on computer programming and phenomenological model development and implementation.

1.2.1 Phenomenological Model Development (F. G. Blottner, J. F. Muir, and D. A. Powers)

The Concrete Ablation and Shape Change (CASC) program developed by ACUREX/Aerotherm Corporation under contract to Sandia was received in January. This model predicts the growth and shape change of a concrete cavity containing a pool of molten core materials. This is accomplished by using a quasi-steady, one-dimensional concrete ablation model coupled to a two-dimensional axisymmetric shape change procedure. Heat transfer across the pool/concrete interface is described with the use of applicable gas-film models. The Taylor instability model for a horizontal surface^{2 3} is employed along the cavity bottom, up to a local surface inclination angle of 15°, at which point the bubbling of concrete decomposition gases into the pool ceases. At higher surface angles, i.e., around the sides of the pool, the laminar and turbulent continuous gas film heat transfer models

formulated by Bulmer⁴ are used. When coupled together with appropriate transition regions, these models provide a continuous description of the pool/concrete interface heat transfer around the entire periphery of the pool.

Given the initial pool and cavity geometries, the pool, gas, and concrete material properties, and the bulk pool temperatures (three layers), the CASC program provides the surface recession rate and gas evolution rate at each point on the cavity surface, as well as the eroded cavity geometry at the end of each time step.

Work continued on the development of a number of additional phenomenological models required for CORCON including:

1. Convective heat transfer from the periphery of the pool (the pool/concrete interface) to its interior including natural convection and convection augmented by bubble agitation of the pool
2. Convective heat transfer between pool layers (liquid-liquid interfaces) and from the pool surface to the atmosphere above the pool (liquid-gas interface) including natural convection and the enhancement resulting from the passage of gas bubbles across these interfaces
3. Convective heat transfer across the pool/concrete interface in the presence of a film of molten concrete (slag) rather than a gas film*
4. Melt/gas chemical reactions

1.2.2 Programming and Numerical Concerns (L. S. Dike, M. A. Ellis, J. F. Muir, and W. H. Vandevender)

Programming activities during the quarter concentrated on the Concrete Ablation and Shape Change (CASC) program developed by ACUREX.

*Some evidence exists which suggests that a slag film configuration may, under certain conditions, be a more realistic approximation of the melt/concrete interface region than the gas film models. Further experimental investigation is needed to resolve this issue and provide data on the influence of gases bubbling through the slag film on the heat transfer.

The code was brought up on the CDC7600 and checked out by using the sample problems provided. A line-by-line examination of the CASC listing was performed to gain an understanding of the computational details enough to allow the code to be modified for incorporation into CORCON. A number of such modifications have been made and the process of inserting CASC into CORCON initiated. At present this process is about 50% completed.

Thermodynamic properties, specific heat and enthalpy, were provided as functions of temperature by D. A. Powers^{5 6} for the three representative concrete types built into CORCON: LWR basaltic aggregate concrete, LWR limestone aggregate concrete, and CRBR limestone concrete. These, together with the concrete compositions and other material property data were stored in the concrete properties subroutine, CONPRP.

Additional programming efforts were devoted to code debugging and cleanup activities. In its present form, CORCON contains a total of 73 subroutines of which 8 or so will be eliminated. Of the present total, 49% are essentially complete, including most of the major subroutines, 19% need further modifications and/or additions, and the remaining 32% still have to be written. Most of the latter are rather straightforward and the phenomenological models required have, for the most part, been developed.

Work continued on the study of the numerical aspects of INTER and CORCON. The purpose of this study is to identify problem areas in INTER and recommend improved numerical techniques for use in CORCON. Attention during this quarter focused on alternative methods for solving the energy conservation equation for each melt layer and the melt atmosphere to update their respective bulk temperatures each time step. No results are available to report at this time.

1.3 References

- ¹D. A. Powers, Molten Core - Concrete Interactions Project Description, Schedule 189 No. A-1019, (Albuquerque: Sandia Laboratories, Oct 1975).
- ²V. K. Dhir, I. Catton, and J. Castle, "Role of Taylor Instability on Sublimation of a Horizontal Slab of Dry Ice," J. Heat Transfer, 99(3): 411-18 (Aug 1977).
- ³H. Alsmeyer et al, A Model Describing the Interaction of a Coremelt with Concrete, NUREG/TR-0039 (Karlsruhe, West Germany: Kernforschungszentrum [Nuclear Research Center], Oct 1977). Translation of KFK 2395; Sept 1978.
- ⁴B. M. Bulmer, Analytical Study of a Liquid/Vapor/Solid Interface, (Albuquerque: Sandia Laboratories, nd). To be published.
- ⁵D. A. Powers, "Concrete Compositions for the Computer Model CORCON," Light Water Reactor Safety Research Program Quarterly Report October-December, 1978, (Albuquerque: Sandia Laboratories, nd). To be published.
- ⁶D. A. Powers, "Default Concrete for CORCON," (Albuquerque: Sandia Laboratories, nd). Widely circulated but unpublished report; available from the author.

2. Steam Explosion Phenomena

(L. D. Buxton, W. B. Benedick; M. L. Corradini
D. E. Mitchell, L. S. Nelson)

2.1 Summary

The two purposes of the steam explosion phenomena program are: (1) to identify experimentally the characteristics of pressure pulses and other initial conditions which are necessary to trigger and to propagate explosive interactions between water and molten light water reactor (LWR) core materials, and (2) to develop criteria to assess the probability and consequences of steam explosions during a hypothetical meltdown accident in a LWR. The major efforts in this program encompass five areas:

- Small scale experiments using simulant molten materials (Corium-A, -E, iron-oxide $\approx 15/g$) with water. These experiments are performed to understand the applied triggering pressures needed to generate steam explosions under a variety of initial conditions and the propagation of these explosions.
- Large-scale open geometry tests using thermitically generated melts (iron-alumina and U/Zr/55, quantities less than 25 kg) dropped into water. These experiments are primarily directed toward determining the explosive interaction potential of these high temperature melts at large scales, in order that sub-sequent closed geometry tests may be better designed.
- Large-scale closed geometry, fully instrumented tests using induction generated melts (iron-oxides, Corium-E ~ 25 kg) dropped into water. These experiments are to observe, at large scale and with prototypical melts, the

efficiency and propagation of the explosion as a function of fuel and coolant temperatures, mass ratios and compositions.

- Theoretical analysis of steam explosions. This theoretical work is expected to help interpret the observed experimental results in light of past theories and models of steam explosions (vapor explosion) and supply additional modeling effort where past work has proven inadequate. The ultimate objective is to use the experimental and theoretical results to predict the possible behavior of a steam explosion during a meltdown accident.
- Assessment of containment failure resulting from steam explosions. This effort is directed toward evaluating how a steam explosion might lead to containment failure via missile generation or overpressure conditions, and to identify and evaluate the realistic mechanisms that could dissipate the explosion energy and reduce the probability of containment failure.

2.1.1 Small-Scale Experiments

This quarter, effort has been devoted to the analysis and interpretation of data gathered previously in the steam explosion triggering program. The results are summarized in Section 2.2.

Several additional experiments were performed to augment the test matrix defined earlier.¹ In particular, the cutoffs in explosivity with both melt composition and water subcooling were explored further.

In molten iron-oxide, the composition O/Fe = 0.95 (measured at flooding time) was found to be inactive with bridgewire initiation. This extends the inactive compositions below O/Fe = 1.10 and 1.00, determined earlier (see Figure 2.4 in the October-December 1978 Quarterly).

The dependence of explosivity on water subcooling is presented graphically for two melts. The peak pressures generated in the interactions decreased steadily to zero as water subcooling decreased to ≈ 20 K for molten iron-oxide, and ≈ 28 K for Corium-E simulant melt. These experiments were initiated with an exploding submerged bridgewire (peak pressure ≈ 1.0 MPa). The effect of increasing the initiating transients on the explosivity cutoff with water subcooling was also investigated briefly. A minidetector that gave an ≈ 10 -fold greater peak pressure than the bridgewire was used. One of the more vigorous explosions, with a peak pressure of 3.7 MPa, was initiated at ≈ 20 K water subcooling with the minidetector.

Several experiments with alternate coolants were performed. These involved the interaction between molten iron-oxide and two hydrocarbons n-pentadecane and n-heptane. Explosions could not be initiated in either liquid; however, there were chemical reactions which produced metallic-appearing surfaces on the frozen residues.

Scoping experiments were performed to test a new melt/water contact geometry. Single pendant drops of molten oxide, 2.7 mm in diameter, prepared with a continuous wave carbon dioxide laser, were dropped into water. Shortly thereafter, a bridgewire pressure transient was applied to the water. Vigorous explosions were induced in melts of composition $\text{FeO}_{\approx 1.3}$ and Al_2O_3 (one of the components of thermite melts used in the field experiments). Not only is it possible to initiate single drop explosions this way but, by properly measuring photographic images of the pendant drops, densities and surface tensions of the melts can be determined.

2.1.2 Open Geometry Experiments

There is no progress to report on the Corium thermite tests. However, during this quarter L. Buxton prepared and presented a summary of the LWR steam explosion research at Sandia to the 4th CSNI Specialist Meeting on Fuel-Coolant Interactions in Bournemouth, England. The paper was well received.

2.1.3 Fully Instrumented Test Series (FITS)

Work is progressing satisfactorily in this area, and effort this quarter has concentrated on more detailed studies related to experimental design and methodology. Small-scale corium melts using induction heating have been successfully accomplished. A stressed glass cylinder method by which the melt is to be introduced into the water is being studied. Simulation experiments to determine the best way to determine the interaction work output, via slug mass and velocity measurements, are being planned.

2.1.4 Theoretical Analysis

Phenomenological modeling of steam explosions this quarter addressed three areas.

The compositional cutoff of steam explosions observed by Nelson in the triggering experiments was examined in light of the known changes in thermophysical properties of the melt. This analysis resulted in a hypothesis that explosions might be suppressed at high and low oxygen content because the molten sample was forming a solid shell before application of the pressure transient, thereby inhibiting the explosion. This could occur because the melting temperature changes with oxygen content.

The ambient pressure and high water temperature cutoff might have a common explanation; i.e., the vapor film boiling regime separating the melt and the water does not collapse as easily under these conditions with the bridgwire pressure pulse held constant. Thus the observed cutoffs might be eliminated if the trigger pressure increased. The work on this subject has been submitted for the ANS Winter Meeting in San Francisco on November 1979.

The mechanism for fragmentation during the propagation phase is initially being investigated by attempting to model the fragmentation experiments of Theofarous. The analysis entails some theoretical modeling

of the Taylor instability mechanism and numerical modeling of the experiment by using the computer code CSQ. Preliminary results indicate that CSQ can successfully model the experiment for short times ($\sim 20 \mu\text{s}$). Present effort is being placed on trying to extend the calculation to observe the whole fragmentation process.

2.1.5 Assessment of Containment Failure

The dissipation of the coolant vapor energy during the expansion phase of the interaction may be significant. Based upon past work in this area, it was proposed that one energy dissipation mechanism would be heat transfer from the expanding hot coolant vapor to the colder liquid coolant slug above it and to the solid structures. Preliminary results indicate that scaling this heat transfer mechanism up to LWR conditions could provide sufficient heat transfer to reduce the mechanical work output by at least a factor of two. Parts of this work are to be presented at the ANS Annual Meeting in Atlanta on June 6, 1979.

Structural modeling of vessel and containment failure has begun with a preliminary literature search to gain an understanding of the problem and formulate some modeling concepts. Preliminary contacts have been made with P. Cybulskis at Battelle-Columbus and D. Cagliostro at SRI International in order to determine the availability of relevant experiments and analysis.

2.2 Steam Explosion Triggering Phenomena (L. S. Nelson, 5830)

2.2.1 The Compositional Cutoff for Molten Iron-Oxide

It has been indicated in previous quarterly reports that the compositions $\text{O/Fe} = 1.00$ and 1.10 did not explode in the floodable arc-melting apparatus (there were also some inactive melts at $\text{O/Fe} > 1.27$). This inactive region was explored further by studying initial compositions of $\text{O/Fe} = 0.95$. The oxygen analyzer was included in the argon exit line from the arc melter to determine the melt composition at flooding time. The pellet from which the melt was formed used a mixture of hematite and metallic iron of average composition $\text{FeO}_{0.95}$. There was no compositional change upon melting, as evidenced by the absence of oxygen evolved.

Explosions could not be initiated with these melts in room temperature with, using time delays which previously resulted in the most energetic explosions.

2.2.2 The Water Subcooling Cutoffs

In the previous quarterly reports, cutoffs in explosivity with reduced water subcooling were reported for arc-melted hematite and Corium-E simulants of 61.5 initial atom percent oxygen. The subcooling cutoff for hematite was reported to be 24 K, while that of the Corium-E simulant was 31 K, (local boiling point of water = 368 K). Peak pressures, generated in bridgewire-initiated explosive interactions with melts prepared from these two starting materials, are plotted against water subcooling in Figures 2-1 and 2-2. Note that the maximum explosive vigor in the interactions for both melts seems to decrease progressively as water subcooling decreases.

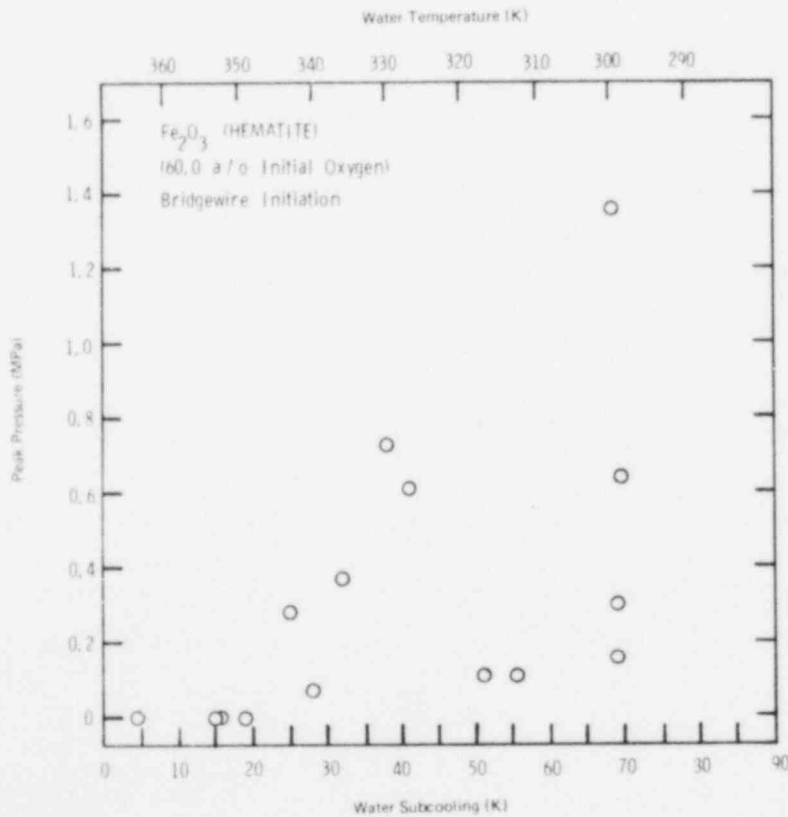


Figure 2-1. Peak Pressure as a Function of Water Subcooling for Hematite Starting Material

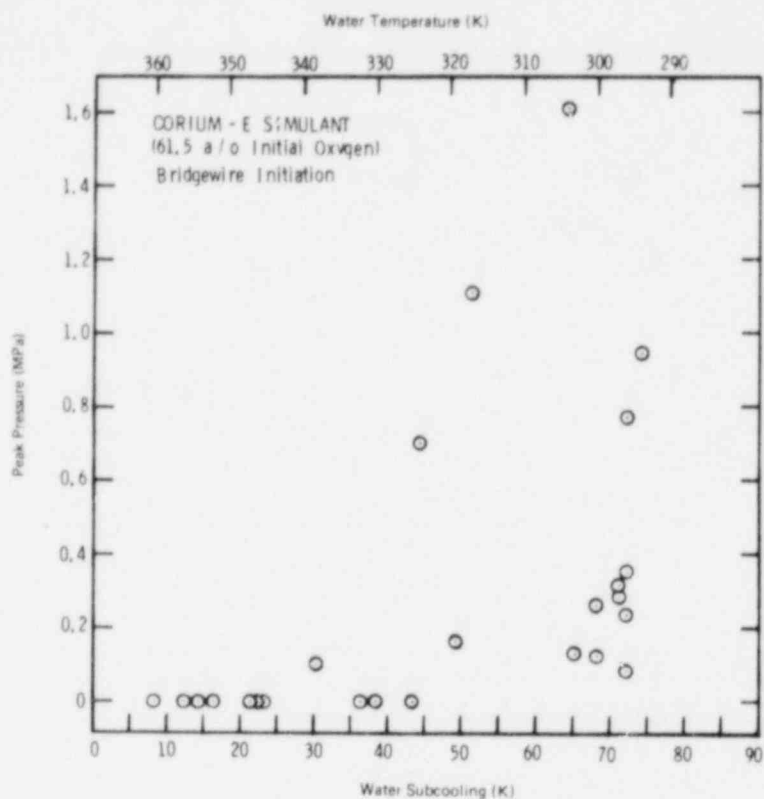


Figure 2-2. Peak Pressure as a Function of Water Subcooling for Corium-E Simulant Starting Material

It is important to know whether the subcooling cutoff phenomenon is sensitive to the magnitude of the pressure transient applied in the aqueous phase during the interaction. In order to test this, several experiments were performed by generating the initiating pressure transient with a minidetector instead of a bridgewire. All other parameters remained the same within the repeatability of the apparatus. It was found that, with the minidetector pulse (peak pressure ≈ 10 MPa), explosions could be initiated in subcooling regions which were hitherto inactive, or at best mildly explosive, with the bridgewire pulse (peak pressure ≈ 1 MPa). For example, explosions were not previously observed in molten iron oxide at 19 K subcooling. However, in experiment 10-139-2 a vigorous explosion (3.8 MPa peak pressure) was initiated at a water subcooling of ~ 20 K using the minidetector; the pressure trace recorded here is shown in Figure 2-3. This is one of the most vigorous explosions ever observed in the entire arc-melting experimental program. The peak pressure in Figure 2-3 should be compared to those shown in Figure 2-1.

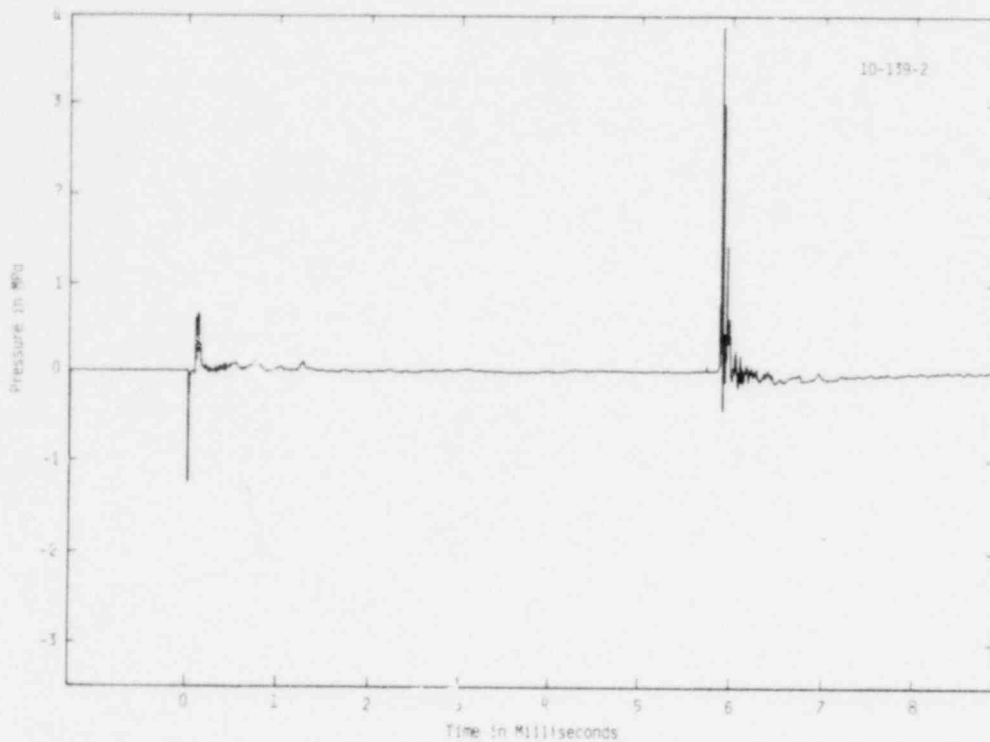


Figure 2-3. Pressure Trace Recorded During Detonator-Driven Steam Explosion of Arc-Melted Iron Oxide as It Interacted With 20 K Subcooled Water. With bridgewire initiation at this subcooling, explosions could not be triggered (cf. Figure 2-1). (10-139-2)

2.2.3 Alternate Coolants

It has been proposed by Epstein et al² that alternate coolants might be used to examine the mechanisms proposed for steam explosion triggering, in particular, gas release-type hypotheses (Epstein,³ Buxton and Nelson⁴). On the basis of the analysis of Epstein et al, n-pentadecane should exhibit bubble dynamic behavior (as measured by the Jacob number) similar to liquid water. This coolant was tried in the floodable arc melter in place of water, using both bridgewire and detonator stimulation. Also, n-heptane, with approximately the same boiling temperature as water was used, but using only bridgewire stimulation. The hot phase for both coolants was molten iron oxide. The most favorable delay times for initiating explosions in water were employed here.

There was no sign of an explosive interaction with either coolant. It appeared, however, that a chemical reaction had occurred at the surface

of the molten oxide in both coolants because of the shiny metallic appearance of the globules after the interaction. It is possible that the hydrocarbon coolants were pyrolyzed during the interaction with the hot molten oxide, generating hydrogen, and other reactive hydrocarbon gases which reduced the oxide to the free metal; perhaps the generation of these gases also stabilized the boiling layer around the molten oxide and thus prevented the explosion.

2.2.4 New Geometries and Heating Techniques

Scoping experiments were initiated to explore new melting techniques and contact geometries; the objective is to obtain more readily interpretable information about steam explosion phenomena than can be obtained with the floodable arc-melting apparatus.

A few experiments were performed this quarter using a continuous wave carbon dioxide laser of approximately 200-W-beam power to prepare pendant drops of two prototypical oxide compositions for insertion into liquid water. The experimental arrangement is shown in Figure 2-4 (for basic techniques, see Nelson et al⁵).

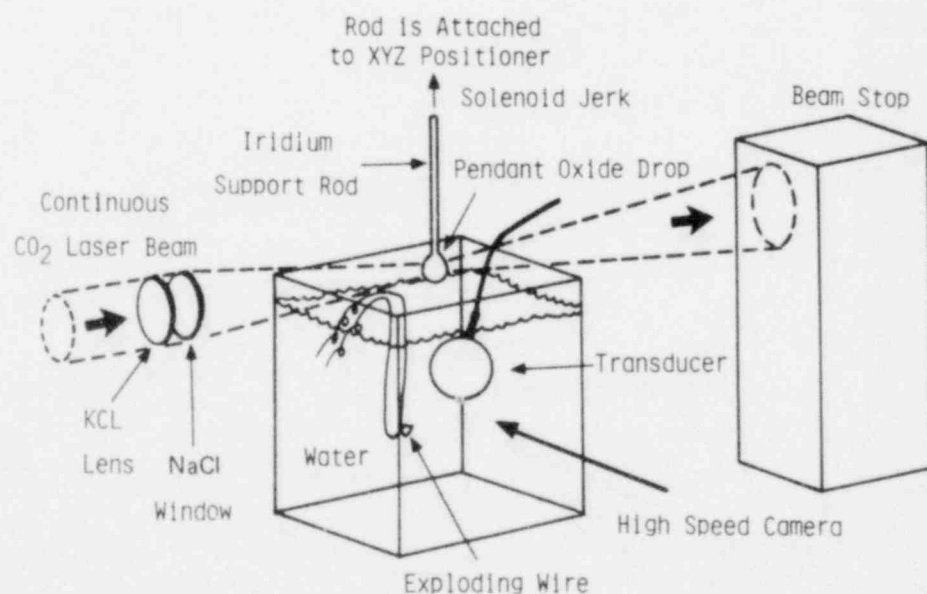


Figure 2-4. Laser Heating Arrangement for Single Drop Studies With Molten Prototypical Oxides

Pendant drops of molten iron oxide or aluminum oxide were prepared in air. The iron oxide drops were supported on a vertical iridium wire, while the aluminum oxide drops were supported on a single crystal sapphire fiber; both supports were 250 μm in diameter. In each case, the upper end of the support was held in a small chuck attached to a solenoid that has a vertically upward stroke. The solenoid, in turn, was attached to a three-dimensional positioner, used to place the drop accurately in the laser focus. After reaching an appropriate temperature, as indicated by the Iron optical pyrometer, the drop was detached from the support by a quick, upward tug of the solenoid, causing the drop to fall several centimeters through air into the water. Shortly after entering the water, the interacting drop could be subjected to a pressure transient generated by the electrical explosion of a submerged bridgewire. Diagnostics used were: (1) high speed cinematography (3000 to 5000 ft/s); (2) a lithium niobate pressure gage suspended in the water, with output recorded on a digital oscilloscope; (3) optical pyrometry; and, (4) debris analysis.

When 2.0- to 2.7-mm-diameter drops of either molten iron oxide ($\text{FeO}_{\approx 1.3}$),* or aluminum oxide (Al_2O_3)** were allowed to fall into water at room temperature, they exploded readily when the interval between drop release and explosion of the bridgewire was ≈ 120 ms. Without the initiating pressure pulse, only a slight jetting of the melt occurred.

In the films, the drops of both compositions initially seemed to have a thin (<1 mm) boiling layer around them just after entering the

*The composition $\text{FeO}_{1.3}$ is determined from the phase diagram of the C-Fe system. Note that this composition lies in a region more oxygen-rich than the upper compositional cutoff for explosions with the floodable arc-melting apparatus (see Figure 2-5 in SAND79-0820).

**Aluminum oxide may well be the material of highest melting temperature (2327 K) which has been induced to explode in a steam explosion-type interaction to date. Also, it should be noted that the liberation of gaseous oxygen internally within the melt by aluminum oxide is not anticipated, as it might be in the interaction of the decomposable iron or cobalt oxides, as suggested previously.

water. There was little disturbance of either drop or water upon entry. When the bridgewire fired, a vigorous interaction occurred with the water; both bridgewire explosion and the interaction usually appeared in the same frame of the film (frame duration $\approx 200 \mu\text{s}$). In room temperature water, a bubble repeatedly grew and collapsed three or four times, depositing debris in the water with each cycle. In several films, incandescent debris particles could be seen at the growing bubble front.

Several oscilloscope records were made of the lithium niobate gage output ($\approx 2 \text{ cm}$ distant) during the interactions. One of those, recorded for a $\text{FeO}_{\approx 1.3}$ drop, is shown in Figure 2-5a; the frame-by-frame horizontal diameters of the bubbles, plotted on the same time scale, are shown in Figure 2-5b. Note that the pressure peaks correspond closely to the onset of rapid outward growth of the bubbles. A similar bubble growth pattern, but smaller in magnitude, was observed for the aluminum oxide drops.

A quick survey was made of the effect of water temperature on the single drop interactions. For 2.7-mm-diameter drops of $\text{FeO}_{\approx 1.3}$, the bridgewire impulse triggered vigorous explosions of the drops in room temperature and 308-K water, and a fairly mild interaction in 313-K water; explosions could not be triggered in either 345-K or 362-K water. These were single experiments, and should be regarded only as preliminary data points at this time.

A quick survey was also made of several photographic pendant drop images, in an attempt to determine surface tension and density. A pendant drop of $\text{FeO}_{\approx 1.3}$ was prepared in air and photographed. Then the atmosphere around the same drop, still molten, was changed to argon in which the composition would be expected to change to $\text{FeO}_{\approx 1.0}$; a second photograph of the drop was recorded. These photographs are reproduced in Figures 2-6a and 2-6b. It can be seen that the drop shapes are different in the two atmospheres indicating different surface tensions in the two melts. The shapes can be related to both the surface tensions (Fordham,⁶ Stauffer⁷) and densities of the melts.

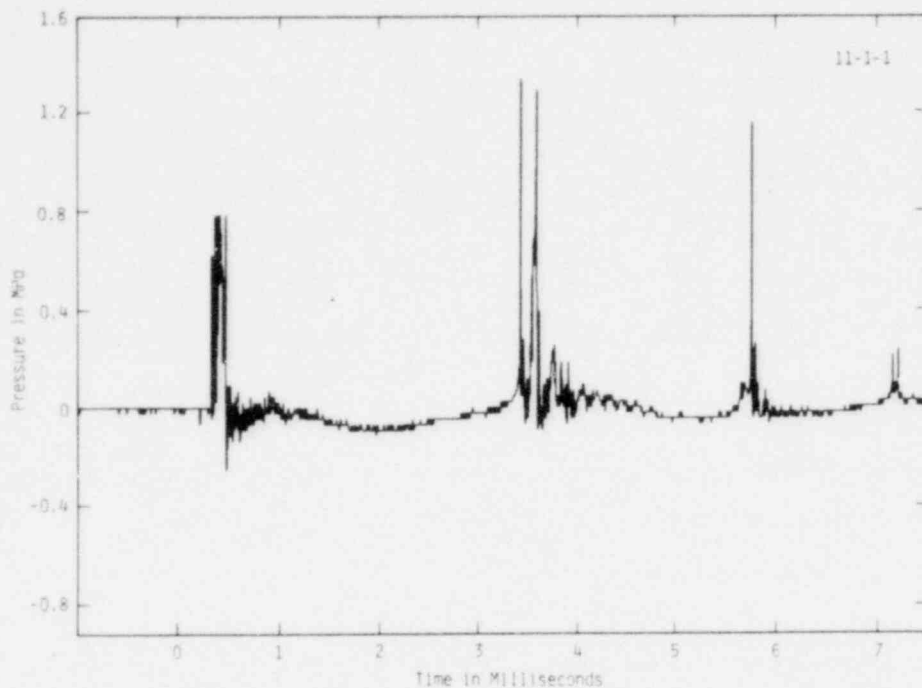


Figure 2-5a. Pressure Transducer Record of Explosion of Single 2.7-mm-Diameter Drop of $\text{FeO}_{\approx 1.3}$ in Water. Bridgewire pulse used to initiate the interaction is about $50 \mu\text{s}$ wide at time zero. Lithium niobate gage was $\approx 2 \text{ cm}$ from the explosion.

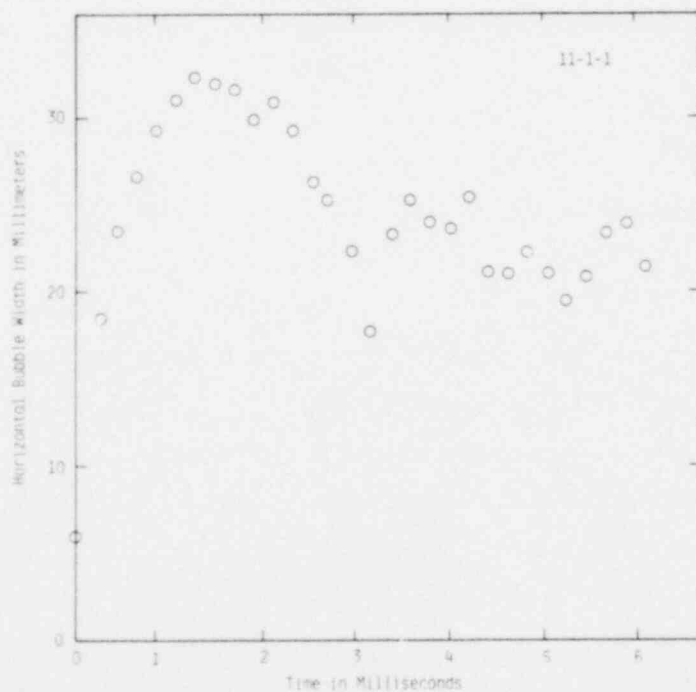
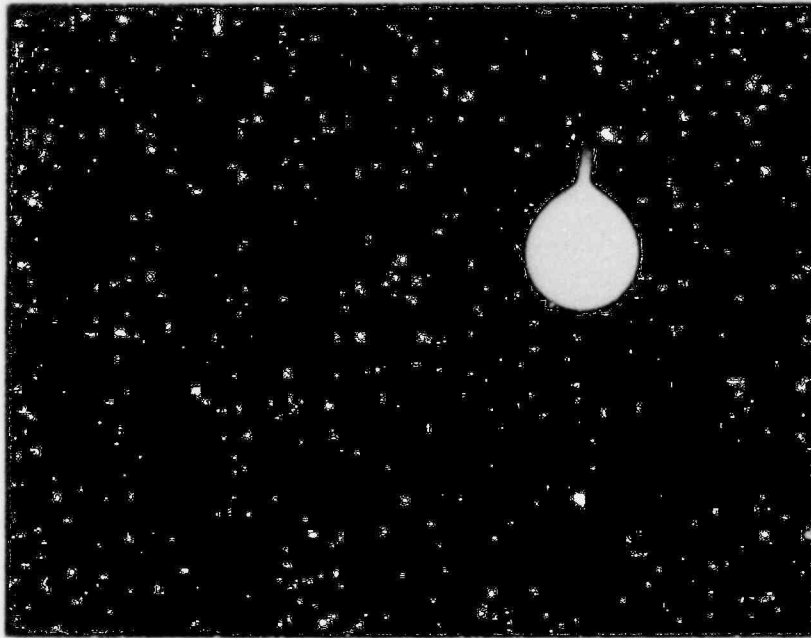
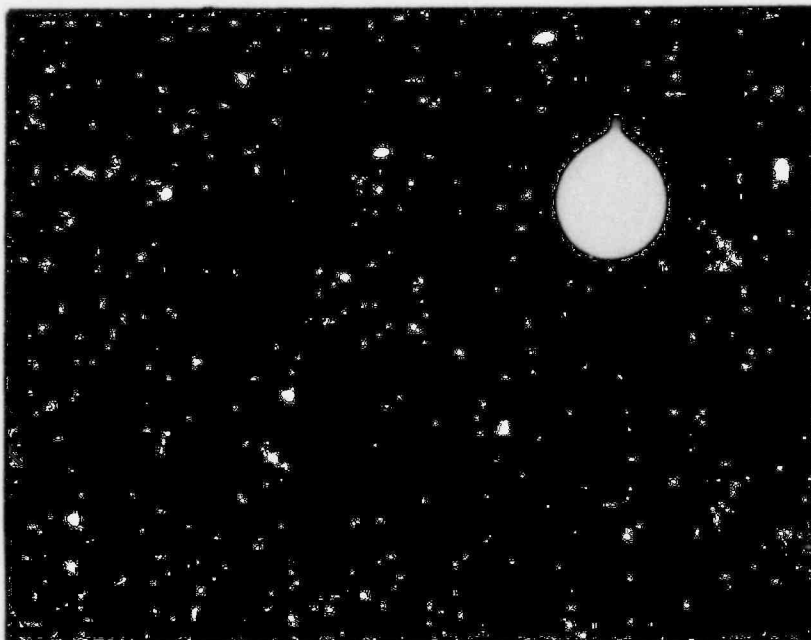


Figure 2-5b. Horizontal Width of the Bubble Blown During the Explosion of a Single 2.7-mm-Diameter Drop of $\text{FeO}_{\approx 1.3}$ in Water. Note that rapid bubble growth coincides with pressure peaks shown in Figure 5a.



a. Air



b. Argon

Figure 2-6. Pendant Drops in Different Atmospheres

The ability to obtain high resolution optical, time and pressure information from the interaction of small quantities of melt of known mass, composition, temperature, and geometry with water is expected to assist significantly in the modeling of steam explosion triggering and propagation phenomena. Preliminary efforts along these lines are underway (see Section 2.5).

2.3 Open Geometry Tests (L. D. Buxton)

There is no progress to report for this quarter.

2.4 Fully Instrumented Test Series (D. E. Mitchell, P. J. Langdon, A. A. Heckes, J. E. Kennedy, C. M. Korbin, M. Elifritz)

The fully instrumented test series (FITS) subtask was divided into six major areas: Interaction Chamber, Melt Generation, Instrumentation, Site Preparation, Analysis and Modeling, and Experiment Design. Work is progressing satisfactorily in all these major areas, and the effort this quarter has concentrated on more detailed studies related to experiment design and methodology. Small-scale corium melts are being prepared, melt drop experiments are being designed, and the method by which the melt is to be introduced into the water is being studied. Simulation experiments to determine the best way to measure slug velocity and mass are also being planned. Progress in each of these areas is discussed in more detail below.

2.4.1 Interaction Chamber (Portupine)

Final drawings are being prepared for the interaction section of the experimental chamber. These are scheduled to be completed early next quarter. After review, procurement procedures will begin. Contacts with potential vendors of the chamber indicate that it could be delivered three months after receipt of an order.

The high speed closure door required to isolate the interaction section from the melting section is undergoing testing to determine

closure times and performance. This device (or a similar type) will be mounted on the top flange of the main chamber.

2.4.2 Melt Generation

Two types of metallic coriums, A and E, were melted and analyzed. The 100-g melts were prepared with a furnace and power supply identical to those to be used in the FITS experiments. Graphite crucibles were used, and it was found that the carbon reduces the uranium oxide (UO_2) to uranium carbide (UC).

The melts produced were homogeneous. The experiments are being done primarily to gain familiarity with induction melting and to determine the degree of melt homogeneity which can be achieved with the induction method. The reduction of UO_2 to UC is not desirable, and other crucible materials are being investigated. However, a graphite susceptor will be required to melt most of the compositions to be used in the actual experiments.

Dropping experiments are being set up at Sandia's Building 9939 in Area Y to study the feasibility of various melt delivery methods. Hardware to begin these tests is on order and this work should begin early next quarter.

2.4.3 Instrumentation

Purchase orders have been placed for signal conditioners, amplifiers, pressure transducers, and a wide band instrumentation tape recorder. The instrumentation is such that a wide range of sensor types can be accommodated.

2.4.4 Site Preparation

Site plans are scheduled to be completed early next quarter. After review, contracts for construction will be placed.

2.4.5 Analysis and Modeling

Currently two types of calculations are being pursued with wave-propagation codes. The first is a study to assess the applicability of these codes to describe the fragmentation process. The second is to aid in determining the types of information contained in pressure and temperature records that will be obtained during the experiments.

The two-dimensional Eulerian code CSQII has been used to simulate a molten iron droplet surrounded by a stable vapor film which is subjected to a transient pressure pulse. Figure 2-7 shows the initial problem definition. This figure is a material-density plot of a 10-mm-diameter molten iron droplet at 2000 K, surrounded by a 1-mm-thick steam film at 1-atm pressure. The drop is imbedded in water at 373 K. A 4.2-kbar transient pressure pulse is supplied to the system to collapse the vapor film. A pulse of this amplitude is required to ensure that the film will collapse against the iron drop in the time scale of 20 μ s.

Figure 2-8 shows the problem at approximately 16 μ s after the pressure wave has impacted the drop. This figure is also a material-density plot and shows that the drop has undergone significant deformation and surface instabilities of both Taylor and Helmholtz types are beginning to form. Figure 2-9 is a pressure-density plot of the same problem. The high density regions correspond to pressures in excess of 10 kbar which have been generated by the interaction of the molten iron and saturated water. The pressures inside the droplet are felt to be of sufficient magnitude to break up the drop either by cavitation or hydrodynamic instabilities. From these preliminary calculations, it appears that CSQII can be used to calculate droplet fragmentation. However, the fragmentation process whereby surface areas are increased by a few orders of magnitude is probably outside the resolution of this calculational method since extremely fine zoning would be required. Coarse fragmentation, which could be responsible for the first pressure pulse observed by Nelson, can be treated by using this code. This work is just beginning, and further study of this part of the problem is planned.

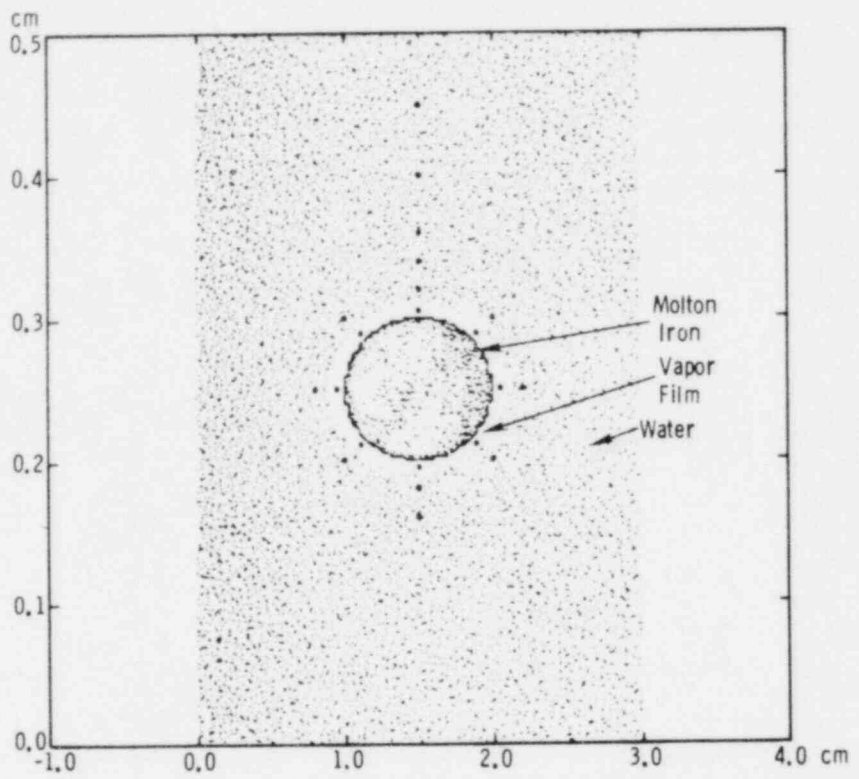


Figure 2-7. Initial Problem Description

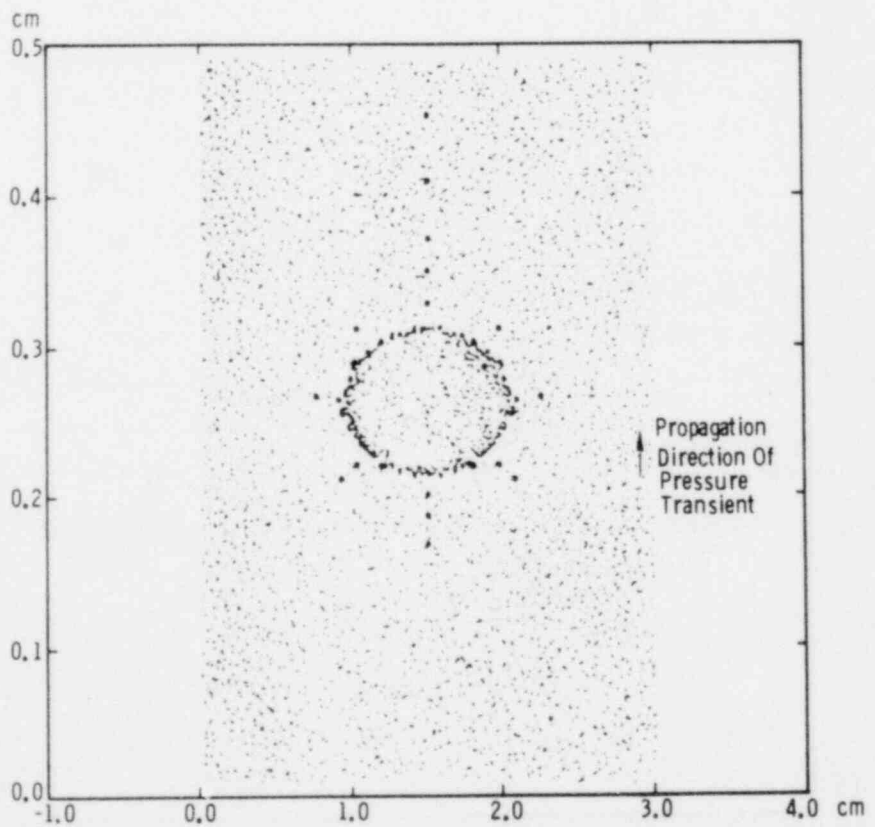


Figure 2-8. Molten Iron Incipient Fragmentation

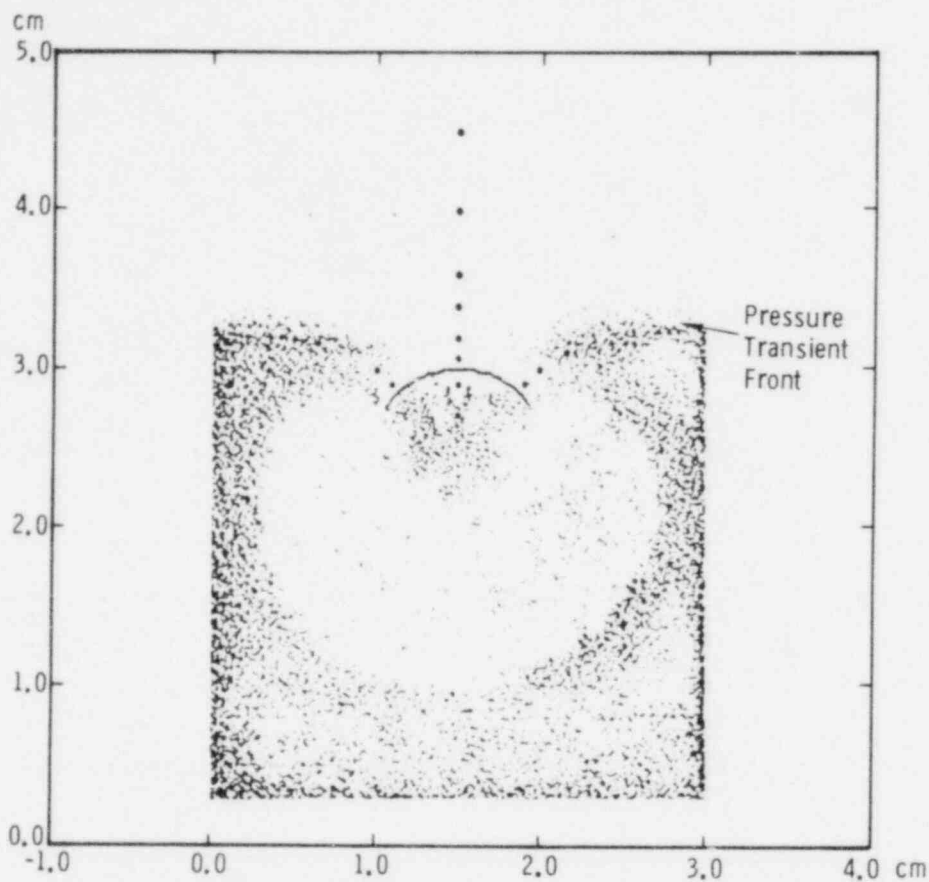


Figure 2-9. Molten Iron: Dot Density Proportional to Pressure

A one-dimensional Lagrangian wave code, Chart D, is also being used to study the interaction. In this work, the molten iron is neglected and energy is being deposited in water at various rates to determine the effect of deposition rate and profile on wave propagation in the coolant medium. The motivation for these numerical experiments is to determine if information on energy deposition rate is contained in the pressure and temperature data which will be obtained in the experiments.

2.4.6 Experiment Design

The data obtained from the experiments are intended to determine the quantity of reactants and the thermal-to-mechanical energy conversion efficiency. Currently, the experiments are being designed so that the amount of molten material in the water prior to interaction is known.

A stressed glass cylinder is being used to allow the melt to be delivered below the surface of the water. Contact of the free-falling melt with the glass cylinder in the water produces a thermal shock which fragments the glass allowing the surrounding water to engulf the melt. Experiments with small (approx 1-kg size) stressed glass cylinders have been done and indicate that the technique may be useful. The fracture rate of the glass is on the order of 2 mm/ μ s, and the pressure disturbance produced by glass fracturing is negligible. The glass fragments are typically on the order a mm or less. Glass fragmentation for these experiments was mechanically activated, and future experiments are planned using small quantities of molten metals. Purchase orders have been written to procure glass cylinders large enough to accept melts of 25-kg size.

Determination of the mechanical work resulting from the interactions requires the measurement of the velocity and mass of the coolant slug. Three methods are being considered, and simulation experiments are being planned to determine the best way of measuring these quantities.

2.5 Theoretical Analysis (Michael Corradini)

2.5.1 Triggering Experiments

The experimental results of the small scale steam explosion experiments have been reported by Nelson and Buxton¹ and are briefly summarized in Table 2-I. The purpose of this portion of the steam explosion research is to analyze the experimental results in light of existing theories and propose new models or concepts where these theories are deficient.

TABLE 2-I

Major Experimental Findings¹

Melt Composition

- Corium-A (U-rich) is very difficult to trigger (1 time in 40 experiments) but occasionally shows spontaneous coarse fragmentation (3 times).
- Corium-E (Fe-rich) triggers easily.
- FeO_x closely simulated Corium-E behavior and has an extensive literature base.
- Explosivity of both Corium-E and FeO_x fall to zero as initial oxygen content of melt decreases.

Applied Press. Transient

- Need only small transient (≈ 1 MPa) to initiate explosion.
- Larger magnitude transient (≈ 10 MPa) breaks up melt, but does not trigger inactive melts.
- Transient applied through the hearth has never initiated explosions.

Subcooling

- Explosions cannot be triggered with 1.0 MPa pulses at subcoolings less than:
 - 31 K for Corium-E
 - 24 K for FeO_x

Ambient Pressure

- Corium-E and FeO_x with high initial oxygen contents explode unchanged up to 0.5 MPa; same material could not be triggered at 0.75 or 1.0 MPa. As pressure increases, successful triggering required longer times between flooding and application of initiating transient.

2.5.1.1 Effects of the Melt Composition on Steam Explosions

Steam explosions appear to be eliminated in the arc melter apparatus if the oxygen content of the iron-oxide at the time of melting falls outside of certain limits of O/Fe ratios (explosion occurs only if

1.0 < O/Fe < 1.26). This same behavior occurs for the Corium-E system (<56% oxygen).

In the last quarterly report it was suggested, based on conservative analyses, that the impulse initiated gas release mechanism may not be the dominant fragmentation mechanism which drives the steam explosion. Rather, another avenue of analyses suggested that the compositional cutoff may be due to a change in the thermophysical properties of the melt with oxygen content. A simple explanation of the observed cutoff is now presented based upon this second hypothesis.

A summary of the known thermophysical properties for the iron-oxygen system is given in Table 2-II. The most notable changes in the properties are for the surface tension and to a lesser extent the density. In addition, the phase diagram of the Fe-O system (Figure 2-10) indicates that the melting temperature decreases by approximately 175°C in the range $1.05 \leq O/Fe < 1.25$. The final point to mention is that the initial temperature of the iron-oxide (T_{I_f}) or Corium-E melts is only slightly above the solidus temperature line ($1900 \text{ K} \leq T_{I_f} < 2000 \text{ K}$). If all these facts are considered together, another explanation for the compositional cutoff could be advanced. The depression in melting temperature values corresponds quite well to the range of O/Fe ratios where explosions are observed. This would suggest that the explosion may become inhibited if the melt sample cools, before the bridgewire pulse is applied, to a point where a solid skin inhibits the fragmentation-heat transfer interaction. This would occur at both high and low O/Fe ratios where T_m is highest. At low ratios of O/Fe (i.e., <1.0), the interaction would be further retarded because the density and surface tension increase would increase the inertia of the melt and the resistance to fragmentation via film boiling destabilization. At high ratios of O/Fe (e.g., >1.26), the interaction may be further retarded by residual oxygen diffusing out of the melt acting as a cushion retarding film collapse. This oxygen is due to the usually high initial O/Fe ratios (~1.5) used. W. Nelson has suggested this behavior for other melts.⁸

TABLE 2-II

Summary of Known Thermophysical Properties
for Iron-Oxygen System

	<u>Fe</u>	<u>FeO</u>	<u>Fe₃O₄</u>	<u>Fe₂O₃</u>
O/Fe Ratio	0	1.00	1.33	1.50
$K \left(\frac{\omega}{m \cdot K} \right)$	37.6 (@ 1810 K)	--	10 (@ 300 K)	12 (@ 300 K)
$\rho \left(\frac{kg}{m^3} \right)$	6770 (@ 1810 K)	4500 (@ 1800 K)	3700 (@ 1850 K)	3600 (@ 1850 K)
$C_p \left(\frac{\omega - S}{kg \cdot K} \right)$	794 (@ 1810 K)	--	862 (@ 1850 K)	906 (@ 1850 K)
$\sigma \left(\frac{nt}{m} \right)$	1.0 (@ 1800 K)	0.7 (@ 1800 K)	0.5 (@ 1850 K)	0.5 (@ 1850 K)
$\mu \left(\frac{kg}{m \cdot s} \right)$	--	--	--	--
$T_{melt} (K)$	1810	1810	1850	1850

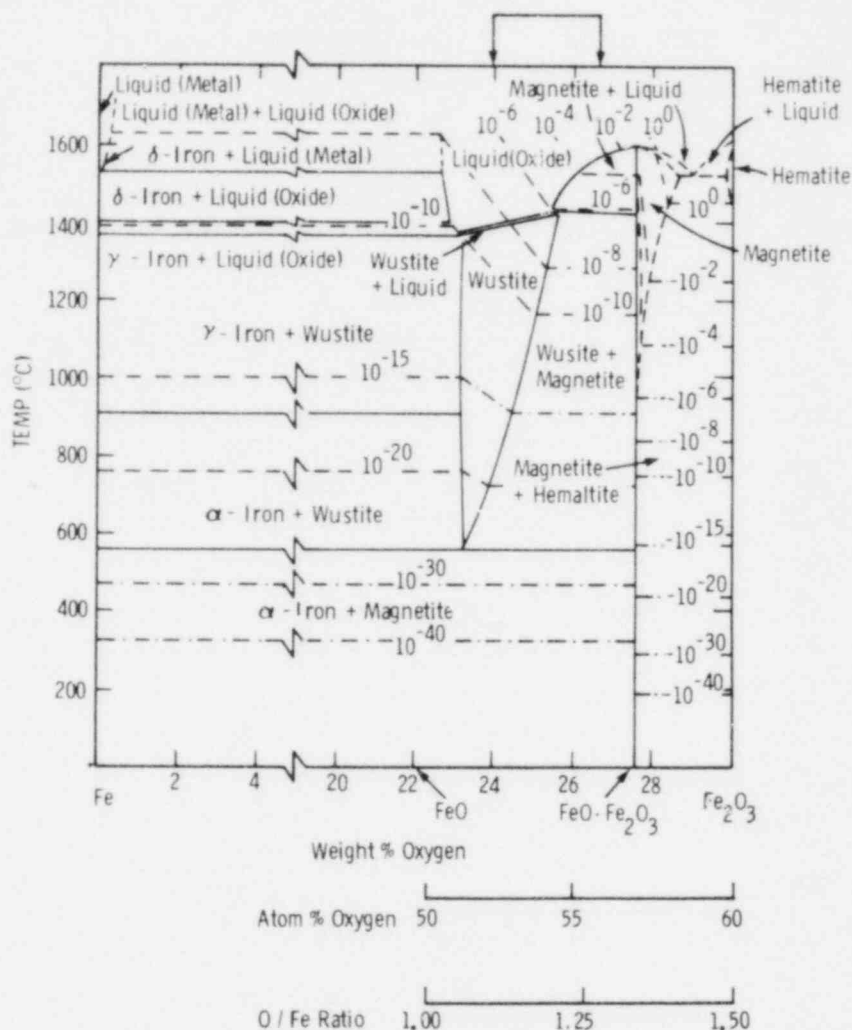


Figure 2-10. Phase Diagram of FeO System

To assess the likelihood of this hypothesis, a cooling analysis was performed for the molten iron-oxide after the arc melter has been turned off but before bridgewire pulse application. If the cooling of the sample is large enough to indicate that the temperature is near or below T_{melt} , then this reasoning may be valid for explaining the compositional cutoff.

After the arc melter is turned off but before bridgewire pulse application, transient heat transfer occurs between the hot melt and the surroundings. There are three dissipative mechanisms: (1) conduction to the water-cooled copper hearth, (2) radiation to solid surfaces and the

water, (3) and convection to the surrounding argon before flooding and to the water after flooding. To accurately model this situation requires a precise knowledge of the initial conditions before the arc is turned off as well as the use of a three-dimensional conduction heat transfer model. Because the initial conditions are not well known, this method of analysis does not seem useful at this point.

Rather, a simple cooling analysis is performed where the molten iron-oxide is modeled as a semi-infinite body (see Figure 2-11) at an initially uniform temperature (T_i). The heat transfer to the copper hearth is not accurately known during the experiment, therefore it will be neglected, realizing that the fuel cooling rate will be underestimated. The heat flux (\dot{q}_r'') due to radiation transport is modeled as

$$\dot{q}_r'' = \sigma_r T_{fs}^4 = h_r(T_{fs} - T_{sat}) \quad (1)$$

where

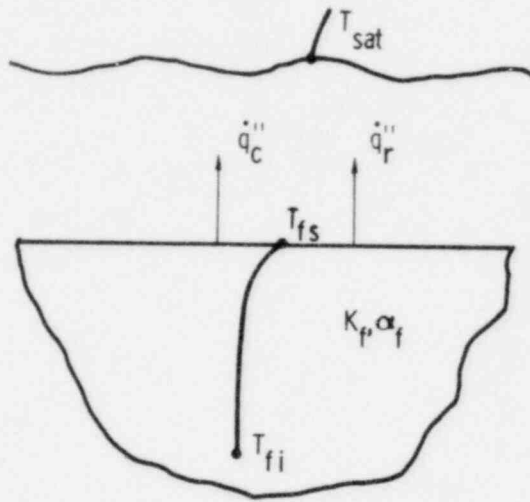
$$h_r = \left(\frac{\sigma_r T_{fs}^4}{T_{fs} - T_{sat}} \right) \quad (2)$$

and where T_{fs} and T_{sat} are the fuel surface temperature and water temperature, respectively, where σ_r is the Stephan-Boltzmann constant and the emissivity is assumed to be one. For molten oxides this is a good assumption.⁹ The convective heat transfer is more complicated, because before flooding it is natural convection from the molten oxide ($Nu_{NC} = 2 + 0.45 (G_r P_r)^{1/4}$) and after flooding film boiling has been established.¹⁰ The heat transfer coefficient varies between the steady conduction value

$$h_C = \frac{K_V}{D} Nu_{NC} = 100 \text{ /m}^2 \text{ K} \quad (3)$$

($K_V = 0.1 \text{ W/m K}$, $D = 1 \text{ cm}$)

to the film boiling value as modeled by Bromley⁹



$$\dot{q}_{\text{TOTAL}}'' = \dot{q}_r'' + \dot{q}_c'' \doteq h_{\text{TOTAL}} (T_{fs} - T_{\text{sat}})$$

$$h_{\text{TOTAL}} = h_r + h_c$$

$$h_r = \frac{\sigma_r T_{fs}^4}{(T_{fs} - T_{\text{sat}})}$$

$$h_c = K_V / \delta$$

$$\dot{q}'' = \text{heat flux } (\omega/\text{m}^2)$$

Figure 2-11. Schematic of the Fuel-Melt Interface

$$h_C = \frac{K_V}{\delta} = 160 \omega/\text{m}^2 \text{ K} \quad (4)$$

where

$$\delta = 0.6 \left[\frac{\lambda_C \mu_V (T_{fs} - T_{\text{sat}}) K_V}{g(\rho_f - \rho_V) \rho_V h_{fg}} \right]^{1/4} \quad (5)$$

where μ_V , K_V , ρ_V are the viscosity, thermal conductivity, and density of the vapor. ρ_l is the liquid, h_{fg} is the latent heat of vaporization and λ_C is the critical Taylor instability wavelength given by

$$\lambda_C = 2\pi \sqrt{\frac{\sigma}{g(\rho_l - \rho_V)}} \quad (6)$$

where σ = surface tension.

How the heat transfer coefficient changes during the flooding process is unknown; thus it is assumed that $h_C = 130 \omega/m^2 K$. The temperature at the surface of the melt is given by.¹¹

$$T_{fs} = T_{sat} + (T_{fi} - T_{sat}) e^{\left(\frac{h_T}{k_f}\right)^2 \alpha_{ft}} \left[1 - \operatorname{erf}\left(\frac{h_r}{k_f} \sqrt{\alpha_{ft}}\right) \right]. \quad (7)$$

Therefore, for a reasonable range of flooding times (0.2 to 1.0 s), the surface temperature changes from $T_{fi} \approx 1900 K$ to

$$T_{fs} = 1800 K @ t = 0.2 s$$

$$T_{fs} = 1710 K @ t = 1.0 s$$

These values are near or below the solidus temperature for the molten oxides with O/Fe ratios less than 1.05 or greater than 1.3. This estimate coupled with the fact that the calculation underestimates the cooling rate by neglecting hearth cooling suggests that a solid shell might exist on the surface of the melt for high or low O/Fe ratios. This shell, in conjunction with the effects of density and surface tension changes, may be the reason explosions are suppressed outside the range $1.0 < O/Fe < 1.26$. Only in this range is the melt superheated enough above

T_m that a solid shell might not form. The explosion insensitivity to the size of the applied pressure pulse¹ may be also explained by this hypothesis. The applied pressure pulse only serves to accelerate the liquid-vapor interface toward the melt surface. Thus the higher applied pressure may not be able to penetrate the solid shell and create new surface area for heat transfer. Further analysis of the experiment considering this hypothesis is under way.

Recent experiments by Nelson might support this hypothesis. A small iron-oxide sample ($m \approx 0.1$ g, $O/Fe = 1.3$) was melted by a CO_2 laser heating technique and raised to a much higher initial temperature (~ 2350 K). It was then dropped into water and a bridgewire pulse 0.1 s later produced a vapor explosion ($P_{peak} \approx 3.1$ MPa @ 2-cm distance). This sample was outside the explosive limits of O/Fe ratio seen in the arc melter experiments and the initial melt temperature was the only variable changed.

2.5.2 Water Subcooling and Ambient Pressure Effects on Steam Explosions

When the water temperature was raised (subcooling lowered) to 60-70°C the steam explosion second stage pressure pulse was inhibited for the Corium-E and iron-oxide melts using bridgewire pulse stimulation. As the temperature was raised further the first stage of the interaction could also be suppressed (Figure 2-12). Nelson has suggested¹ that the pressure pulse is less effective in collapsing the film and triggering the interaction at high water temperatures because the film boiling regime is more stable.

When the ambient pressure was raised from 0.1 MPa to 0.5 to 0.75 MPa, the two-stage interaction was suppressed for bridgewire pulses for both Corium-E and iron-oxide melts (Table 2-III). When minidetectors were used at high pressure, the detonators misfired due to water leakage and only one explosion was observed at 0.5 MPa (Table 2-III). A high pressure cutoff for steam explosions has been proposed by Henry.^{12 13} This upper limit is based on the concept that the propagation phase of the

interaction is tightly coupled to the vapor growth characteristics of the coolant, which are significantly affected by the ambient pressure. These same dynamic characteristics are involved in the triggering phase of the interaction for vapor collapse. Thus it is unclear which phase of the interaction is suppressing the vapor explosion. If it is indeed the propagation phase, then this would suggest an inherent safety benefit for high pressure environments, for regardless of trigger magnitude vapor explosions would not occur. Conversely, if the trigger phase is partially affected by these dynamic vapor characteristics, then this suggests only a more energetic trigger is needed to initiate vapor explosions at higher ambient pressures.

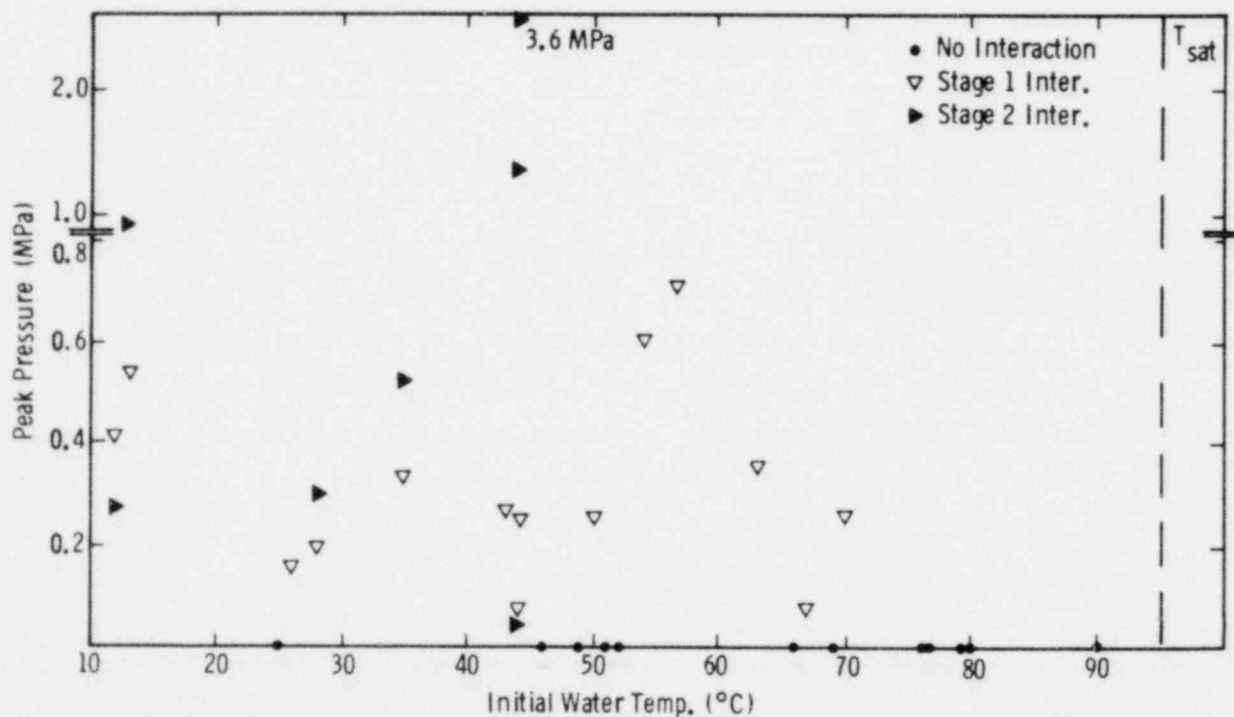


Figure 2-12. Small-Scale Triggering Experiments, Fe_2O_3^* - Bridgewire Pulse Trigger - 0.83 bar. Similar behavior for Corium-E; cut off both stages at 64°F.

TABLE 2-III¹

Ambient Pressure Cutoff Results

Material	P_{∞} (MPa)	Pressure Generator	P_2^a (MPa)	P_{melt}^b (MPa)	Results
1.0 Oxidic Corium-E; 8 Tests	0.2	Bridgewire @3 kV @20 μ s	0.81 (average)	0.31	2 fine fragments; 2 coarse fragments 4 single pieces; caldera formed
1.0 Oxidic Corium-E; 6 Tests	0.3	Bridgewire @3 kV	0.86	0.33	1 fine fragment; 5 single pieces
1.0 Oxidic Corium-E; 8 Tests	0.5	Bridgewire @3 kV	0.8	0.305	1 fine fragment and 1.4-MPa pulse; 7 single pieces; caldera formed
1.0 Oxidic Corium-E; 1 Test	0.5	Minidetonator	Misfire 6.9	1.7	Fine fragmentation ~0.77 MPa pulse
1.0 Oxidic Corium-E; 6 Test	0.75	Bridgewire @ 3 kV	1.05	0.4	Single piece. Caldera formed
1.0 Oxidic Corium-E; 2 Test	1.0	Bridgewire @ 3 kV	--	--	Single piece. With caldera

TABLE 2-III (cont)

Material	P_{∞} (MPa)	Pressure Generator	P_2^a (MPa)	P_{melt}^b (MPa)	Results
0.78 Oxidic Corium-E; 6 Tests	0.5	Minidetonator	Misfire 10.3 @ 20 μ s	2.5	Single piece with tall cone formed or pieces blown apart
Fe_2O_3 ; 1 Test	0.2	Bridgewire @3 kV	0.89	0.34	Fine fragmentation; 3 pressure pulses
Fe_2P_3 ; 1 Test	0.3	Bridgewire @3 kV	0.69	0.26	Fine fragmentation; 2-stage explosion ~1.4 MPa
Fe_2O_3 ; 3 Tests	0.5	Bridgewire @3 kV	0.93	0.35	Difficulty melting single piece
Fe_2O_3 ; 1 Test	0.75	Minidetonator	--	--	Single piece; not much information

^aAveraged over all recorded pulses.

^bFound by assuming a 1/r dependence from the transducer P_2 to melt center.

To address these experimental results and previous explanations of them, the dynamics of vapor film destabilization by applied pressure pulses is being investigated. Initially the analysis centers upon the film boiling behavior of a hot molten sphere in the coolant. The major assumption is that the pressure pulse application and subsequent collapse is symmetric. This assumption makes the analysis amenable to simple phenomenological modeling. The film boiling is modeled by considering the molten drop, vapor film and surrounding coolant as lumped parameter volumes and writing an energy equation for each region coupled by temperatures and heat fluxes. Dynamic film boiling behavior can be predicted as a function of the applied pressure pulse and other initial conditions. A detailed description of the model will be presented in an upcoming topical report.

It should be emphasized that the results are not directly applicable to the first stage interaction of Nelson's experiments¹ because (1) the initial test geometry is more complex for stage 1 interaction and (2) the film-boiling collapse before Stage 1 may be asymmetric. However the results should indicate the effect of different subcoolings and ambient pressures, with more direct applicability to the second stage of the interaction as observed by Nelson where the geometry of the molten fuel is spherical and symmetric.

The growth of the vapor film before a pressure transient is applied is dependent upon the ambient pressure and to a lesser extent on the initial water temperature as Figure 2-13 and 2-14 illustrate. The density of water vapor increases linearly with pressure and thus, for higher ambient pressures, the same mass is contained in a smaller volume. Thus the film thickness decreases. As the water temperature increases, the temperature gradient between the liquid-vapor interface decreases. This causes less energy to flow into the liquid and more into generating water vapor. Therefore the mass of vapor increases and hence so does the film thickness. The initial conditions for these calculations were taken to be representative of what may be the characteristic size (~3.5 mm) and temperature (~2000 K) of the molten fuel before the second stage explosion in Nelson's experiments. The growth time (~3 ms) is also representative of the delay between stage 1 and stage 2 of the explosion.

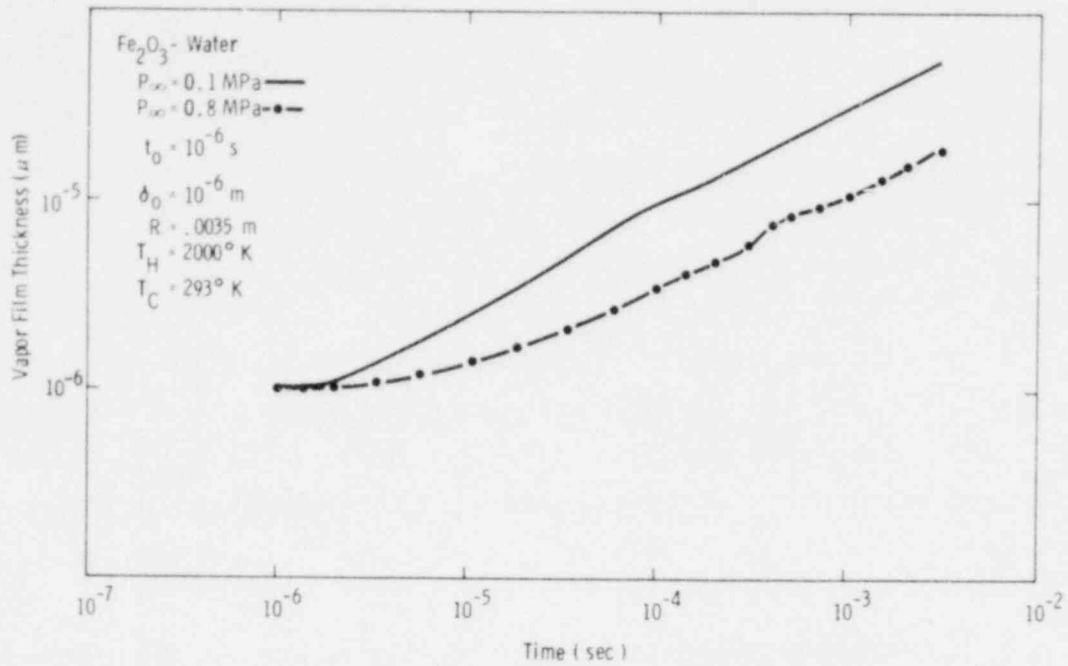


Figure 2-13. Vapor Film Growth Behavior (Water Temperature Dependence)

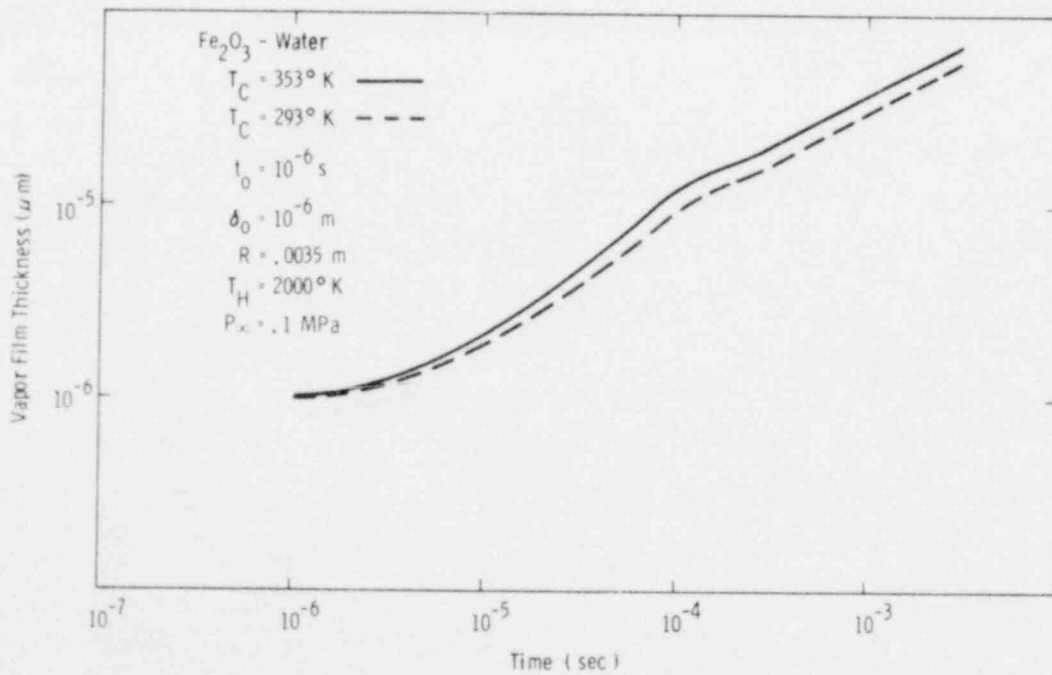


Figure 2-14. Vapor Film Growth Behavior (Ambient Pressure Dependence)

When modeling the dynamic collapse of the film due to a pressure pulse, there are two ways in which the heat transfer can be represented at the water vapor-liquid interface: (1) local thermodynamic equilibrium exists between the vapor and liquid and (2) nonequilibrium exists at the interface and condensation and vaporization rates are specified by using additional models. Drumheller¹⁴ has theoretically modeled the collapse process based upon the latter interface model with the additional constraint of neglecting the heat transfer from the hot molten fuel. Bankoff et al¹⁵ have modeled the film destabilization process for a set of past experiments performed by Inoue¹⁶ using both models but neglecting the work energy ($\int p dV$) of the collapsing bubble. No justification for use of either model or these additional assumptions was presented. However the dynamic behavior of film collapse is significantly dependent upon these models. An upcoming topical report details the present analysis and a representative result is presented here. It should be noted that vapor heat transfer and work energy are included in this analysis. Collapse behavior is predicted in Figure 2-15 using both interface conditions. The pressure pulse was assumed to be a square wave with a pulse width and energy similar to that in Nelson's experiments (~ 0.8 MPa @ $20 \mu s$). The major difference noted is that the film is predicted to reach a minimum value and rebound with the equilibrium model whereas it is predicted to rebound at much smaller film thicknesses with the nonequilibrium model (the calculation was stopped if the film was less than 10^{-6} m). The difference is caused by the computed pressure in the vapor film which resists the collapse process. The film pressure (P_f) using the equilibrium model rises much sooner because more coolant is vaporized faster as δ becomes very small. At some point P_f is much greater than the ambient and begins to accelerate the interface outward. This difference in collapse behavior will be addressed in the future by modeling simple film boiling experiments¹⁶ to determine which model is applicable over what range of initial conditions. This is of importance in the propagation phase of the interaction where the heat flux may be dependent upon the film thickness. However for the triggering phase of the interaction both models exhibit the same trends with regard to changes in water temperature or ambient pressure. Therefore results are presented using the equilibrium interface condition.

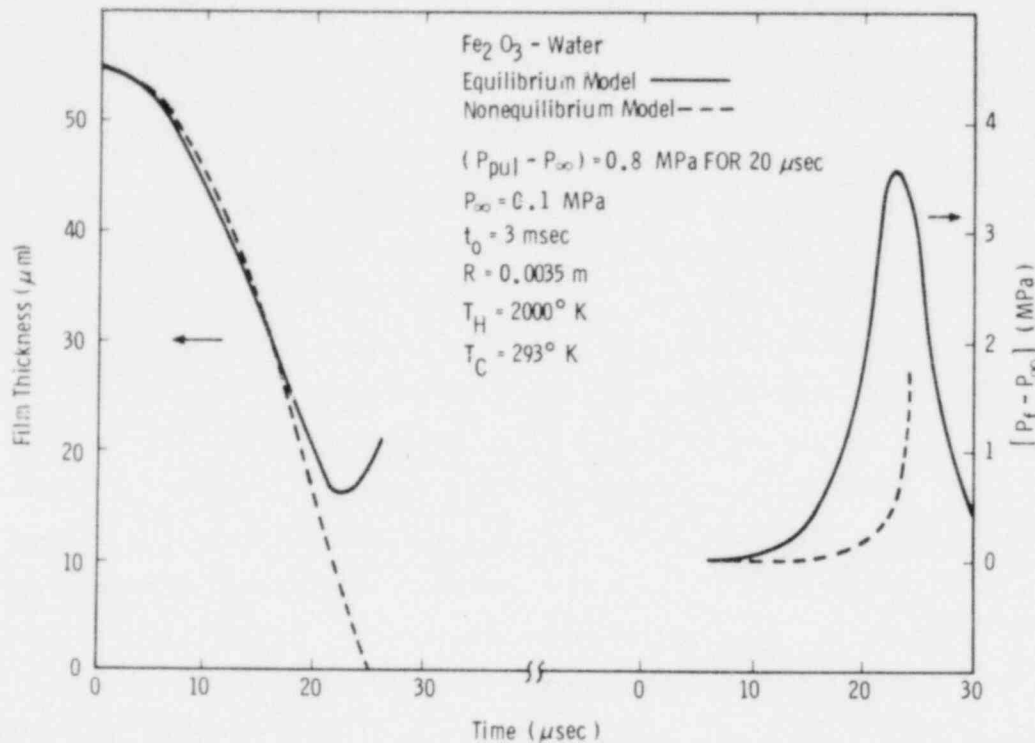


Figure 2-15. Comparison of the Equilibrium and the Nonequilibrium of Film Boiling Collapse

Application of a pressure pulse causes the vapor-liquid interface to be accelerated inward, causing vapor condensation. As the film thickness decreases significantly, the energy transferred from the hot fuel to the coolant becomes large, causing coolant vaporization and the film vapor pressure (P_f) to rise. P_f increases above the ambient pressure; acceleration is now directed outward from the vapor into the liquid, which is a hydrodynamically unstable condition. The liquid-vapor interface becomes distorted and interfacial Taylor instability waves are accelerated toward the melt surface and may collapse upon it even though the overall interface collapse process is slowed and goes through a minimum. The model does not account for this Taylor instability growth but rather shows the overall interface being stopped (minimum film thickness) and then pushed outward by the high pressure film. The instability growth can be modeled

by Taylor's linear theory where the instability amplitude over its initial amplitude (η/η_0) is given by

$$\eta/\eta_0 = \cosh (nt) \quad (8)$$

where

$$n = \left[\frac{2\pi}{\lambda} \frac{a(\rho_l - \rho_v)}{\rho_l + \rho_v} \right]^{1/2} \quad (9)$$

and where λ is taken to be the fastest growing Taylor wavelength

$$\lambda \doteq \lambda_m = \pi \sqrt{\frac{3\sigma}{(\rho_l - \rho_v)a}} = \sqrt{3 \lambda_C} \quad (10)$$

and

- a = the acceleration caused by the film pressure
- σ = liquid-vapor surface tension P_f
- ρ_l and ρ_v = liquid and vapor densities respectively.

The linear theory coupled with the collapse model can give an indication of the effects of various initial conditions.

When the ambient pressure or the water temperature increases, the predicted peak pressure during film collapse is reduced (Figures 2-16 and 2-17). High ambient pressures require that more energy be expended to vaporize the liquid thus less vapor is created and the peak pressure is reduced during collapse and occurs sooner than it would at lower pressures. The collapse behavior is more thermally controlled and is sluggish. To a lesser extent this sluggish behavior is exhibited with higher water temperatures. The reason here though is that the minimum film thickness is larger for a larger initial water temperature and less heat flows into the liquid. Thus the film pressure builds more slowly and to a lower magnitude. The net effect for high ambient pressure or water temperature is that the acceleration causing instability growth is reduced and the film

may not collapse as readily. This behavior is shown in Figure 2-18 for a change in the ambient pressure. The net growth of an instability wavelength $(\eta - \eta_0/\eta_0)$ is plotted as a function of the applied trigger pressure pulse $(P_{\text{pulse}} - P_{\infty})$ for two ambient pressures (P_{∞}) . The instability growth and thereby film collapse is significantly retarded when the trigger pulse is low $(P_{\text{pul}} - P_{\infty} \sim 0.3 \text{ MPa})$ and the ambient pressure is high $(P_{\infty} = 0.8 \text{ MPa})$. The growth difference between low and high ambient pressure is more than an order of magnitude for $(P_{\text{pul}} - P_{\infty}) \sim 0.3 \text{ MPa}$. However when the trigger pulse is increased in energy, $(P_{\text{pul}} - P_{\infty}) \sim 2.5 \text{ MPa}$ @ $20 \mu\text{s}$, the difference between the instability growth is only a factor of two for two different values of P_{∞} . A direct link cannot be made between film collapse and the instability growth because the initial amplitude of the wavelength, η_0 , is not known. The inference though is that, if a larger trigger pressure pulse is applied, the film will collapse regardless of the ambient pressure or water temperature. And if P_{∞} and T_C affect only the triggering phase of the interaction, an explosion would then be expected.

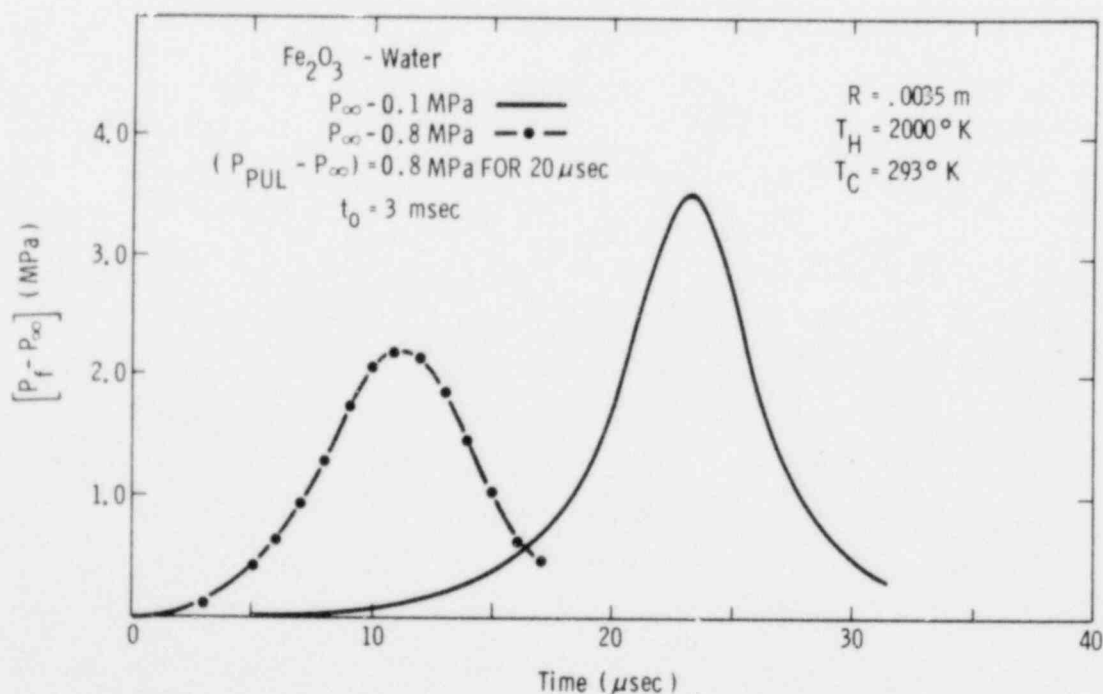


Figure 2-16. Vapor Film Pressure Behavior During Collapse

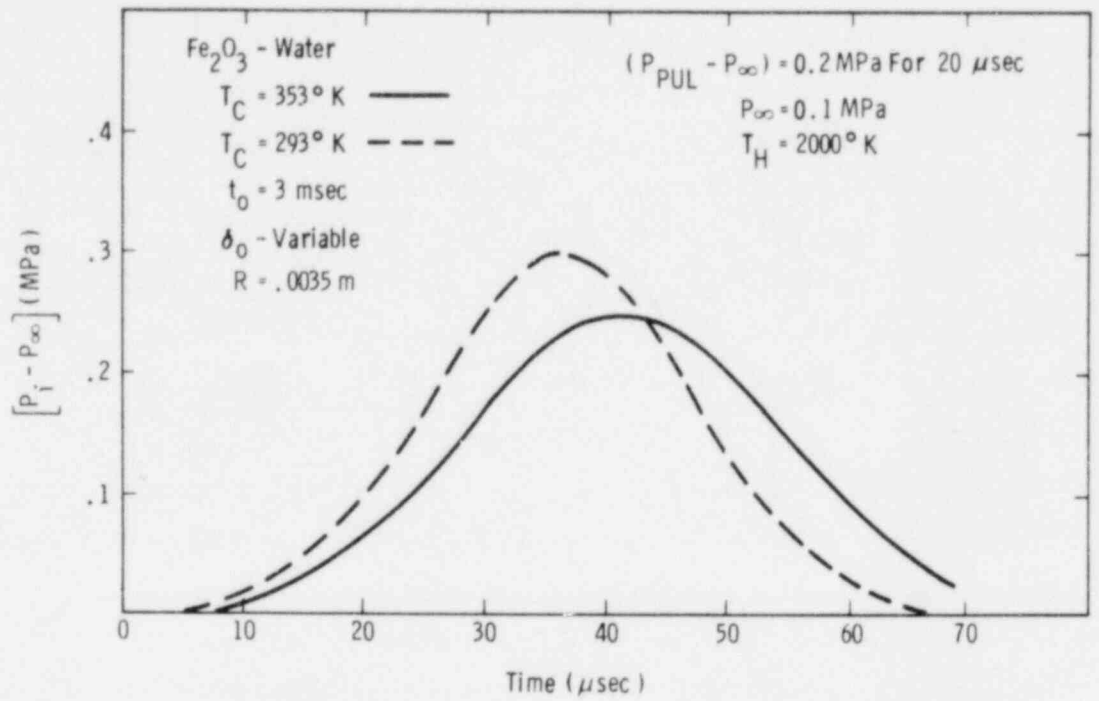


Figure 2-17. Vapor Film Pressure Behavior During Collapse

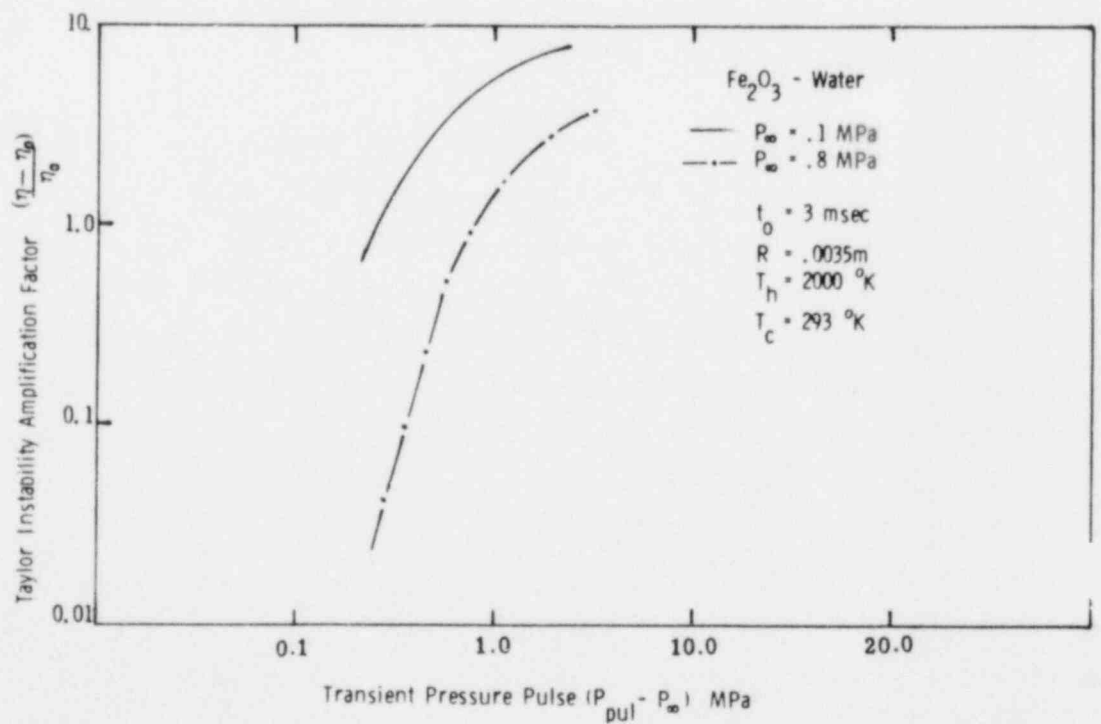


Figure 2-18. The Effect of Ambient Pressure on Taylor Instability Growth

This conclusion was validated for high water temperatures by Nelson. A vigorous explosion ($P \sim 3.5$ MPa) was obtained by using a detonator generated pressure pulse (~ 5 MPa) at high water temperatures ($\sim 85^\circ\text{C}$) where previous bridgewire pulses (~ 0.5 MPa) failed. For high ambient pressures the sluggish collapse behavior (thermally controlled) exhibited during the triggering phase also occurs during the propagation phase during vapor growth as Henry^{12 13} points out. Continued analysis and experiments are underway to resolve this question.

2.5.2 Propagation Experiments

After the interaction has been triggered, the molten fuel energy is rapidly transferred to the surrounding coolant. This is accomplished on short time scales (< 1 ms) by rapid fragmentation of the molten fuel to increase the heat transfer area and an efficient heat transfer regime (i.e., liquid-liquid contact or thin vapor film boiling), in various geometric configurations. The heated coolant then expands against the inertial constraint of the surrounding and transforms its acquired internal energy into disruptive mechanical energy.

The large-scale fully instrumented test series is designed to investigate the effects of melt and coolant compositions and temperatures, geometric constraints and possibly ambient pressure on the conversion ratio of the fuel internal energy into mechanical work. These integral tests will hopefully aid in determining the scale effects on the interaction work output either by (1) providing experiments with which to compare phenomenological models or (2) supplying experimental data for the purpose of constructing empirical correlations for mechanical work conversion ratio.

What is lacking from these large-scale tests is the detailed investigation of the fragmentation and heat transfer process which is occurring on a length scale consistent with coarse intermixing of the molten fuel ($\sim 0.1 - 1$ cm). The small-scale heating techniques developed by Nelson may be able to accurately control the initial conditions of molten fuel so that experiments examining primarily fragmentation and heat transfer can be conducted. Recent experiments using a laser heating technique have

successfully produced coherent explosions (~3.1 MPa) for iron-oxide melts of the appropriate length scales (~3.0 mm). The technical advantages of these experiments are (1) the geometry is well characterized during melting and fuel-coolant contact, i.e., spherical and (2) the initial fuel temperature and composition and the mass participating in the interaction are accurately known. Thus the dependent variables observed are reduced to the work output and the fragmentation behavior of the interaction which are believed to be representative of the microscopic behavior during the propagation phase.

Because both of these programs have just started, analysis in this area is now centered on research into the basic mechanism of fragmentation and heat transfer. The fragmentation experiments of Patel and Theofanous¹⁷ are initially being used as a focal point to address modeling of fuel fragmentation. The experiment consists of a liquid water shock tube (width ~5 cm) into which a mercury droplet (~1 - 10 mm) is placed and subjected to a planar shock wave ($5 < \Delta P < 150$ MPa @ 1-2 ms pulse width). The fragmentation behavior is then observed and compared to proposed fragmentation models. These mercury-water experiments represent a logical starting point for investigation of fuel fragmentation in three stages:

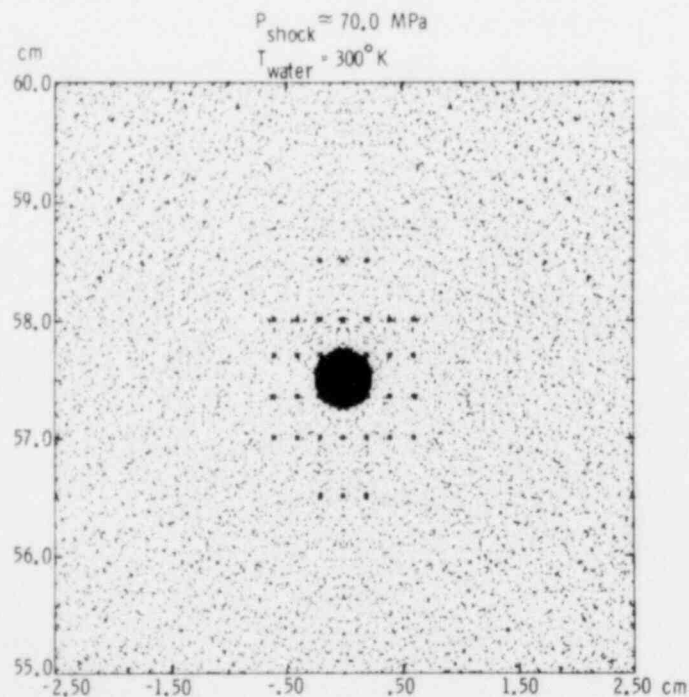
1. Liquid-liquid isothermal fragmentation
2. Liquid-gas-liquid isothermal fragmentation, gas = air
3. Liquid-vapor-liquid nonisothermal fragmentation

This final phenomenon to be investigated is part of the small scale experiment being developed by Nelson.

The isothermal mercury-water experiments are being numerically modeled using the hydrodynamic code CSQ. CSQ is a program which predicts the transient flow of materials (solids, liquids and gases) under a variety of initial conditions by using a LaGrangian formulation of the conservation equations in an Eulerian calculational mesh. The major assumptions for the models used in the code are

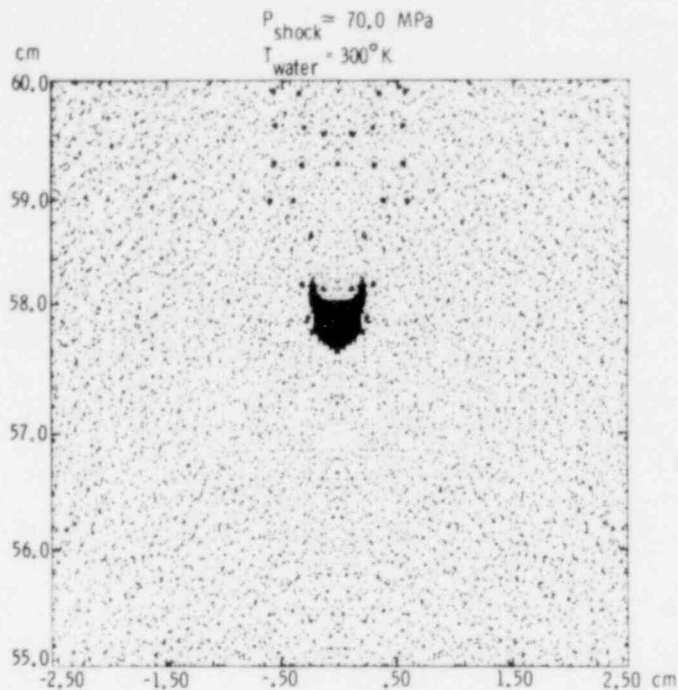
1. One set of continuity equations is written for each mesh cell and it is therefore assumed that different materials in the cell are in equilibrium in velocity and temperature.
2. Surface tension is not included in the models and because of the assumed local equilibrium, material mixing laws are used to preferentially move different materials from one cell to another.

These two assumptions cause the fragmentation behavior of the mercury droplet to be dependent upon the mesh cell size. The mesh cell size can be reduced to suppress this unphysical effect; however, there is a lower limit ($\Delta x \sim 10 \mu\text{m}$) below which code calculations become prohibitively expensive. Preliminary results indicate that the mercury drop response to a planar shockwave is qualitatively similar to Patel and Theofanous' experimental results¹⁷ (Figure 2-19). Work is to continue in this area with the final objective being analysis of the interaction for coarse intermixing length scales ($\sim 1-10 \text{ mm}$).



a. Time = 0.0 s

Figure 2-19. Numerical Simulation of Hydrodynamic Mercury Water Experiment. • Dots are tracer particles; dot density represents material density; mercury drop is at the center, surrounded by water coolant ☼.



b. Time = 0.0004 s

Figure 2-19 (concluded)

In conjunction with these past efforts fragmentation is also being examined by using simple phenomenological models. Originally Patel and Theofanous¹⁷ concluded that Taylor instability growth was the dominant mechanism for the observed mercury fragmentation. They based this conclusion on a simple analysis using the linear growth theory of a Taylor instability to match experimental results. The characteristic breakup time was defined to be

$$\tau_b \equiv \eta_0 / d\eta/dt \quad (11)$$

where η_0 is the initial perturbation amplitude of the mercury-water interface and the amplitude growth rate, $d\eta/dt$, is found by taking the time derivative of Eq (8). This results in a dimensionless breakup time, τ^* , of the form

$$\tau^* = \tau_b \frac{U_{\text{rel}}}{r_{\text{drop}}} = \frac{1}{n e^{nt}} \frac{U_{\text{rel}}}{r_{\text{drop}}} \propto \frac{1}{n} \left(\frac{U_{\text{rel}}}{r_{\text{drop}}} \right) \quad (12)$$

where

U_{rel} is the relative velocity between the drop and the liquid

r_{drop} is the drop radius.

If Eq (9) is substituted in for the growth time constant, n , the resultant expression becomes, after some manipulation,

$$\tau^* \propto 1.5 \left(\frac{\rho_m}{\rho_w} \right)^{1/2} Bo^{-1/4} \quad (13)$$

where ρ is density for the mercury, m , and water, w , Bo is the Bond number defined as

$$Bo = \frac{\rho_m a r_{drop}^2}{\sigma_{mw}} \quad (14)$$

where the acceleration is given by

$$a = \frac{3C_D}{8} \left(\frac{\rho_w}{\rho_m} \right) \frac{U_{rel}^2}{r_{drop}} \quad (15)$$

for $C_D = 2$

$$\text{and } U_{rel} = \Delta P_{shock} / \rho_w C_w - \Delta P / \rho_m C_m \quad (16)$$

This expression for the characteristic breakup time gives reasonable agreement with the experimental results within a proportionality constant.

The analysis though does not seem to be physically correct. If the Taylor instability mechanism governs the mercury droplet fragmentation, the instability growth rate over long times is the appropriate

velocity to use. The linear growth rate used is only valid over a short time when the instability starts to grow and the amplitude, η , is smaller than the wavelength, λ . This period of growth would not encompass a large fraction of the fragmentation process. Instead, the nonlinear growth rate model based on experiments by Corradini¹⁸ should be used. The rate of instability growth, V_r , is given by

$$V_r = C_1 \sqrt{a \lambda_C} + C_2 \sqrt{a \lambda_0} \quad (17)$$

where λ_C is the critical Taylor instability wavelength given by Eq (10).

λ_0 is the observed wavelength given by

$$\lambda_0 \propto at^2 \text{ for } \lambda_0 \ll r_{\text{drop}} \quad (18)$$

$$\lambda_0 \propto r_{\text{drop}} \text{ for } \lambda_0 \leq r_{\text{drop}}. \quad (19)$$

The dimensionless breakup time can be again derived based on a new definition for the breakup time, τ_b

$$\tau_b \equiv \frac{\lambda_C}{V_r} \quad (20)$$

This definition is based on the physical picture that the time for breakup is influenced by time for the instability to travel across the drop, r_{drop}/V_r , and the relative size of critical Taylor wavelength, λ_C , to r_{drop} , $\lambda_C/r_{\text{drop}}$. Table 2-IV gives the results of this analysis for dimensionless breakup time, τ^* , where it is assumed that any one component of V_r may dominate. It should be noted that one of the results is again similar to Eq (13). What is more important is that all of these models separately exhibit the same general trend in the experimental data for the breakup time: (1) the density ratio of ρ_{drop} to ρ_{fluid} appears to the 1/2 power and (2) the breakup time decreases as the ΔP_{shock} increases (Bo increases) to a fractional power. It appears then that, if Taylor

instability is the dominant mechanism, the fragmentation process is much more complex than first imagined and the model should be revised.

TABLE 2-IV

Results of Analysis for Dimensionless Breakup Time

$\frac{\tau_b}{\lambda_C/v_r}$	$\frac{v_r^{++}}{\lambda_C/v_r}$	$\frac{\tau^{*+}}{\lambda_C/v_r}$
λ_C/v_r	$C_1 \sqrt{a\lambda_C} + C_2 \sqrt{a\lambda_o}$	$\left(\frac{\lambda_C}{r_{drop}}\right) \left(\frac{U_{rel}}{v_r}\right)$
λ_C/v_r	$\sqrt{a\lambda_C}$	$Bo^{-1/4} \left(\frac{\rho_m}{\rho_w}\right)^{1/2}$
λ_C/v_r	$\sqrt{a\lambda_o}$	$Bo^{-1/2} \left(\frac{\rho_m}{\rho_w}\right)^{1/2}$
	$\lambda_o \approx r_{drop}$	
λ_C/v_r	$\sqrt{a\lambda_o}$	$Bo^{-1/2} \left(\frac{\rho_m}{\rho_w}\right)^{1/2} \left(\frac{r_o}{at^2}\right)^{1/2}$
	$\lambda_o \approx at^2$	

$$^+ \tau^* \equiv \tau_b U_{rel} / r_{drop}$$

$++v_r$ is changed depending on which effect dominates.

2.6 Assessment of Containment Failure Capability by Steam Explosions (M. Corradini, R. Woodfin)

Steam explosions are of interest in hypothetical core melt accidents because they may provide a radiological transport path to the environment by containment failure due to a dynamic overpressure or missile generation. Therefore the final portion of this research work is to couple the experimentally observed interaction results with analyses to determine containment failure capability. The approach is based on four tasks:

1. Assume a conservative upper bound on the coherent release of energy from triggering and propagation of the interaction and then assess various mechanisms by which the work energy may be dissipated during the coolant slug acceleration prior to reactor vessel head impact
2. Determine the ways the reactor vessel may be failed and/or a missile be generated due to the impact of the coolant slug
3. Perform order of magnitude analyses to assess mechanisms that may dissipate the missile energy in its flight toward the containment
4. Use simple structural models or analyses to predict if containment failure could occur due to (i) missile impact or (ii) dynamic overpressure

The status of each task will be reviewed briefly.

2.6.1 Energy Dissipation Mechanisms Prior to Reactor Vessel Impact (M. Corradini)

Heat transfer to the cold water slug above the fuel-coolant interaction zone and to solid structures in the vessel (Figure 2-20) may be a major energy dissipation mechanism for the hot expanding coolant vapor. However, it should be emphasized that the amount of heat transfer is dependent upon the geometry within the vessel for coolant vapor expansion which, in turn, is accident-scenario dependent. In fact, if it is postulated that no steam explosion occurs within the reactor vessel but rather below in the reactor cavity area, these same heat transfer processes are operative but now with different initial conditions and geometry.

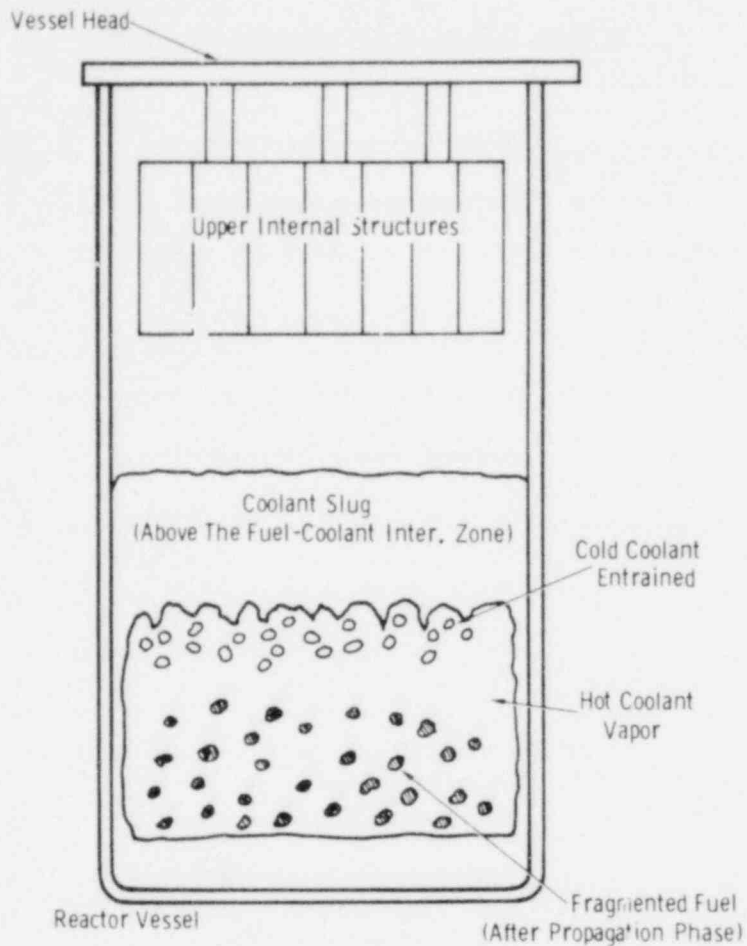


Figure 2-20. Conceptual View of the Expansion Phase Before Reactor Vessel Head Impact

Because of this dependence on the likely accident scenario which at this time is quite uncertain, the research is primarily directed toward identifying the key heat transfer phenomena, and with proposed models performing parametric calculations to determine the possible range of effects on this expansion work of the interaction.

Heat transfer to solid structure in the core is very scenario dependent because the structural geometry remaining after the accident dictates the surface area available for heat transfer. Therefore this question cannot be adequately addressed at this time other than to assume either of two extremes cases; all the upper vessel structure has melted out or all is still in place. The heat transfer coefficient for this

process is complicated by the fact that as the high pressure coolant vapor from the interaction expands it pushes the liquid coolant slug upward exposing solid structure with a liquid water film remaining (Figure 2-21). Depending on the liquid film thickness, Δ , the heat transfer process may be dominated by transient condensation on the liquid film or a combination of condensation and conduction in the solid. Ozgu and Chen¹⁹ indicate the ratio of Δ to the hydraulic diameter of a channel, D_H , is on the average 0.1 for driving pressures of a few bars. For this interaction, the driving pressure is an order of magnitude; higher thus a rough estimate of the film thickness would be

$$0.01 < \Delta/D_H < 0.1 \quad . \quad (21)$$

The hydraulic diameter is again dependent on the geometry but, if we choose the smallest D_H possible and $\Delta > \sqrt{\alpha_f \tau_{exp}}$, then liquid-film-controlled condensation would appear to be the dominant heat transfer process. The smallest D_H is in the fission gas plenum, with $D_H \sim 1.1$ cm; therefore

$$0.011 < \Delta < 0.11 \text{ cm.}$$

The thermal penetration thickness is found by evaluating the characteristic expansion time through the structure this time can be estimated to be

$$\tau_{exp} \approx \left(\frac{2 \Delta L_s}{a} \right)^{1/2} \quad . \quad (22)$$

and

$$a \approx \frac{\Delta P}{\rho_W L_W} \quad (23)$$

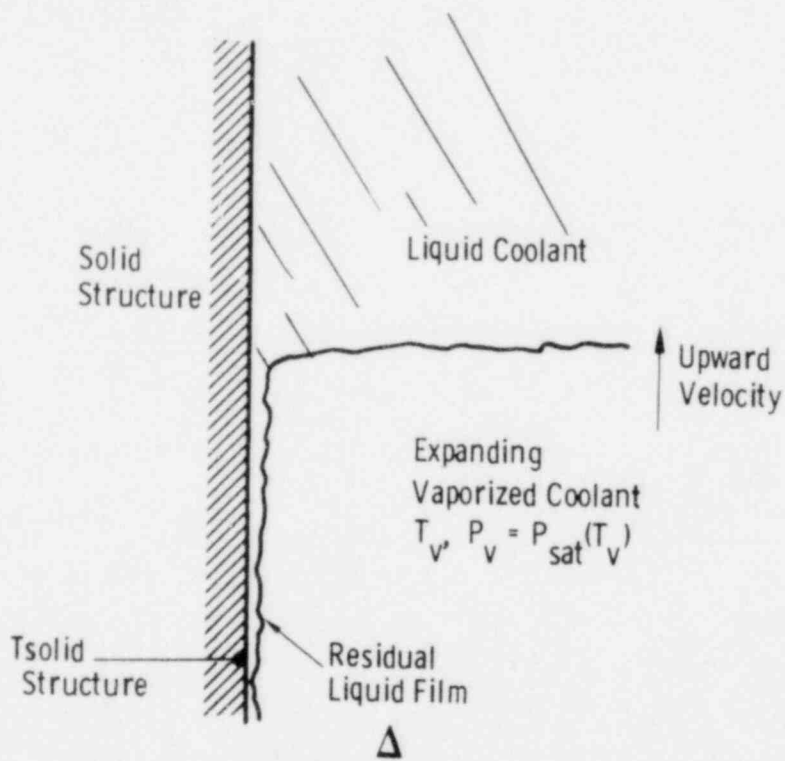
where

ΔL_s - length of the structure ≤ 3 m

ΔP - pressure pulse due to interaction ≈ 10 MPa

L_w - depth of coolant slug ≈ 1 m

This gives $\tau_{exp} \approx 20$ ms and $\sqrt{\alpha_l \tau_{exp}} \approx 0.005$ cm. Thus $\Delta > \sqrt{\alpha_l \tau_{exp}}$ and film controlled condensation is the expected mode of heat transfer.



- Heat Transfer with Liquid Film Only

$$\Delta > \sqrt{\alpha_l \tau_{exp}}$$

α_l - thermal diffusivity of liquid coolant

τ_{exp} - characteristic expansion time through the structure

- Heat Transfer With Solid Structure With Liquid Film as a Heat Transfer Resistance

$$\Delta < \sqrt{\alpha_l \tau_{exp}}$$

Figure 2-21. Schematic of Solid-Vapor Heat Transfer Model

Heat transfer to the cold liquid coolant should be considered. This process takes place between the hot vapor and the liquid above the fuel-coolant interaction zone during its acceleration by coolant vapor expansion. The surface area for this heat transfer would be created by fluid instabilities which cause the liquid coolant to become entrained in the hot vapor. When condensation heat transfer similar to that expected with the liquid film on the solid structure would occur. The amount of liquid coolant entrained into the expanding hot vapor may be caused by a number of mechanisms. Some that have been proposed are

- Taylor instability entrainment would be caused by the less dense vapor accelerating the more dense liquid. Corradini¹⁸ has proposed a model for this entrainment mechanism.
- Helmholtz instability entrainment would be caused by vapor flow over a liquid film. Cagliostro et al²⁰ have suggested this mechanism but no models have been proposed.
- Theofanous²¹ has recently suggested that neither hydrodynamic entrainment mechanism previously described may dominate in a condensing vapor expansion. Rather it has been suggested a condensation shock occurs at the vapor-liquid interface entraining the liquid coolant. No model has been proposed.

All these mechanisms may be operative during the expansion and none may dominate. Work is continuing on these entrainment models, however at this point analysis based on Taylor instability entrainment alone is presented and applied to the accident situation. This mechanism is felt to be operative throughout this transient expansion because vapor is accelerating the liquid coolant. The model to be presented has been compared to small scale integral experiments at SRI performed by Cagliostro.²⁰ A short comparison is given here with a detailed explanation of the model and experiments to be included in an upcoming topical report.

The Taylor instability entrainment model is based on simple hydrodynamic experiments.¹⁸ These planar two-dimensional experiments were used to determine the nonlinear growth rate of the Taylor instability at a water-air surface. Based upon the results a volumetric entrainment model, \dot{V}_e , is proposed to be

$$\dot{V}_e = \frac{dV_e}{dt} = 4.6 A_p \sqrt{a \lambda_C} \quad (24)$$

where λ_C is the critical Taylor wavelength, Eq (10), and A_p is the projected area.

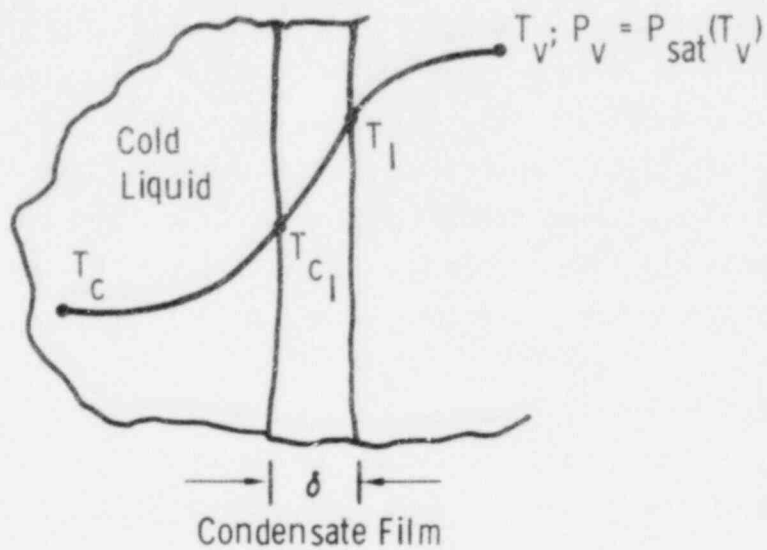
The surface area, A_d , of the entrained liquid is

$$A_d = \frac{6 V_e}{D_d} \quad (25)$$

where D_d is the characteristic entrained drop diameter thought to be between $\lambda_C \leq D_d \leq \lambda_m = \sqrt{3 \lambda_C}$. This characteristic diameter is felt to be near λ_C because this is the probable size of the entrained droplets when they are being formed. Further droplet breakup due to Weber forces may occur if $We > We_{crit}$ and if the breakup time is smaller than the time scale of the transient.

The condensation heat transfer coefficient for these processes can be approximated to be a combination of three heat transfer resistances (Figure 2-22); (i) interfacial resistance to condensation, h_I , (ii) condensate film heat transfer resistance, h_f , (iii) heat transfer resistance in coolant droplet or film or solid structure due to transient heating, h_W . Note that both the drop and the film are treated as semi-infinite because $\Delta > \sqrt{\alpha_W t}$, or $D_d > \sqrt{\alpha_W t}$. The interfacial resistance is negligible for these processes in comparison to the other resistances and thus the heat transfer coefficient is

$$h_{TOT} = \frac{1}{\frac{\delta}{k_W} + \frac{\sqrt{\pi \alpha_W t}}{Z k_W}} \quad (26)$$



$$\dot{q}'' = h_{TOT} (T_V - T_C)$$

$$\frac{1}{h_{TOT}} = \frac{1}{h_W} + \frac{1}{h_f} + \frac{1}{h_I}$$

$$h_W = \frac{k_W}{\sqrt{\pi \alpha_W t}}$$

$$h_f = \frac{k_W}{\delta}$$

$$h_I = \frac{h_{fg}}{(T_V - T_I)} \left[\frac{1}{\sqrt{2\pi R_W}} \left(\frac{P_{sat}(T_V)}{\sqrt{T_V}} - \frac{P_{sat}(T_I)}{\sqrt{T_I}} \right) \right]$$

Figure 2-22. Schematic of Liquid-Vapor Heat Transfer Model

For the case of liquid heat transfer the heat transfer rate becomes, combining Eqs. (24-26),

$$\dot{q} = \frac{6 V_e}{D_d} h_{TOT} (T_V - T_C) \quad (27)$$

The vapor expansion is modeled by a one-dimensional momentum equation and the expanding vapor volume is modeled by a lumped parameter energy equation including this heat transfer model. This model was applied to vapor source integral experiments performed at SRI.²⁰ The purpose of these tests was to answer LMFBR safety questions when condensable fuel vapor is discharged into a cold sodium pool. The test used hot two-phase water as a vapor source and a cold water pool to simulate the sodium.

The experimental apparatus employed by SRI International for these tests was a 1/30 scale model of the Clinch River Breeder Reactor upper plenum, without the above-core structure, and with subcooled water in the upper plenum and fission gas regions (Figure 2-23). The core region contained a high pressure (8.2 MPa), two-phase water source separated from the fission gas region by quickly opening sliding doors (explosively triggered). An extensive experimental description is given in Ref 20. It should be emphasized that although the geometry was scaled, the experiment was not intended to be thermodynamically similar to a vapor expansion at full-scale LMFBR reactor condition.

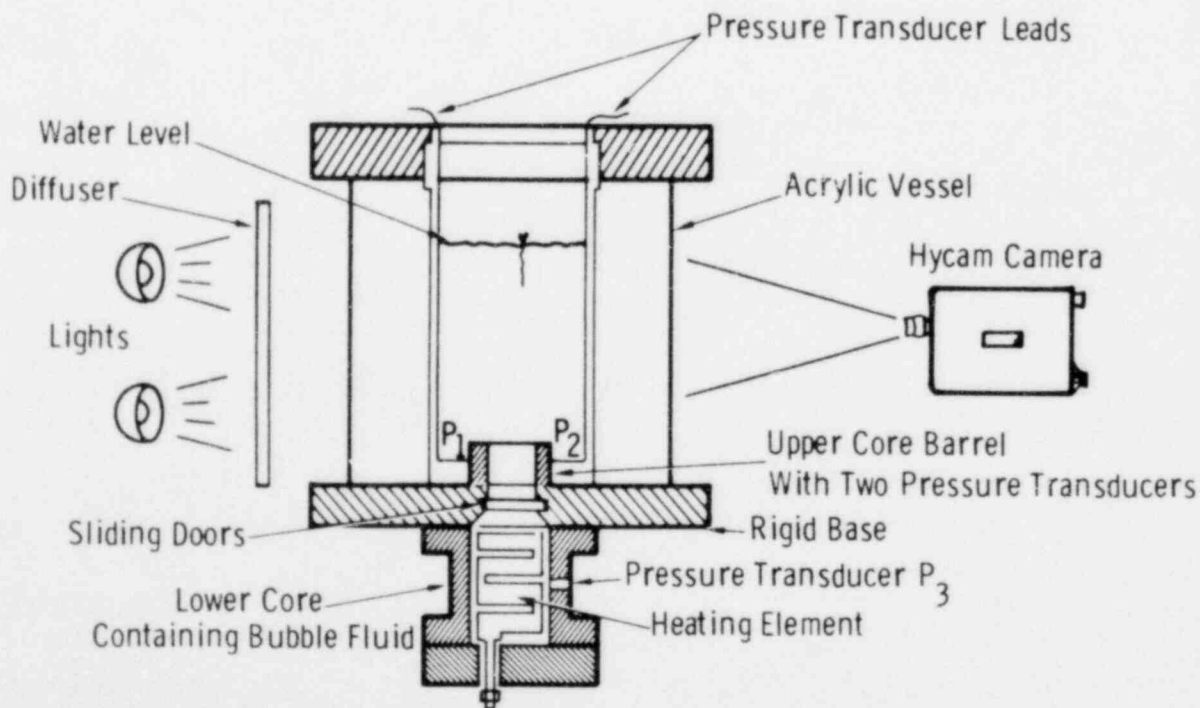


Figure 2-23. Schematic of Test C-003 Apparatus

However it is expected that the water vapor-liquid fluid pair is somewhat prototypic of the LWR vapor explosion application.

Figure 2-24 shows the measured vapor volume (V_g) and the entrained water volume (V_e) as a function of time for two SRI tests, one with the reactor vessel head removed and one with it in place. Calculations based upon the Taylor instability mechanism show good agreement with the data. The vapor volume expansion is bounded by using the proposed heat transfer model with the entrained coolant droplet diameter, D_d , being either λ_m , or λ_c . Most important, the reduction in the expansion work from adiabatic expansion conditions for the experiment is an order of magnitude and appears to be due primarily to this heat transfer process between the vapor and entrained liquid.

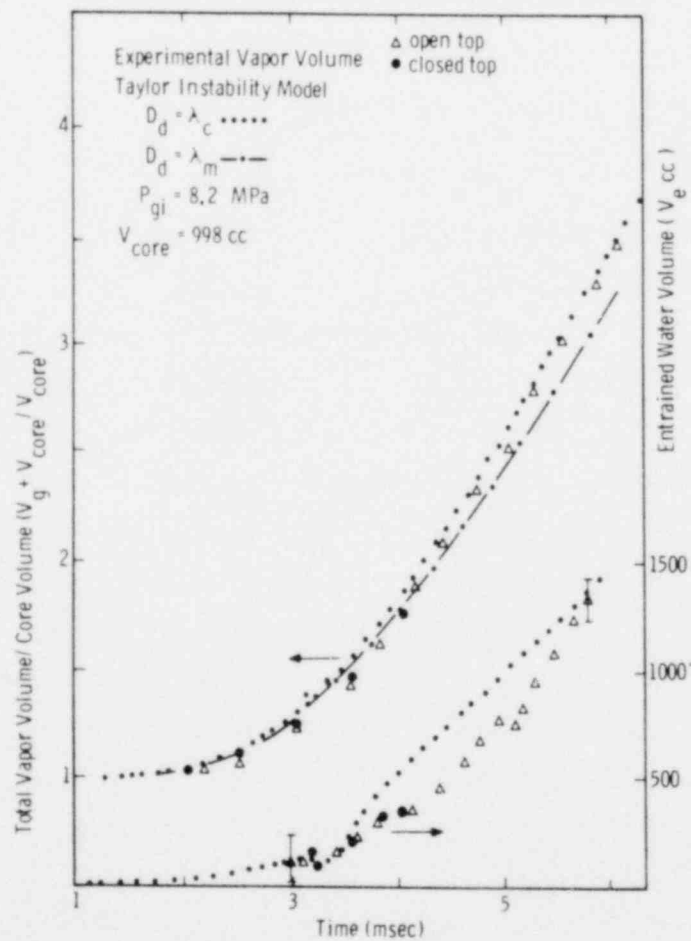


Figure 2-24. Comparison of Model With SRI Experimental Data

Other entrainment mechanisms may be operative during the expansion; however, it is felt that the Taylor instability mechanism dominates in the production of heat transfer surface area.

This simple model can be applied to the full scale LWR interaction given some appropriate initial conditions after the propagation phase has been essentially completed. Based upon the scoping experiments of Buxton and typical PWR vessel dimensions, the initial conditions are assumed to be

Mass of coolant in interaction - 1000 kg

Pressure in the interaction zone - 10 MPa @ 580 K

Quality of two-phase water - 0.05

Mass of coolant slug - 14000 kg

Reactor vessel area - 14 m²

Temperature of coolant slug - 373 K

Structure in core - none present

These values are calculated based on the picture that the lower plenum is full of water when part of the molten core and structure falls into it and an interaction occurs. The real unknown quantity is the mass of the coolant that participates in the heat transfer process. The mass value used is purely an assumption based on reasonable volume estimates to illustrate parametrically the possible effect of vapor-liquid heat transfer on the expansion work. Figure 2-25 illustrates the results of the calculation. The effect of heat transfer on expansion work is dramatic even when the coolant slug is assumed to be saturated at ambient pressure. This calculation only gives an indication of the possible dissipation effect of heat transfer. More realistic initial conditions must be determined before quantitative estimates of expansion work reduction can be given. Future work in this area will focus on evaluating other entrainment models for liquid heat transfer and the effects of various initial conditions on the expansion phase.

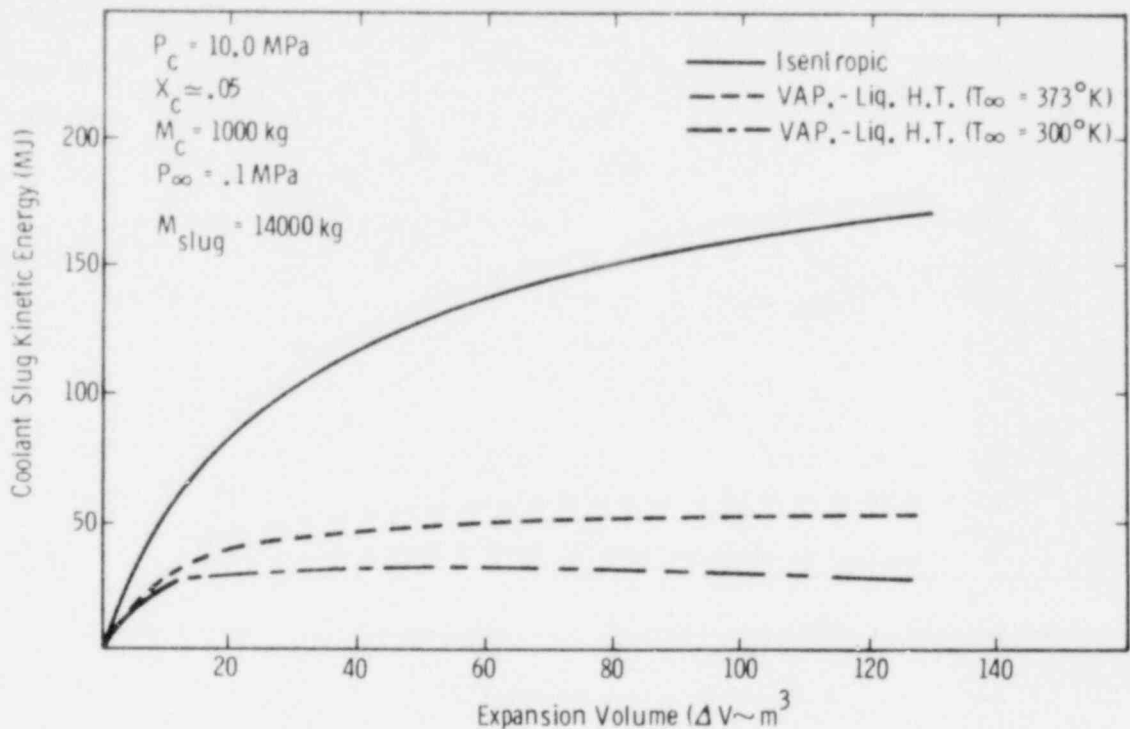


Figure 2-25. Energetic Fuel Coolant Interaction Expansion Phase

2.6.2. Reactor Vessel Failure Analysis (R. Woodfin)

A preliminary plan has been developed for analysis as follows: Conceptual development of the model of the reactor vessel will begin with the simplest representation possible and be refined a step at a time toward the objective of a realistic model which includes joints, obstructions, internal items, supports, etc. The fluid loading will begin similarly in a simple way, considering the fluid above the explosion as a rigid piston, then as a flexible one, then as a fluid one, and then adding the idea of fluid-structure interaction.

2.6.3 Missile Energy Dissipation (R. Woodfin)

Work has not begun on this item. It will follow the first modeling described in the previous section and be refined in a similar manner.

2.6.4 Containment Failure Analysis (R. Woodfin)

Since the containment failure is primarily a concrete penetration problem, the work presently in progress on another program (EPRI's

Concrete Impact Tests) should transfer but work specifically directed toward this item has not yet begun, other than research into the available literature. This will follow the two previous sections at each stage of the refinement of the modeling.

2.7 References

¹L. Nelson, L. Buxton, and H. N Planner, Steam Explosion-Triggering Phenomena P + II, Corium-A, Corium-E Simulants and Oxides of Iron and Cobalt Studied with a Floodable Arc Melting Apparatus, SAND 79-0260 (Albuquerque: Sandia Laboratories, nd). To be published.

²M. Epstein, et al, "Reconsideration of Gas Release in Molten Metal Fragmentation," Trans Amer Nucl Soc 27:669 (1977).

³M. Epstein, "Thermal Fragmentation--A Gas Release Phenomenon," Nucl Sci Eng 55:462-67 (1974)

⁴L. D. Buxton and L. S. Nelson "Impulse-Initiated Gas Release--A Possible Trigger for Vapor Explosions," Trans Amer Nucl Soc, 26:398-9 (1977)

⁵L. S. Nelson et al, "Effects of Oxygen and Argon Atmospheres on Pendant Drops of Aluminum Oxide Melted with Carbon Dioxide Laser Radiation," High Temp Sci, 5:138-154, (1973)

⁶S. Fordham, "On the Calculation of Surface Tension from Measurements of Pendant Drops," Proc Roy Soc (London) A194:1-16, (1948).

⁷C. E. Stauffer, "The Measurement of Surface Tension by the Pendant Drop Technique," J Phys Chem 69:1933, (1965).

⁸W. Nelson, "The Cause of Kraft Explosions," Combustion Engineering Report, 1972.

⁹L. A. Bromely, Handbook of Heat Transfer, ed W. M. Rohsenow (New York: McGraw-Hill Co, 1973), pp 13-73.

¹⁰F. Kreith, Principles of Heat Transfer (New York: Harper & Row, 1973).

¹¹H. S. Carslaw and J. C. Jaeger, Conduction of Heat in Solids (New York: Oxford Press, 1959).

¹²R. E. Henry, "Vapor Explosions of Freon-22 With an External Trigger," Presented at the LWR Safety Information Meeting held Nov 7, 1978, at Sandia Laboratories.

¹³R. E. Henry, Paper presented at the Fuel Meltdown Program Review and Information Exchange Meeting held Dec 5, 1978 at Sandia Laboratories.

¹⁴D. Drumheller, "A Cavitation Model for Fuel-Coolant Interactions" (Paper submitted to Nucl Sci Eng in Feb 1979).

¹⁵G. Bankoff et al, "Destabilization of Film Boiling Due to the Arrival of a Pressure Shock Part II: Analytical," Report COO-2512-15 (NW Univ, Dec 1978).

¹⁶A. Inoue, "Destabilization of Film Boiling Due to the Arrival of a Pressure Shock Part I: Experimental," Report COO-2512-13, (NW Univ., Apr 1978).

¹⁷P. D. Patel and T. G. Theofanous, "Fragmentation Requirements for Detonating Vapor Explosions," PNE-78-122 (Purdue: Nuclear Regulatory Commission, Jan 1978). Quarterly Report.

¹⁸M. Corradini, "Heat Transfer and Fluid Aspects of Fuel-Coolant Interactions," COO-2781-15TR (Boston: Massachusetts Institute of Technology, Sept 1978).

¹⁹R. Ozgu and J. C. Chen, "Local Film Thickness During Transient Voiding of a Liquid Filled Channel," 75-WA/HT-27 (Paper presented at the ASME Winter Annual Meeting in Houston, 1975).

²⁰D. J. Cagliostro et al, "Development and Characterization of a Liquid-Vapor Bubble Source for Modeling HCDA Bubbles," PYU-2939 (Albuquerque: Sandia Laboratories, March 1977). Technical Report 2.

²¹T. G. Theofanous, "Termination of Core Disruptive Accidents in LMFBRs," Presented at the Specialist Meeting on Predictive Analysis of Material Dynamics for LMFBR Safety Experiments held at Los Alamos on March 15, 1979.

3. Statistical Analysis

(G. P. Steck, R. K. Byers, M. Berman, L. D. Buxton)

3.1 Summary

The goal of this study is the application of statistical methods to the prediction of the probable distribution of peak clad temperature (PCT) in a pressurized water reactor during a loss-of-coolant accident (LOCA). Computer code predictions of PCT are analyzed to form response models, which may then be used in judging sensitivities to various physical parameters.

During the quarter, we completed the blowdown portion of the study, using RELAP4/MOD6, and began preparing the final report on that phase of the study. A coding error was discovered which had prevented the varying of one of the input parameters, and an assessment of its effect was made. Difficulties in initialization procedures were experienced, and corrected with the aid of Idaho National Engineering Laboratory. We discovered evidence that RELAP would, in our implementation, occasionally produce inconsistent results from identical input sets; an extensive study of this question showed that the results of the statistical analysis were probably not adversely affected.

The TRAC program, to be used for full LOCA analyses through reflood, was modified and the resulting code tested on a steady-state problem, but efforts to begin calculations for statistical analyses were hampered by the press of other work.

3.2 Statistical Analysis of Blowdown Results

Analysis of RELAP-predicted PCT values was completed for a set of 134 calculations. The nodalization (Figure 3-1) used a description of the Zion I plant. Variations in the values of 21 selected input parameters were made by several sampling techniques: Latin hypercube, fractional

factorial, and one-at-a-time. (Table 3-I lists the parameters varied; a more complete description may be found in Reference 1.) A few input sets were specified separately with the goal of achieving high values of PCT. Excluding one calculation, in which energy produced by the zirconium oxidation caused a temperature excursion and failure of the calculation, PCTs calculated ranged from about 770° to about 2270°F.

TABLE 3-I

Input Variables and Values

Parameter	Range	Nominal Value
1. DLEHRY = subcooled discharge coefficient	0.7 → 1.2	0.9
2. DLHEM = saturated discharge coefficient	-0.25 → 1.0	0.0
3. SLIP = slip correlation dial	-1.0 → 1.0	0.0
4. DLTF = 2-phase form loss dial	0.4 → 1.6	1.0
DLTFM = 2-phase Fanning friction loss dial		
These dials are assumed to be equal, and a single variable.		
5. DCHF = critical heat flux dial	0.3 → 2.0	1.0
6. DHTC6 = Condie-Bengston dial	0.5 → 2.0	1.0
7. DHTC7 = free convection and radiation dial	0.6 → 1.5	1.0
8. DHTC8 = Dittus-Boelter dial	0.5 → 2.0	1.0
9. DHTC9 = Hsu and Bromley-Pomeranz dial	0.5 → 2.0	1.0
10. DLBLK = flow blockage dial multiplier	0.4 → 1.6	1.0
11. DLMWR = multiplier of Metal-Water reaction rates*	0.85 → 1.15	1.0
12. DLPWR = power level multiplier	0.94 → 1.06	1.0
13. DLCPR = increment to be added to containment pressure	-5.0 → 10 psia	0.0
14. DLPUMP = dial for 2-phase pump head multiplier	-1.0 → 1.0	0.0
15. ECCTMP = temperature of accumulator and safety injection system water	40° → 140°F	90°F
16. DLACC = accumulator pressure	594.2 → 693.2 psia	643.2 psia
17. TLF = time in life	0.0 → 440 months	226 months
18. PFUNC = peaking factor uncertainty multiplier	0.84 → 1.16	1.0
19. DLECON = thermal conductivity dial multiplier	0.6 → 1.3	1.0
20. DLGAP = additive uncertainty in radial gap size	±1.5 mils	0.0
NOB = 0 → fresh fuel		
= 1 → once burned fuel		
21. DLDEC = decay heat multiplier	-0.06 → 1.0	0.0

* Late in the study, a coding error was found which had prevented the implementation of this dial.

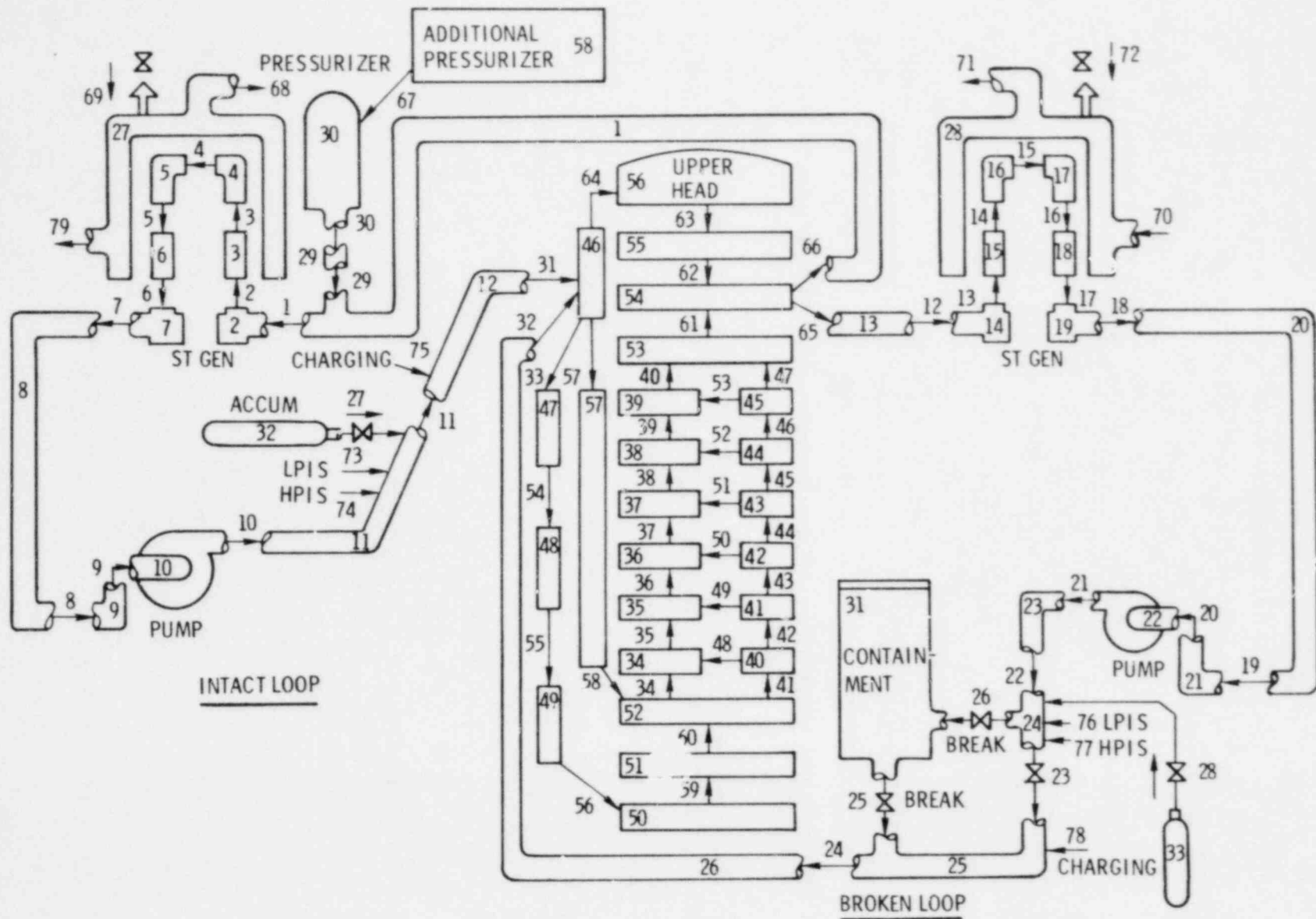


Figure 3-1 RELAP4 Nodalization for BE/EM Study

Using the RELAP results, a set of 12 response models was constructed, employing a variety of modeling philosophies. We were thus able to compare the models' results with each other, thereby assessing the reasonableness of the results.

All the response surface models displayed virtually the same results for relative influence of input variables on PCT. Furthermore, there was very good agreement among the models on the magnitude of the sensitivity of PCT to changes in those variables. For the ranges of variation used in this study, the three fuel-behavior-related parameters were found to be of dominant influence on the PCT models. These are, in approximate decreasing order of importance, gap width, total peaking factor, and fuel thermal conductivity. PCT sensitivities to one standard deviation change in these variables were, roughly, 80°, 60°, and 40°F, respectively. Other variables of importance were Condie-Bengston film boiling heat transfer coefficient, friction and form loss factor for two-phase flow, the slip correlation multiplier, and power level. For this group of variables, the magnitudes of PCT sensitivities were approximately 20°F.

Additional calculations, with variations of single parameters, showed good agreement with the response surface results. Also, examination of RELAP results other than PCT yielded no apparent physical inconsistencies with the influence ranking of the statistical analysis. We feel this study has demonstrated the feasibility of performing a response-model-type uncertainty analysis of a reactor accident sequence, using a large computer code and a reasonable number of calculations.

A final report is being prepared for this portion of the statistical LOCA analysis program. The report² treats the results of the study, and the statistical methods used, in much greater detail than is presented here, and its perusal is recommended to the interested reader.

3.3 The Metal-Water Reaction

Quite late in the course of this program, we discovered that the "dial" on energy produced by zirconium oxidation would only have an effect

if no pin swelling or flow blockage models were used. Since this is not the case for our calculations, the first 134 runs contained no variations of the metal-water reaction (MWR). Six calculations were performed with the dial implemented, and PCT comparisons with otherwise identical runs appear in Table 3-II. As may be seen from the table, the effect of MWR only begins to become important for temperatures above about 2000°F. In fact, one may observe that for the temperatures shown under 1900°F, the effect of MWR is masked by other variables (not input parameters) in the calculations, such as timestep differences. The strong temperature dependence of MWR is consistent with analytical results obtained with parameters in the approximate range seen in the RELAP calculations. This was also borne out by calculational experience. In one member of the statistical variable set, the energy production rate at one of the heat slabs exceeded the heat removal rate so much that the local temperature increased enough to cause failure of the calculation (see Figure 3-2).

TABLE 3-II

Metal-Water Reaction, "Star Points"

<u>T_{HIGH} (°F)</u>	<u>T_{LOW} (°F)</u>	<u>Sensitivity (°F/σ)</u>
1850	1857	- 2
1878	1852	9
1890	1883	2
2151	2077	12
2151	2105	15
2267	2185	27

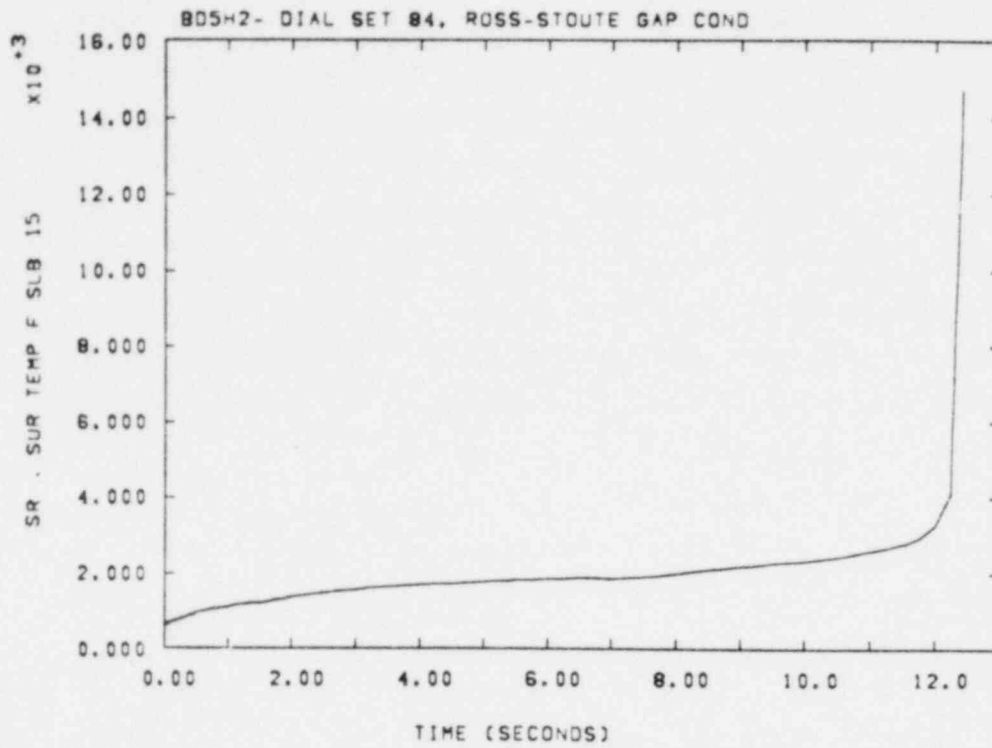


Figure 3-2 Clad Temperature, DS 84, Slab 15

We attempted to include the effects of the MWR sensitivity runs in the response surface models, but were unsuccessful. We assume that this is because of the small number of results available, and the biased nature of the sample for MWR-varied runs. It seems improbable that statistical results for this variable can be obtained without a fairly large number of additional calculations.

3.4 Pin Pressure Initialization

Evidently because of the wide range of input conditions used in the statistical study, a few of our calculations failed to initialize properly. The failures were due to lack of convergence in an iterative procedure used to solve for fuel pin initial conditions, given surface temperature and cold dimensions. The iteration was becoming "trapped" in a set of internal pin pressures, and exceeding the number of trials allowed.

By inspecting the behavior of the iteration, we learned that the range of pressures being attempted varied from a few to about 80 lb/in². Since the pressure values being calculated were around 1900 lb/in², we altered the code to print an informative message, use the last iterate, and proceed. Conversations with R. J. Sand at INEL yielded no knowledge of any severe consequences of following this procedure, and revealed that personnel at Savannah River Laboratory had experienced the same problem. Also, at that time, he was just beginning work on modifying the iteration scheme in order to improve convergence.

After developing and testing the modifications, Sand sent them to us, and we incorporated them in our version of RELAP. In order to assess the consequences of our previous method of treating the initialization problem, we reran the calculation which had been iterating over the broadest pressure range. The resulting internal pin pressure was about 40 lb/in² higher, within the iteration band of the original calculation.

Comparison of plot output from the pair of calculations showed, in most quantities, undetectable differences. The fuel stored energies and lower plenum pressures (Figures 3-3 and 3-4) are examples of the close agreement between the calculations. Midcore flows and volume temperature differed only slightly between the two runs (Figure 3-5 and 3-6). The most significant difference we observed between the two calculations was a change in PCT of approximately 40°F, with the new initialization procedure yielding the lower value (Figures 3-7 and 3-8). Since this PCT difference should be the largest we could have caused by ignoring the initialization error, we believe that procedure had no serious consequences in the statistical analysis.

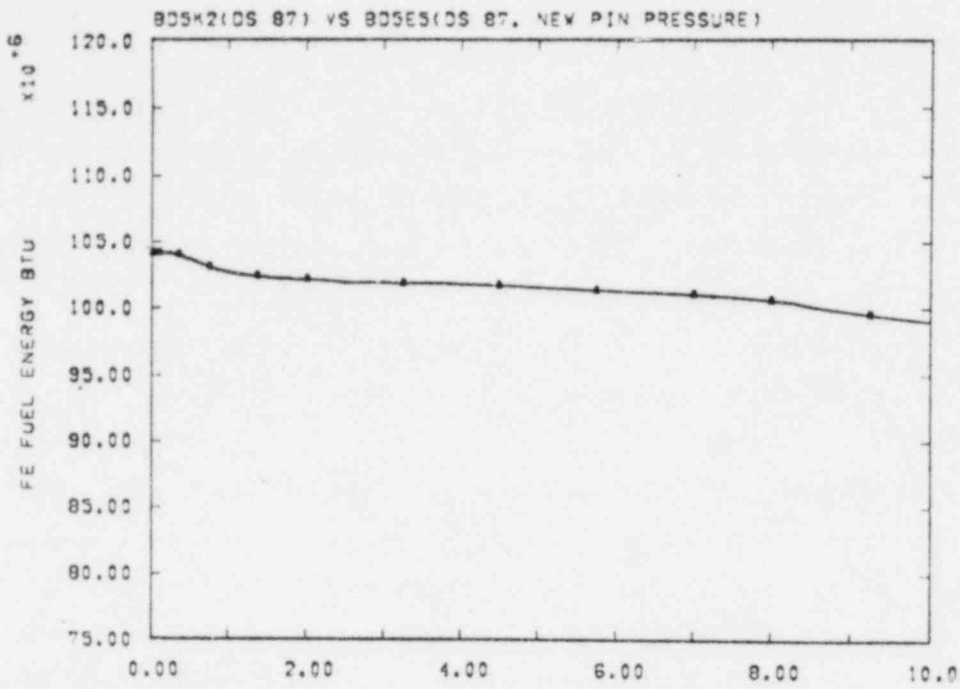


Figure 3-3. Fuel Stored Energy, Effect of New Pin Pressure Initialization

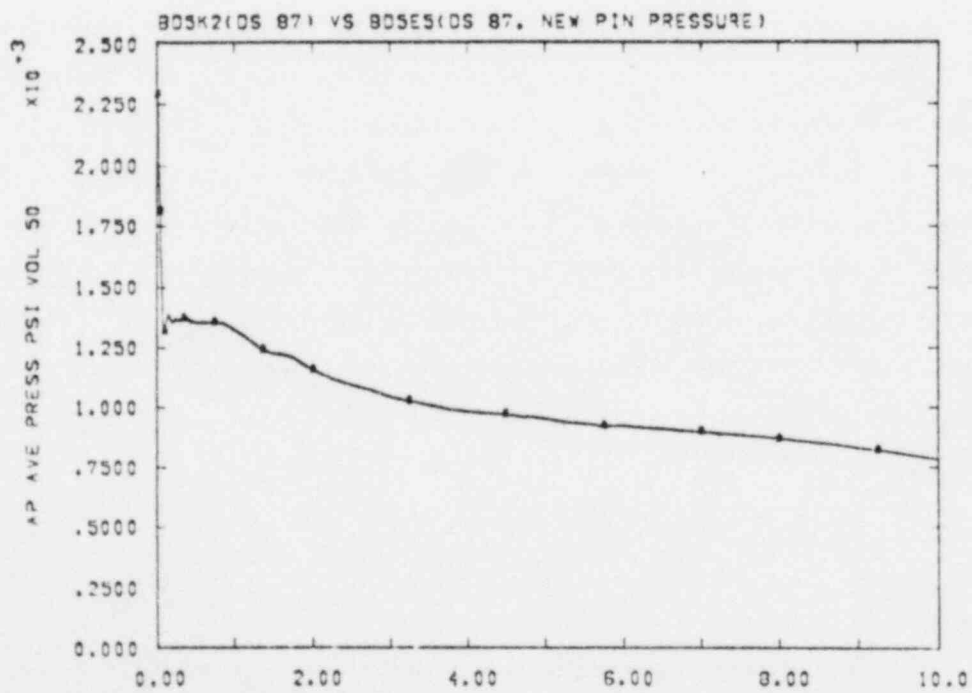


Figure 3-4. Lower Plenum Pressure, Effect of New Pin Pressure Initialization

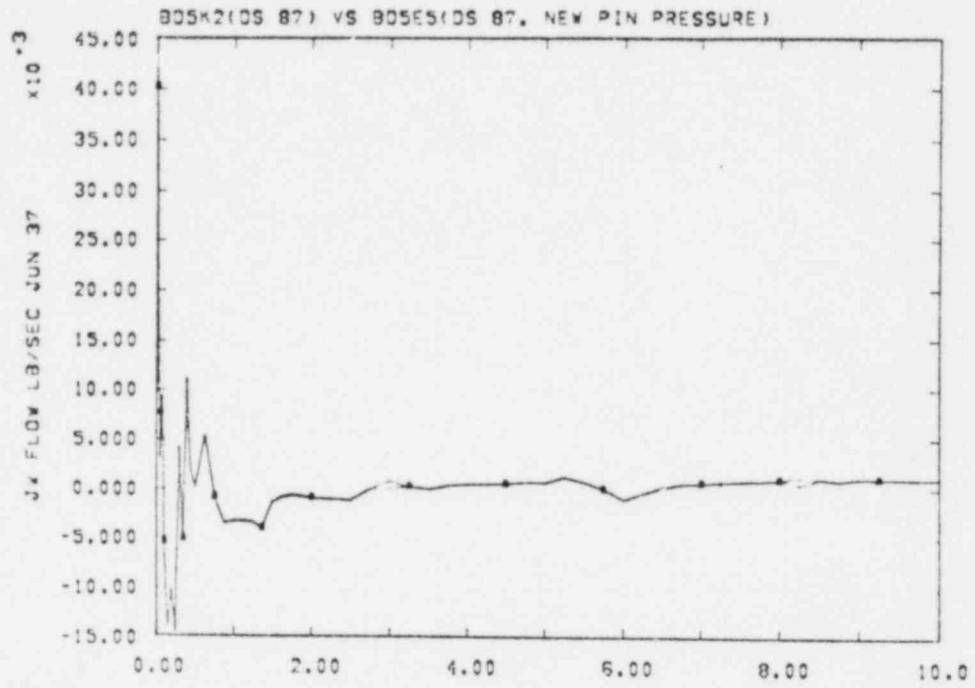


Figure 3-5. Middle Average Core Flow, Effect of New Pin Pressure Initialization

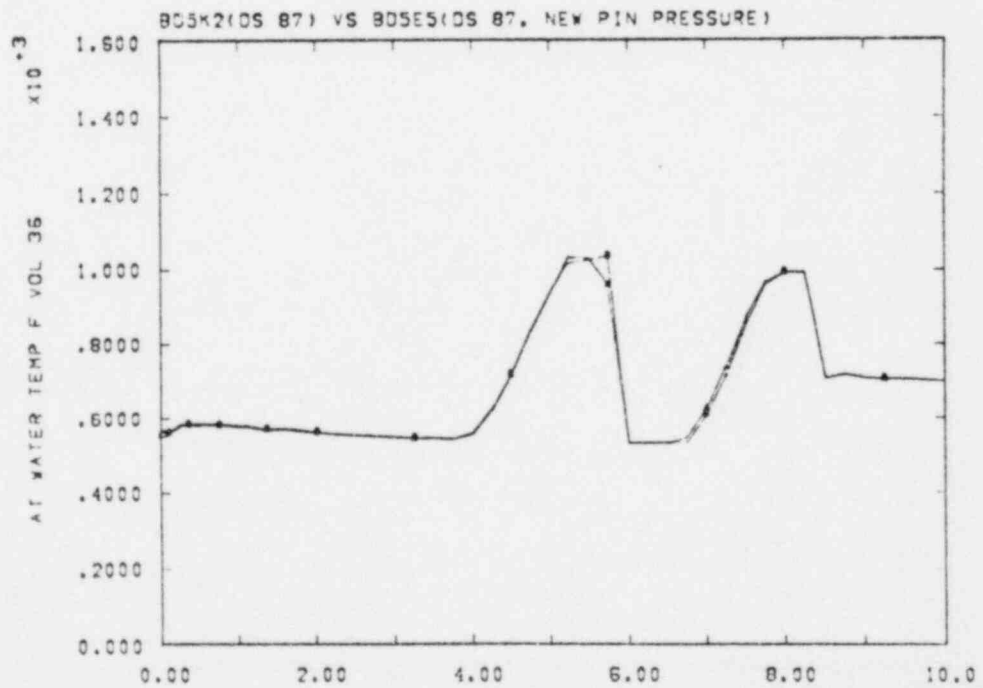


Figure 3-6. Temperature in Middle Average Core, Effect of New Pin Pressure Initialization

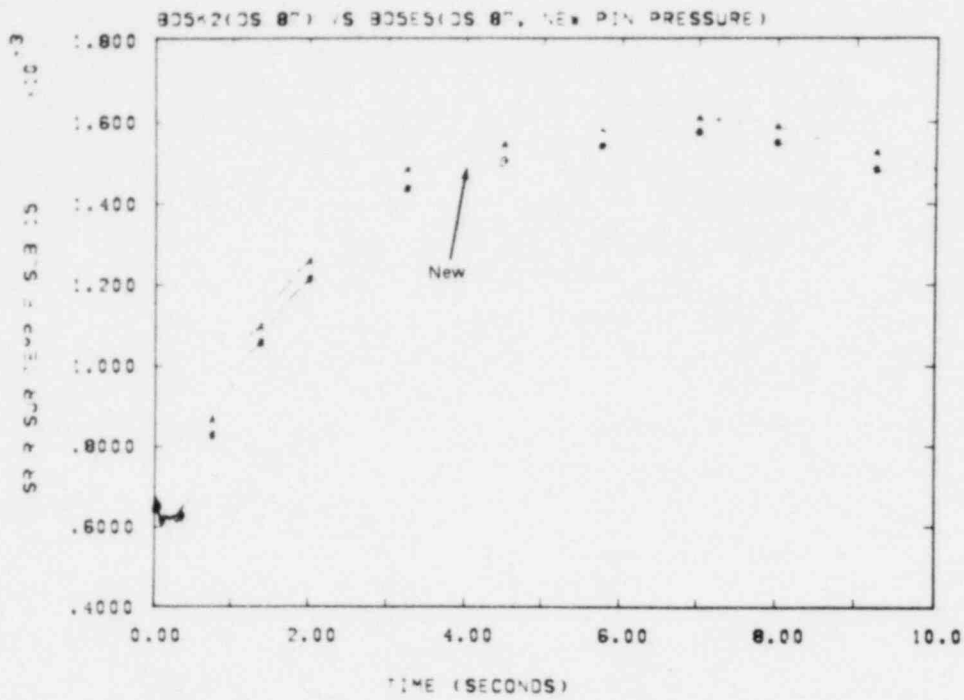


Figure 3-7. Slab 15 Surface Temperature, Effect of New Pin Pressure Initialization

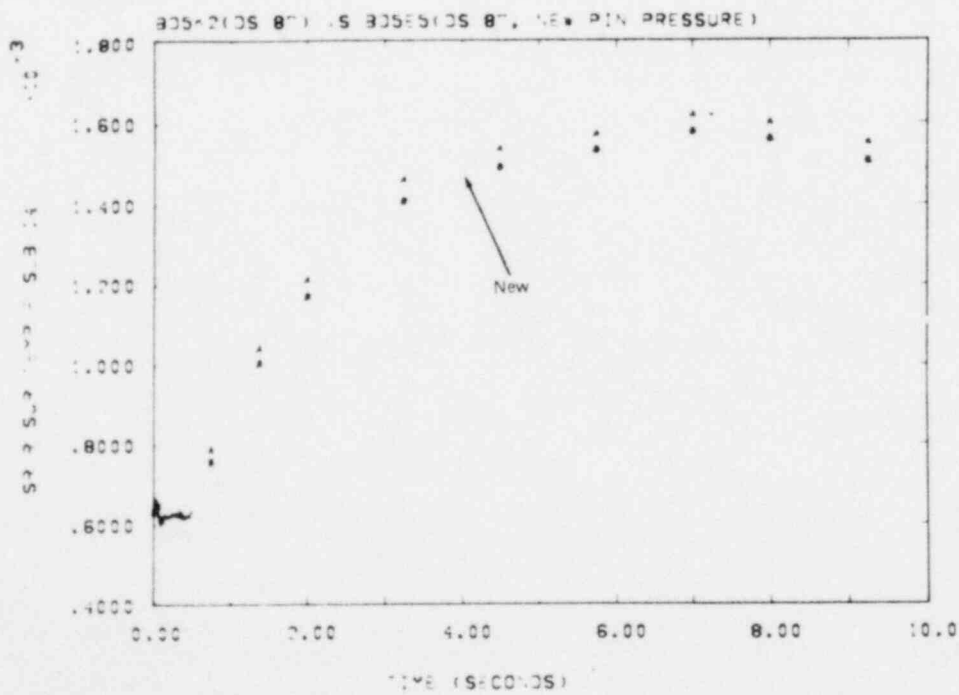


Figure 3-8. Slab 14 Surface Temperature, Effect of New Pin Pressure Initialization

3.5 Reproducibility of Calculated Results

Quite late in this program, we accidentally discovered that our combination of RELAP, computer operating system, and job execution procedure could produce different results for identical input sets. The discovery occurred when one calculation seemed to have disappeared from the system, so it was resubmitted; on resubmission, an unexplained system-generated job rerun occurred after the RELAP calculation was complete. Subsequently, output from the original run was located, so that we had three calculations that should have been identical, but were not. This event caused a great deal of concern and we began a search for its possible source.

Of the trio of runs which raised the question of reproducibility, two produced the same PCT result. However, the three calculations were all terminated by different RELAP-detected errors, and a detailed comparison of output showed divergence of results as early as 9 reactor seconds. Five more calculations with this input set, including three restarts from one of the error-aborted runs, produced neither the error previously observed nor divergences in output. Sandia's computer operations personnel stated that they knew of no hardware or software error existing in the system at this time. The RELAP program, therefore, seemed the most likely source of the discrepancies.

Our original suspicion was that the code was in some way using a quantity which had not been properly initialized. RELAP is capable of accessing memory areas that are not explicitly declared in any storage allocation statements. Because of this, the job procedure used to preset storage to an "illegal" value did not reach all of the areas of memory that could be used by RELAP. After some investigation, a method was developed to control the initial state of all the memory being used. This method consists of loading and executing a "dummy" program, before the loading and execution of RELAP. The dummy program performs no function other than the declaration of storage areas sufficient for RELAP execution, thus allowing full presetting of the core.

For the purpose of broadening our information base on the possible frequency of irreproducible results, 43 more recalculations were performed with 14 of the statistical input sets. In these calculations, various legal and illegal numbers were used for presetting storage, both the old and new job procedures were employed, and both of Sandia's CDC 7000 series computers were used. A number of the dial sets selected for these runs were those with PCT results or temperature histories that seemed somewhat inconsistent, statistically, with the response model predictions (i.e., large RMS residuals). Many of these calculations were run for a reactor time of at least 20 s; most were carried out at least past the time of PCT. The set also included some short and repeated restart runs.

Of the 49 runs performed for comparison purposes by this point, only 2 differences in PCT were observed that might have consequences for the statistical analysis. These differences (20° and 62°F) occurred for calculations with the same dial set, again in conjunction with a system-caused rerun of a job for no apparent reason. (The dial set which produced these differences was one which, because of the difficulties with the metal-water reaction parameter, was not in fact used as part of the input for the response surface analysis.)

We observed 5 other divergences in output in the set of 49 calculations; in none of the 5 was there a difference in PCT as large as 1°F. Clearly, such small differences could have no significant impact on the statistical analysis. It should also be emphasized that differences in results were detected by full comparison of output files, to the limits of machine accuracy.

In another effort to assess the frequency of possibly irreproducible results, we performed a set of 100 calculations with input identical to that which had produced the significant PCT differences. Since those differences were felt to have stemmed from divergences very early in the calculations, this set of runs had a small time limit (approx. 0.05 s reactor time). The runs were divided into four equal groups: each of the two computers was used with either the old or the new job control sequence.

Complete comparisons were then performed on the output. Apart from a frequent shift in the memory location of the first word of executable RELAP code, no differences in results were observed in the entire set of 100 runs. The memory shift appeared only in runs using the old job configuration. We also note that in all our investigations, we found no evidence that the new job control procedure would fail to give reproducible results.

In summary, we were not able to uncover any clear reason for the occasional lack of reproducibility of RELAP output. The combinations of values used to preset memory were expected to force the code to behave in a way which would provide some clue, but that expectation was not fulfilled. We were able, however, to construct a job execution procedure which never yielded self-contradictory results. This method will, of course, be used in all subsequent calculations.

Two points should be emphasized: (1) the possibility exists that undetected errors were occurring in our computing system at the times we experienced difficulty and (2) recalculation of some of the data actually used in the statistical analysis never showed divergences of numerical significance to the study.

3.6 TRAC Progress

Because of the very high priority given by the NRC contract monitors to the performance of TRAC calculations for the UHI Semiscale program this quarter, only a small effort was devoted to the TRAC statistical LOCA program. A nonstandard version of the newly released TRAC-PIA code was generated which had sufficient small core memory and large core memory allocation to run a full-scale PWR LOCA analysis. That version of the code was then used to run a steady-state calculation for the sample PWR problem given in the DRAFT TRAC-PIA manual. The calculation was run to 200 s of problem time without satisfying the 1% steady-state convergence criterion used, but most of the variables appeared to be well stabilized at that time. Only the upper head region appeared still to be undergoing significant changes. That was probably caused by the limited flow area from the

upper head to the lower parts of the reactor vessel. The results obtained for the calculation appeared to be in good agreement with the results obtained at Los Alamos. This suggests that no basic errors were created in converting TRAC-PIA to the Sandia computer system.

3.7 References

¹M. Berman, ed, Light Water Reactor Safety Research Program Quarterly Report, April-June 1978, SAND78-1901 (Albuquerque: Sandia Laboratories Light Water Reactor Safety Department, Jan 1979).

²G. P. Steck, M. Berman, and R. K. Byers, Uncertainty Analysis for a PWR Loss-of-Coolant Accident, SAND79-1206 (Albuquerque: Sandia Laboratories, nd). To be published.

4. UHI Model Development

(R. K. Byers, T. J. Bartel, L. D. Buxton,
R. K. Cole, M. Berman)

4.1 Summary

Upper head injection (UHI) is a recent feature for emergency core cooling, developed by Westinghouse for use with pressurized water reactors (PWRs) having ice condenser containment systems. Analytic methods (to date, principally RELAP4) are thought to be inadequate in treating some of the important phenomena associated with the behavior of a UHI-equipped PWR during a loss-of-coolant accident (LOCA). Areas where improved treatment is felt to be required include, but are not limited to, top quenching in the core, two-phase flow with slip, and upper head draining during refill. Sandia is engaged in a program intended to enhance the ability to analyze these and other important phenomena.

During the quarter, we continued our efforts to find a means of incorporating the Westinghouse-Zuber slip correlation in RELAP4/MOD5 in a way that would permit stable and reasonable results to be obtained. RELAP calculations were also analyzed in an attempt to isolate the source, or sources, of results we think are unrealistic. Investigations were also made of the effects of varying quench criteria in the core, and the influence of upper head draining on lower plenum refill.

Work continued in the application of RELAP to the analysis of the reflood phase of a LOCA. A version of the FRAP-T4-LACE code was received which will permit specifying initial conditions for the flood calculations. For the use of the reflood mode of RELAP, questions were addressed concerning the effect of the nodalization on computational stability, the influence of the carry-out-rate fraction model, and the means of using results of the blowdown calculations in initializing the reflood phase.

Various versions of the TRAC code were employed in calculations of the Semiscale MOD3 Series 7 experiments. This configuration, while not a UHI one, was employed in order to build confidence in the methods being used, by comparison with experimental results. Support was provided to LASL, in the form of computer time, consultation on coding and nodalization errors, and output handling. TRAC was also used in a sample calculation of a full scale, four loop PWR. Plans for the future include calculations for the UHI test series (Series 8) of Semiscale MOD3.

4.2 UHI RELAP Blowdown Calculations

In this section, we present some of the results of various calculations performed during the quarter, and comparisons with previously obtained results. Calculations were performed with a modified core slab quenching criterion, and with an altered definition of junction void fraction for slip velocity calculations. The nodalization we have termed "UHL2" (Figure 4-1) was used, and salient features of the calculations are listed below:

- FT - Sandia-Westinghouse quench, generic MOD5 slip
- FQ - UHL2FT, but relaxed quench criterion
- G - UHL2FT, but spline-smoothed Westinghouse-Zuber slip
- H - UHL2G, without smoothing; modified junction void fraction
- H2 - UHL2H, but water packing option on at 2 s, not 10 s

4.2.1 Effect of Relaxed Quench Criterion

The logic for quenching of core slabs currently being used is a Sandia modification of a Westinghouse model based on data for reactors with UHI. In the event that criteria based on temperature, pressure, flow, and quality are met, heat transfer coefficients are raised to a proprietary value if they currently lie below that value. This process takes place over a period of time for average core slabs and immediately for slabs in the hot assembly. After a delay, Sandia's version of this model allows the usual RELAP heat transfer logic to regain control.

One of the criteria to be satisfied in the above scheme, at certain pressures, is the presence of either single phase or two-phase co-current downflow. Because we had observed some instances of countercurrent flow in the hot assembly, we relaxed the criterion so that only liquid upflow would result in eliminating the possibility of quenching. Figures 4-2 through 4-5 demonstrate the results of this modification for calculations employing the MOD5 generic slip correlation. Heat slab surface temperature at the midplane of the core (Figure 4-2) is somewhat affected; temperatures at the top and bottom slabs (Figures 4-3 and 4-4, respectively) show much more significant differences. In keeping with the enhanced removal of heat from the core region, the rate of loss of fuel stored energy is larger with the relaxed criterion, and continues to be so over significant portions of the calculation (Figure 4-5). Additional evidence of reasonable behavior in the calculation may be seen in Figures 4-6 and 4-7, showing average temperature and liquid mass comparisons for the middle volume in the average core, respectively. The calculation with the less stringent quenching criterion (UHL2FQ) permits a larger energy absorption rate in the coolant for the period between about 10 and 20 s; the difference is sufficient to produce virtually complete vaporization of the fluid.

Neither the upper head draining nor the refill of the lower plenum are significantly affected by the quench criterion relaxation. The altered heat transfer in the core results in some differences in support column flow between 40 and 80 s (Figure 4-8); however, flow from the upper head ceases at virtually the same time for both calculations (Figure 4-8; see also upper head mass in Figure 4-9). Figures 4-10 and 4-11, showing masses in the two volumes used to model the lower plenum, display no large, sustained differences in refill behavior. Those figures, together with the previous two, also demonstrate a phenomenon we have observed in all our calculations with the UHL nodalization: complete refill of the lower plenum, and therefore the beginning of core reflood, does not occur until delivery of water from the upper head ends. This behavior is evidently due to the steam being generated in the core as water from the upper head encounters the hotter core slabs.

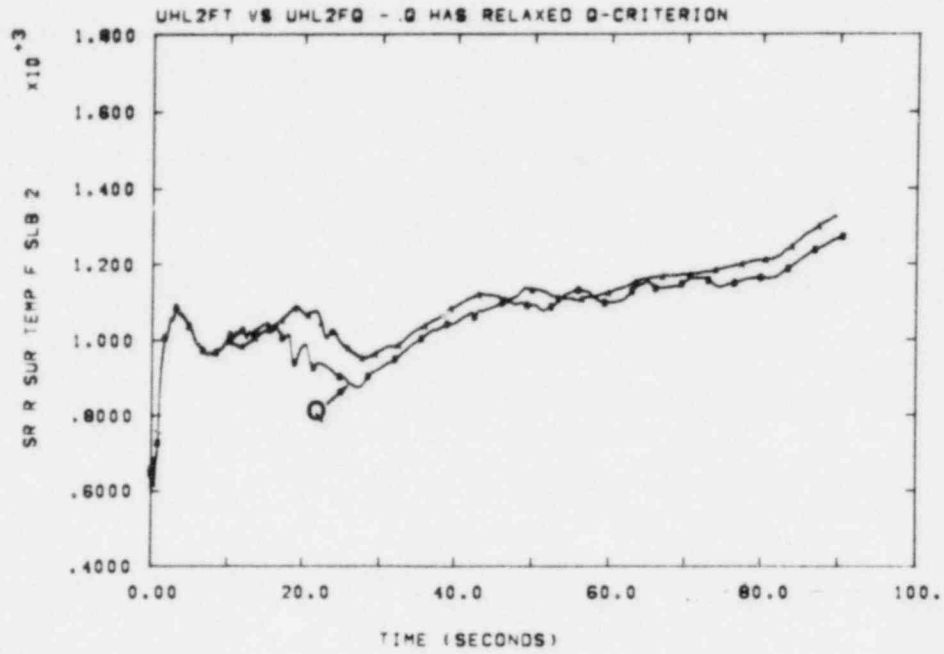


Figure 4-2. Midcore Heat Slab Temperature, Effect of Relaxed Quench Criterion

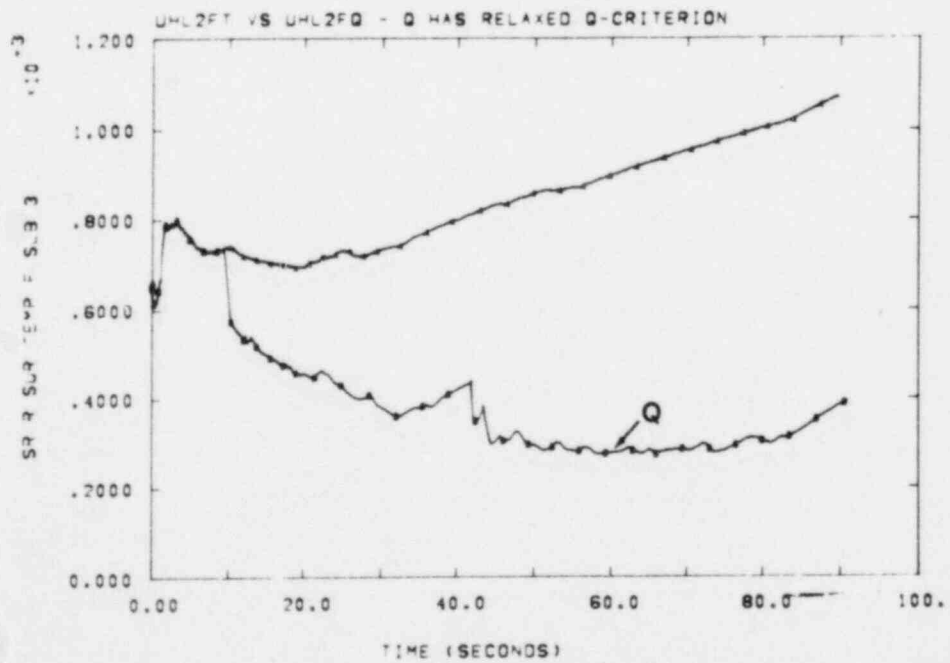


Figure 4-3. Top Core Slab Temperature, Effect of Relaxed Quench Criterion

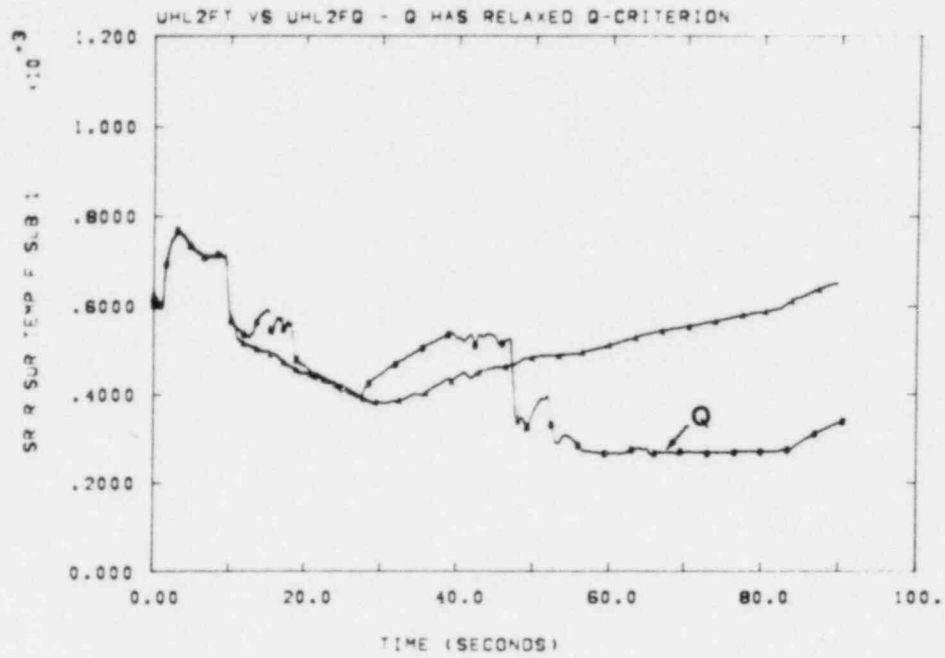


Figure 4-4. Bottom Core Slab Temperature, Effect of Relaxed Quench Criterion

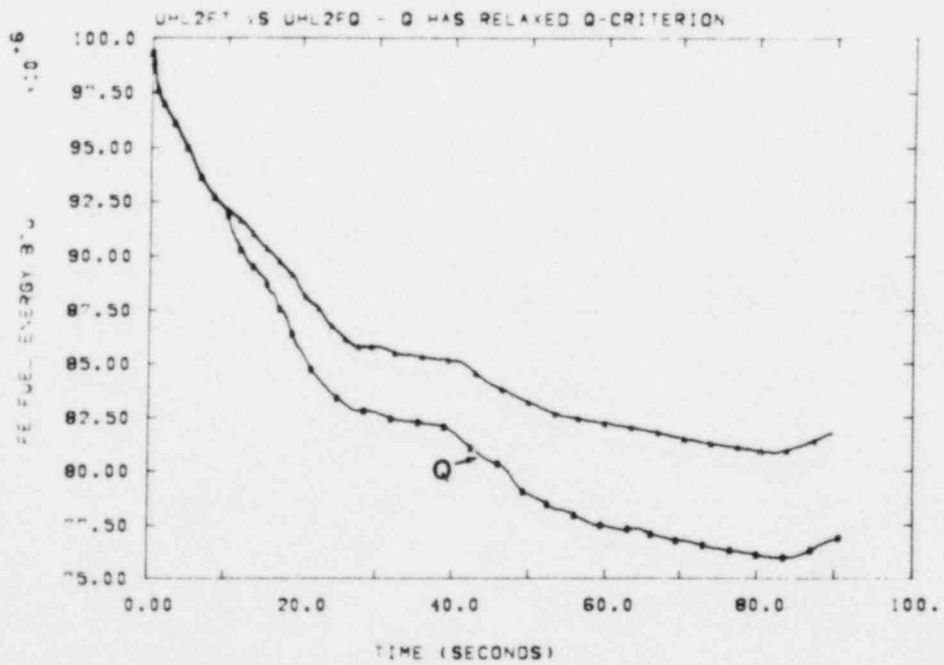


Figure 4-5. Total Fuel Stored Energy, Effect of Relaxed Quench Criterion

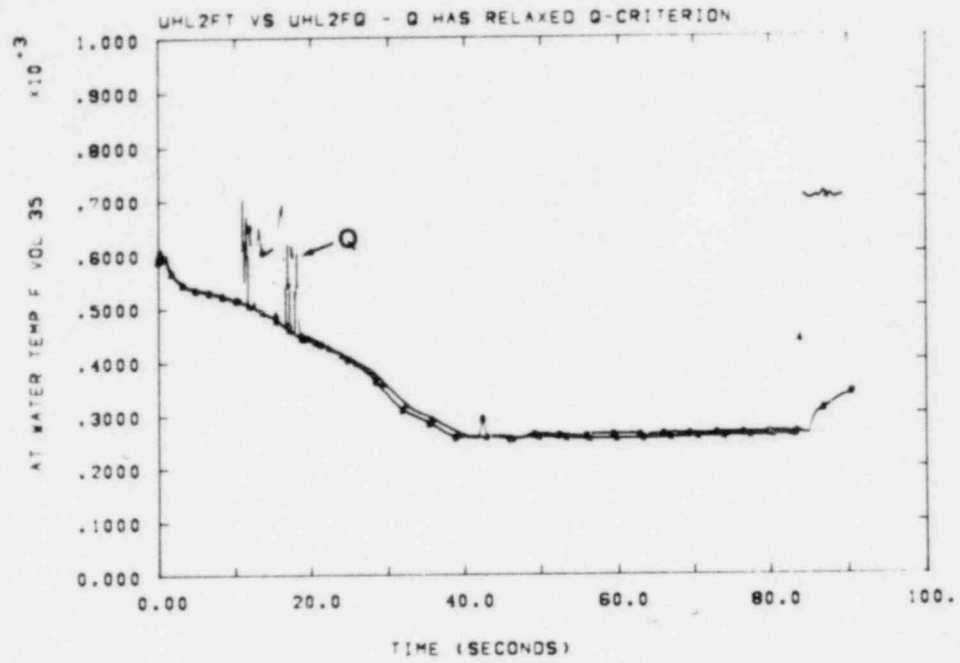


Figure 4-6. Volume Temperature, Middle Average Core Volume

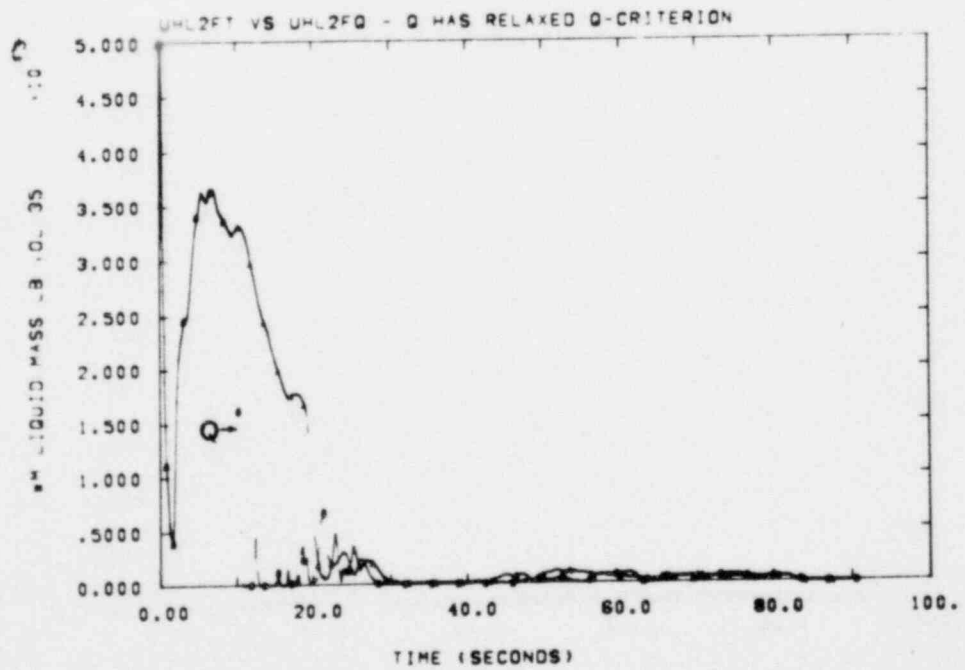


Figure 4-7. Liquid Mass, Middle Average Core Volume

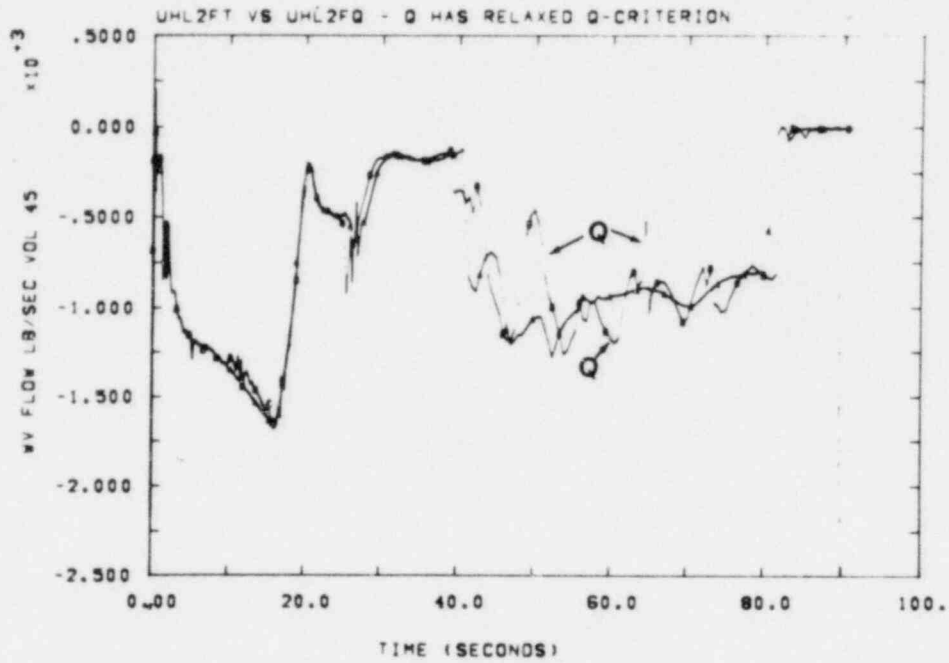


Figure 4-8. Support Column Flow, Effect of Relaxed Quench Criterion

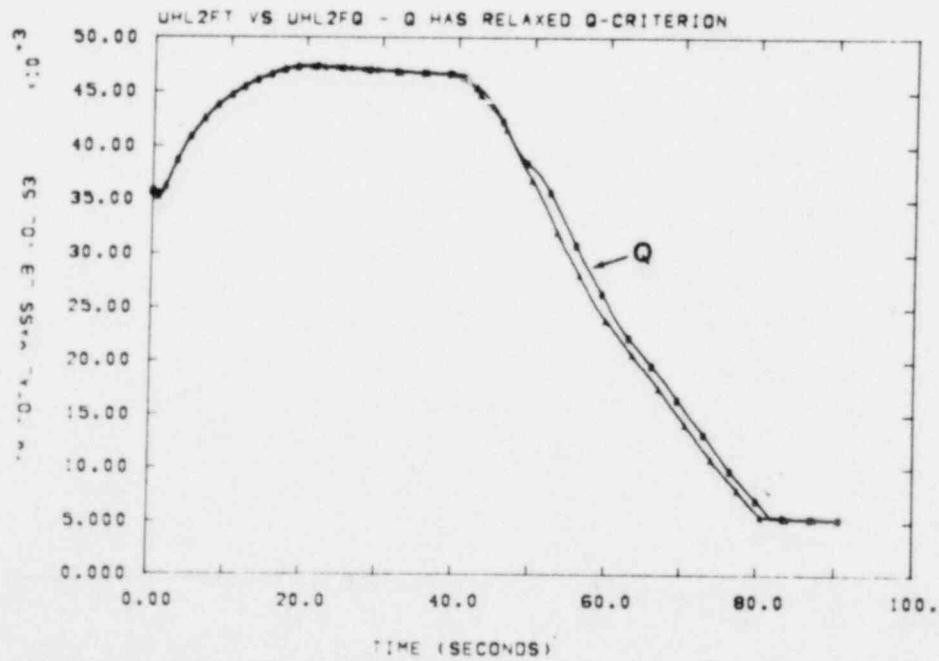


Figure 4-9. Mass in Upper Head, Effect of Relaxed Quench Criterion

12

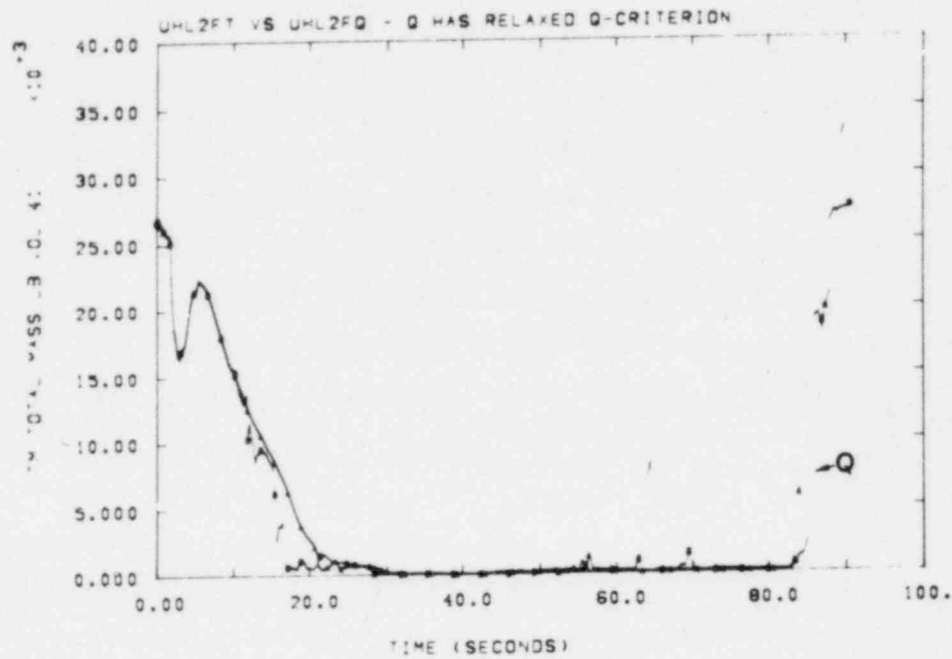


Figure 4-10. Mass in Upper Volume of Lower Plenum

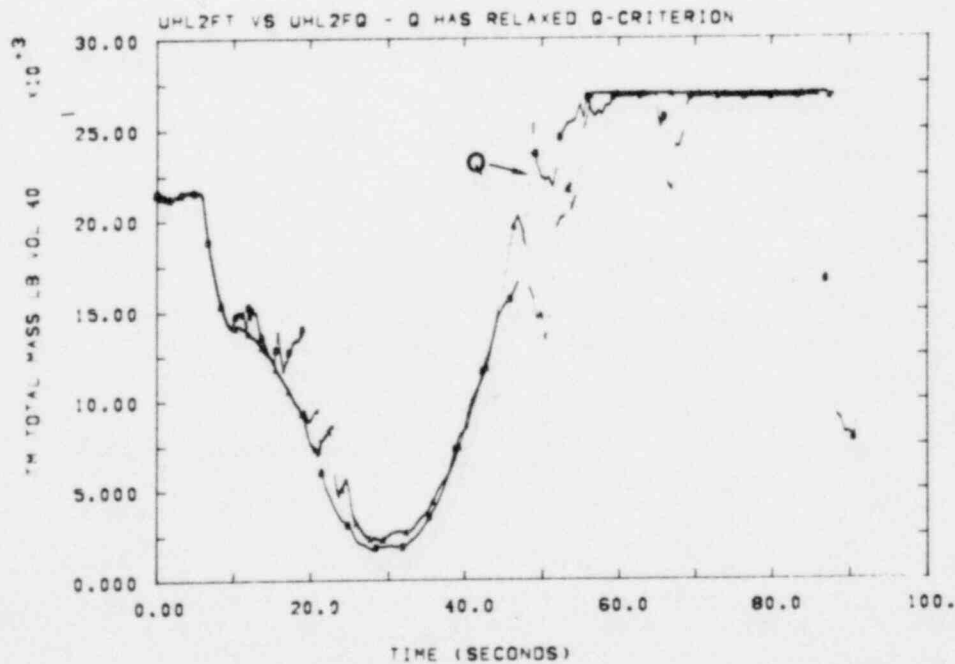


Figure 4-11. Mass in Lower Volume of Lower Plenum

4.2.2 Combined Effects of Slip Correlation and Relaxed Quench Criterion

In an attempt to obtain further understanding on which features of our modeling techniques are dominant in various parts of our calculations, we have compared results of the UHL2FQ run, described in the previous section, with those of UHL2G. The latter calculation employs the Westinghouse-Zuber (WZ) slip correlation modified so that the slip parameters have continuous first derivatives in the void fraction.¹ The quench criterion applied to core flow directions was the more stringent one, also described in the previous section.

Figure 4-12 shows slab surface temperatures at the bottom of the hot assembly for the two calculations. As in the previous comparison (Figure 4-4), the temperatures are quite similar to a time shortly before 30 s, when the calculation with generic slip begins heating up. In this case, however, the effect of the WZ slip model is to maintain the heat transfer calculations in the more efficient modes, so that, after re-quenching occurs in the run with generic slip, the temperature histories remain similar.

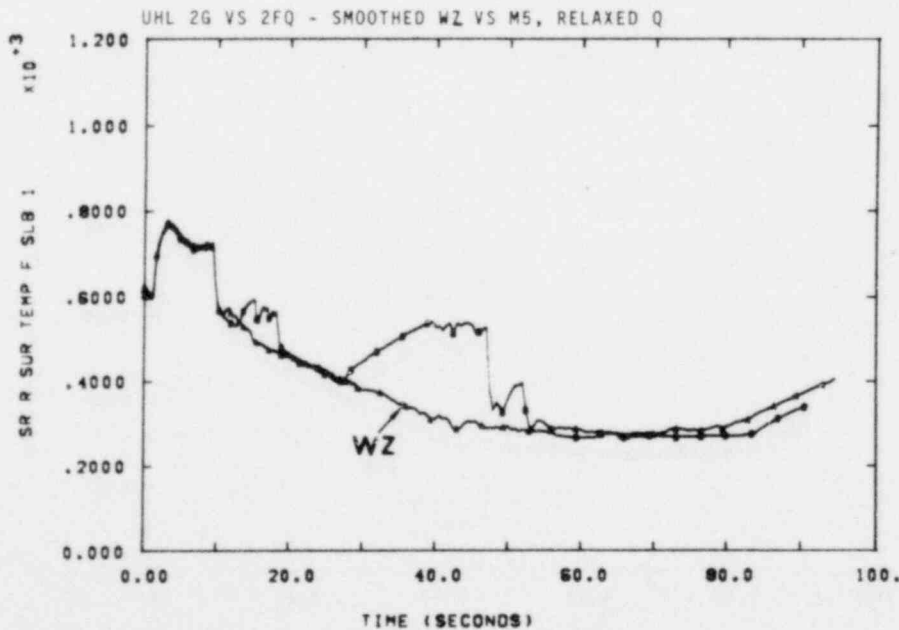


Figure 4-12. Clad Temperature, Bottom of Hot Assembly; Smoothed Westinghouse-Zuber Slip vs Generic Slip, Relaxed Quench Criterion

Effects of the WZ correlation at the middle elevation and top of the hot assembly are more dramatic (Figure 4-13 and 4-14). At the middle level (Figure 4-13) a quench episode is calculated with WZ slip; clad temperature there drops below 240°F, at about 45 s, before the slab begins to reheat. For slab 3 (Figure 4-14), as for slab 1, heat transfer modes permit more rapid removal of energy, and temperatures are comparable to those in the generic slip calculation.

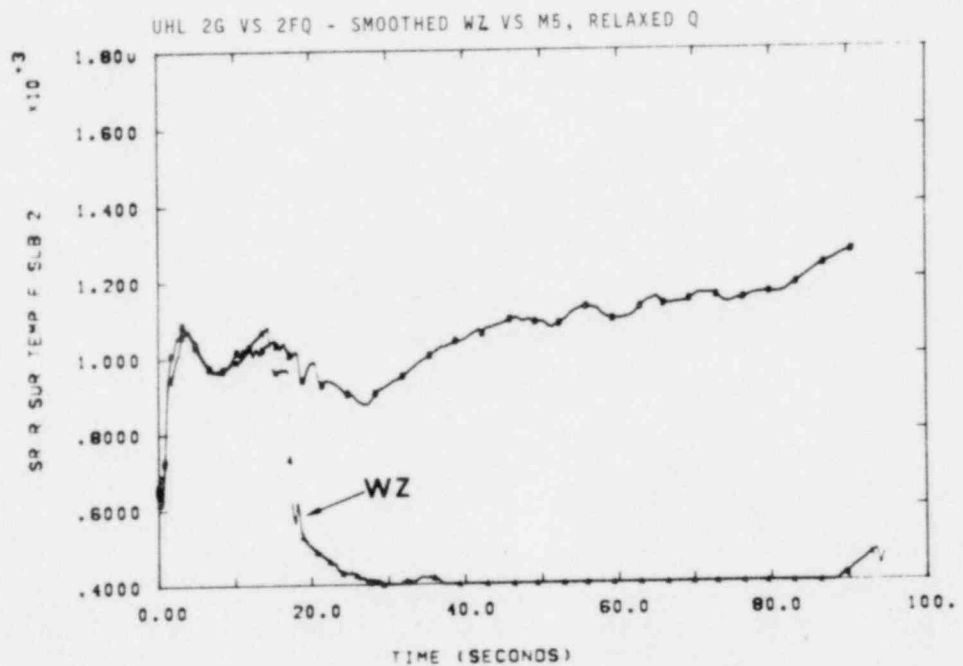


Figure 4-13. Midcore Hot Assembly Clad Temperature; Smoothed Westinghouse-Zuber Slip vs Generic Slip, Relaxed Quench Criterion

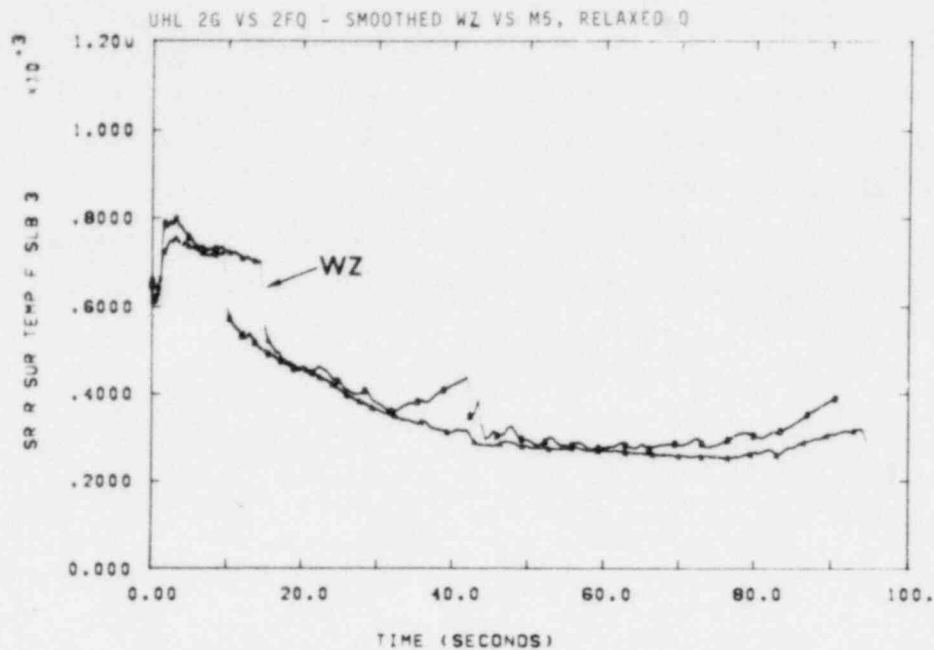


Figure 4-14. Top Hot Assembly Clad Temperature; Smoothed Westinghouse-Zuber Slip vs Generic Slip With Relaxed Quench Criterion

In the average core region of the nodalization, where most of the energy is concentrated, the WZ slip correlation does not result in as much similarity in temperature histories. Consequently, as shown in Figure 4-15, fuel stored energy is still higher than that for the calculation with MOD5 slip modeling; however, the difference is not as great as that produced by the relaxed quench criterion alone (Figure 4-5).

As may be expected, the different treatments of two-phase flow with slip also affect upper head drain and lower plenum refill. In comparison with Figures 4-8 and 4-9, differences due to WZ slip modeling are much more apparent in support column flow (Figure 4-16) and upper head mass (Figure 4-17). Differences due to the slip correlations in lower plenum refill also appear in mass histories (Figures 4-18 and 4-19), particularly in a loss of mass in the lower volume of the lower plenum, followed by refilling of that volume (Figure 4-19). We note again that the time at which draining of the upper head ceases compares very closely with that at which full refill of the lower plenum is approached.

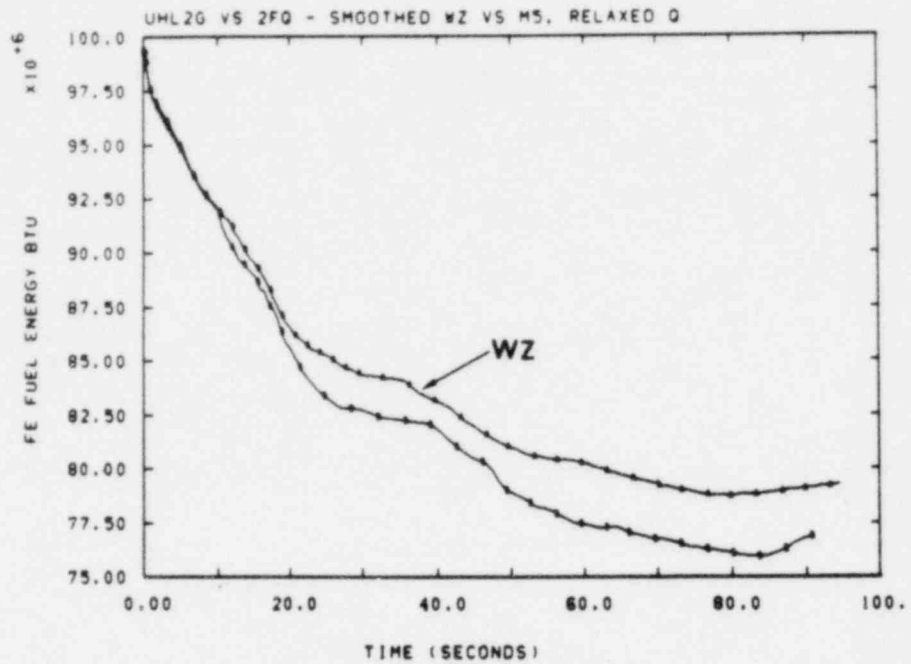


Figure 4-15. Total Fuel Stored Energy; Smoothed Westinghouse-Zuber Slip vs Generic Slip, Relaxed Quench Criterion

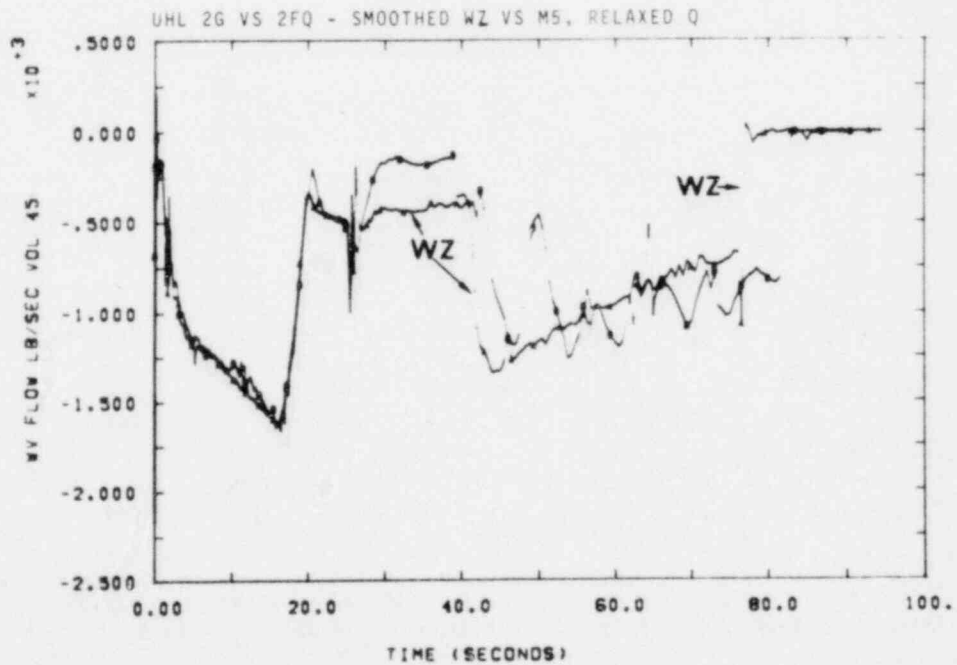


Figure 4-16. Support Column Flow; Smoothed Westinghouse-Zuber Slip vs Generic Slip, Relaxed Quench Criterion

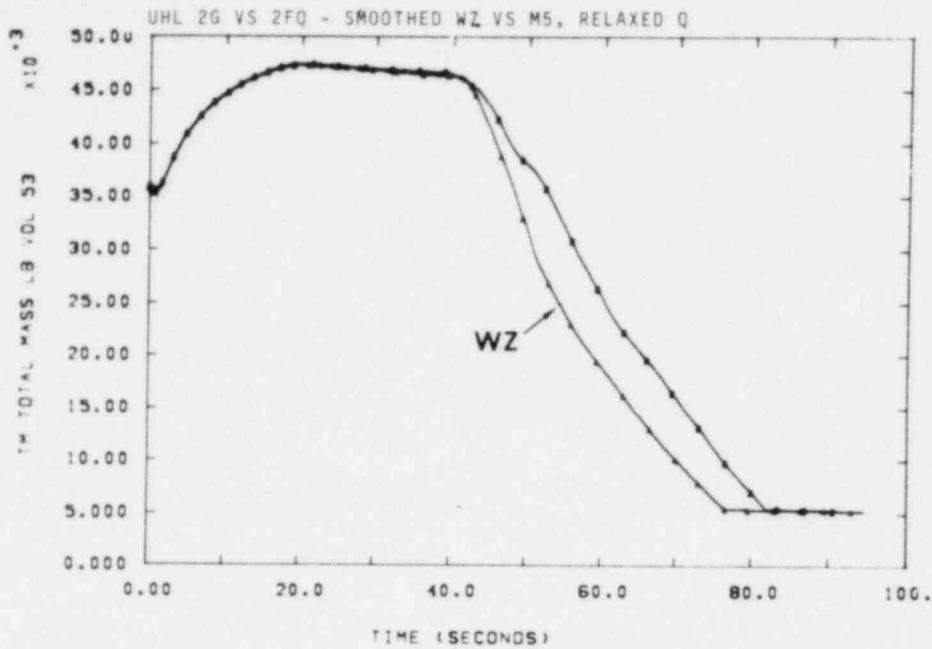


Figure 4-17. Upper Head Mass; Smoothed Westinghouse-Zuber Slip vs Generic Slip, Relaxed Quench Criterion

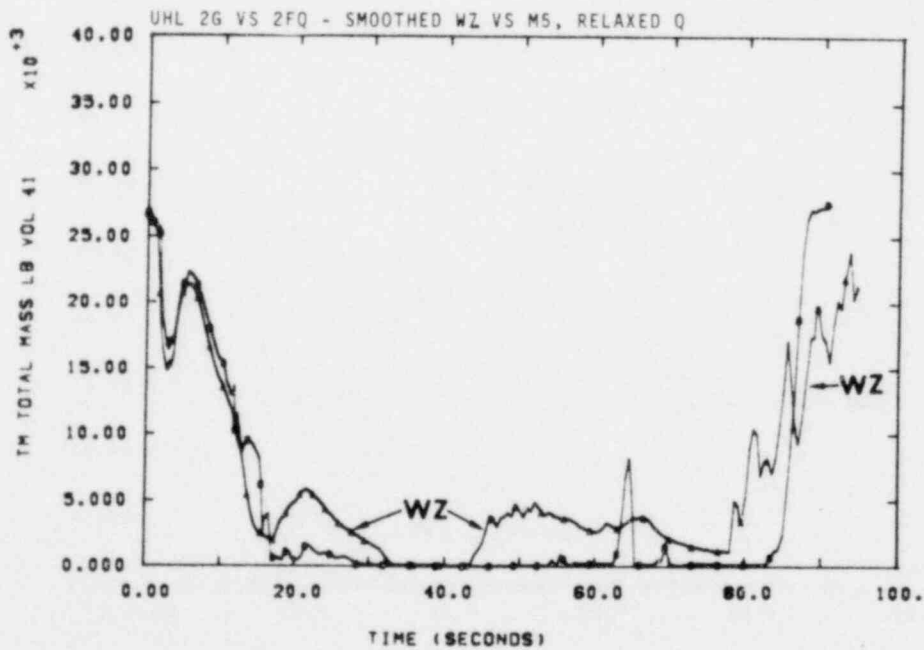


Figure 4-18. Mass in Upper Volume of Lower Plenum; Smoothed Westinghouse-Zuber Slip vs Generic Slip, Relaxed Quench Criterion

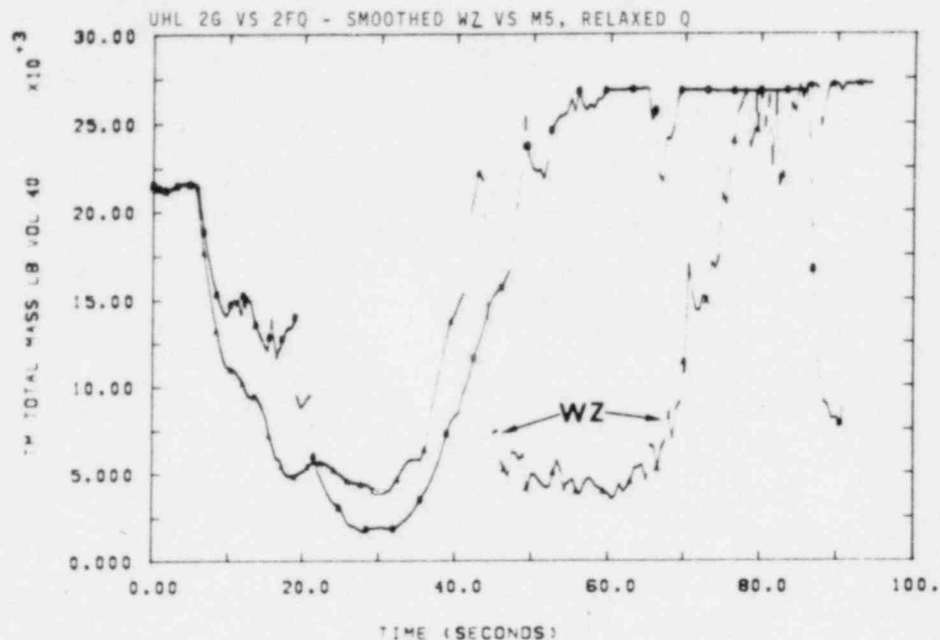


Figure 4-19. Mass in Lower Volume of Lower Plenum; Smoothed Westinghouse-Zuber Slip vs Generic Slip, Relaxed Quench Criterion

4.2.3 Slip-Related Investigations

It may be recalled from previous reports that the RELAP4/MOD5 generic slip correlation seems to produce results which run the most smoothly and efficiently, and contain less unrealistic oscillatory behavior. Various forms of the WZ slip correlation have been tried in our UHI calculations, and have persistently yielded flow and/or pressure oscillations in core and downcomer junctions. Modifications to the WZ correlation which first made the slip parameters V_{gj} and C_o continuous in junction void fraction, and then assured that their first derivatives were also continuous, did not seem to provide much improvement. We have also attempted to isolate mechanisms which might account for the beginning of the oscillations in question.

Figures 4-20 and 4-21, showing flows at the top and bottom of the downcomer, respectively, are typical of the comparisons between results using generic MOD5 slip and the WZ correlation. In this case, both V_{gj} and C_o have continuous first derivatives with respect to junction void fraction, but that property does not seem to have much overall effect on the calculations.

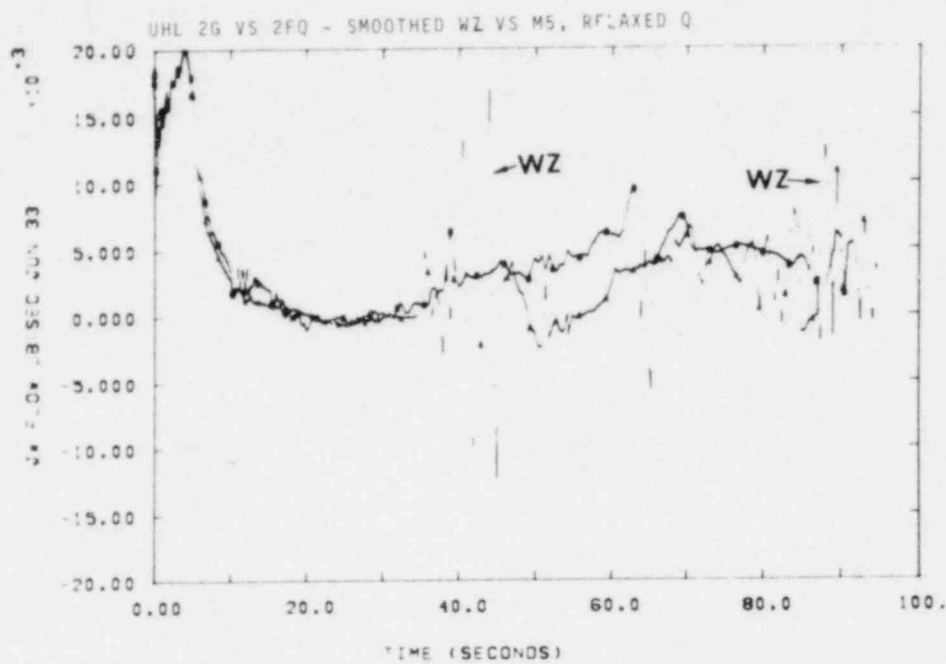


Figure 4-20. Flow at Top of Downcomer, Westinghouse-Zuber Slip vs MOD5 Slip

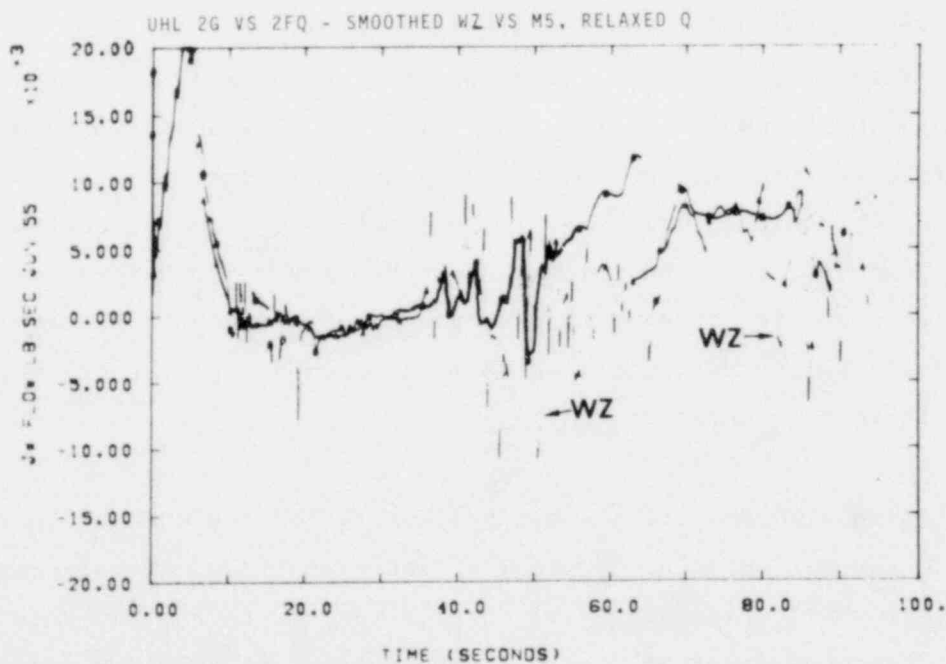


Figure 4-21. Flow at Bottom of Downcomer, Westinghouse-Zuber Slip vs MOD5 Slip

One feature of the slip calculation which we believed might be a source of difficulty is the choice of junction void fraction (α) to be used in the slip calculation. In particular, we suspected that this choice should depend on whether the conditions at the junctions were gravitationally stable (i.e., higher α above) or unstable. To investigate this question, we modified our version of the slip calculation so that the value of α results in a point on the flooding curve, or in a maximum gas flux for the gravitationally unstable case or minimum for the stable case.

The first calculation we attempted (UHL2H) using the above procedure terminated abnormally due to a failure in the steam table iteration. Examination of the results showed that this failure occurred very soon after the water packing correlation option was enabled. Because of this, we attempted another calculation (UHL2H2) in which the water packing option was applied at 2 s of reactor time, rather than 10 s. This calculation ran about 0.25 s longer than the previous one, then failed with the same error at the same location in the problem (the top hot assembly volume). Figures 4-22 and 4-23 display liquid mass flow at the bottom of that volume for the two calculations, and may indicate that the error is associated with the rather abrupt change in flow rates.

The steam table failure mentioned above is a frequent occurrence in many of our calculations. A common practice is to attempt circumventing the error by changes in timestep control. We have not yet tried this procedure, but intend to do so in order to see the effects of our slip modifications at later times. Also, we have noted that previous calculations that have used spline-smoothed WZ slip, with and without forcing C_o to be unity for co-current flow, compare in some ways very similarly as do smoothed WZ and generic slip calculations. This seems to indicate that treatment of the distribution parameter might be the dominant question.

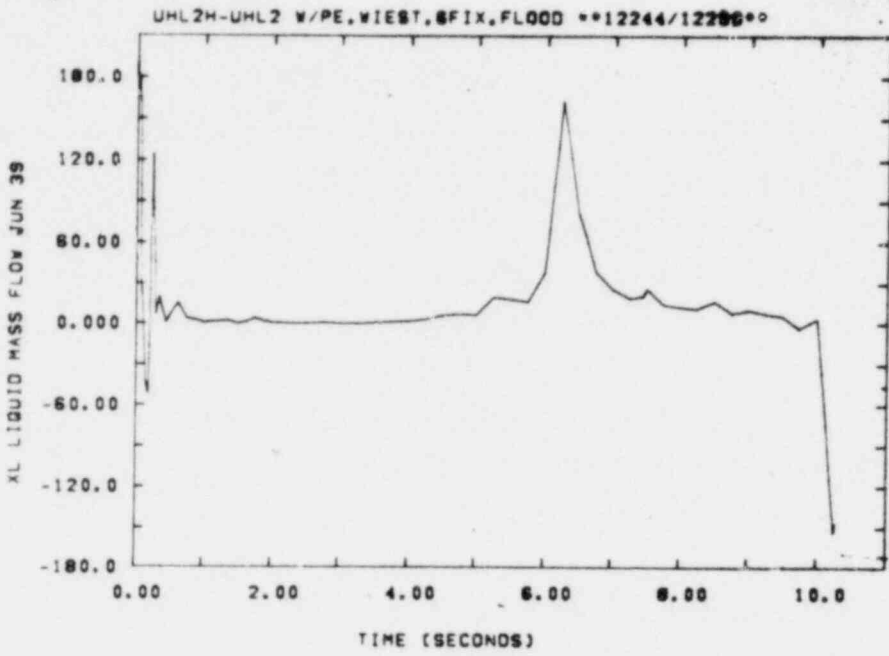


Figure 4-22. Flow Into Top Hot Assembly, Modified Void Fraction, Waterpack on at 10 s

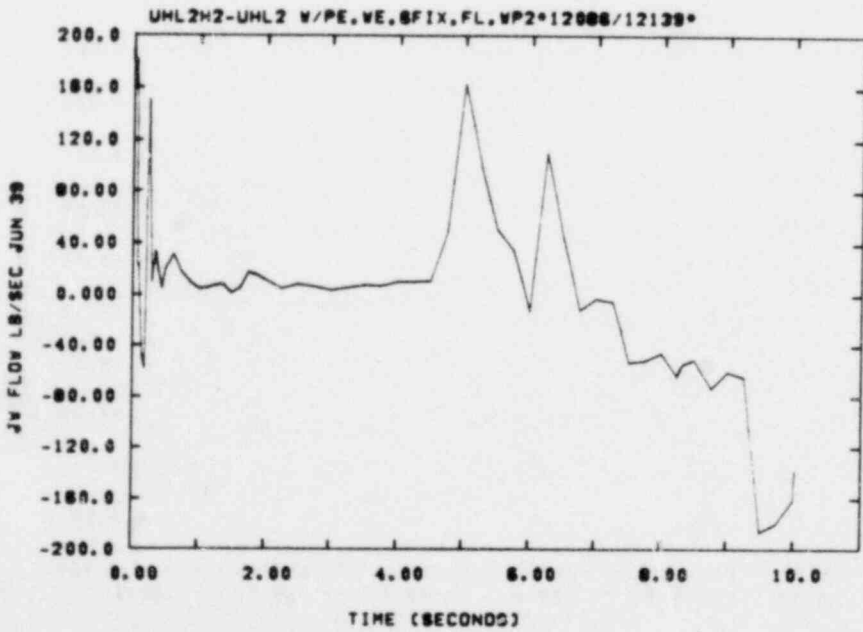


Figure 4-23. Flow Into Top Hot Assembly, Waterpack on at 2 s

4.3 UHI Reflood Calculations

4.3.1 Summary

This quarter, investigation continued into the use of the FLOOD mode of the RELAP4/MOD5 code to calculate the reflood portion of a loss-of-coolant accident occurring in a reactor equipped with an upper head injection system. The three main topics addressed were

- Sensitivity of the FLOOD calculation to the Westinghouse carryout-rate-fraction (CRF) model
- System initialization parameters
- Coupling of the LOCA blowdown calculation to the reflood phase for eight core power regions

This work determined that the implementation of the CRF model was critical to the computational stability of the code. Key questions concerning this model were resolved. Also, due to stability requirements, the intact loop accumulator fill was moved to the lower plenum. Finally, work began on a strategy to couple the reflood phase directly to the blowdown phase in a continuous calculation.

4.3.2 Carryout-Rate-Fraction Model

The Westinghouse Carryout-Rate-Fraction (CRF) model² was evaluated for computational stability and physical meaning. This correlation is a curve fit to PWR FLECHT data and is a function of several parameters. The definition of a quenched and unquenched region is critical for this model. Westinghouse (W) defines an unquenched region for the reflood phase as a region which did not quench during active upper head injection. Therefore, a core heat slab can be unquenched at the time of reflood but considered quenched in the CRF model.

A discontinuity in the CRF occurred as the core mixture level rose above the initial quench height, when calculated with the published W CRF model. However, it has been learned that W employs a 1-ft transition region to smooth this discontinuity. Therefore, the present CRF model was

modified such that the initial model temperature, T_{INIT} , is ramped linearly to 1600° . This procedure begins when the mixture level is 1 ft below the initial quench height. Figure 4-24 illustrates this strategy; this calculation is slightly conservative.

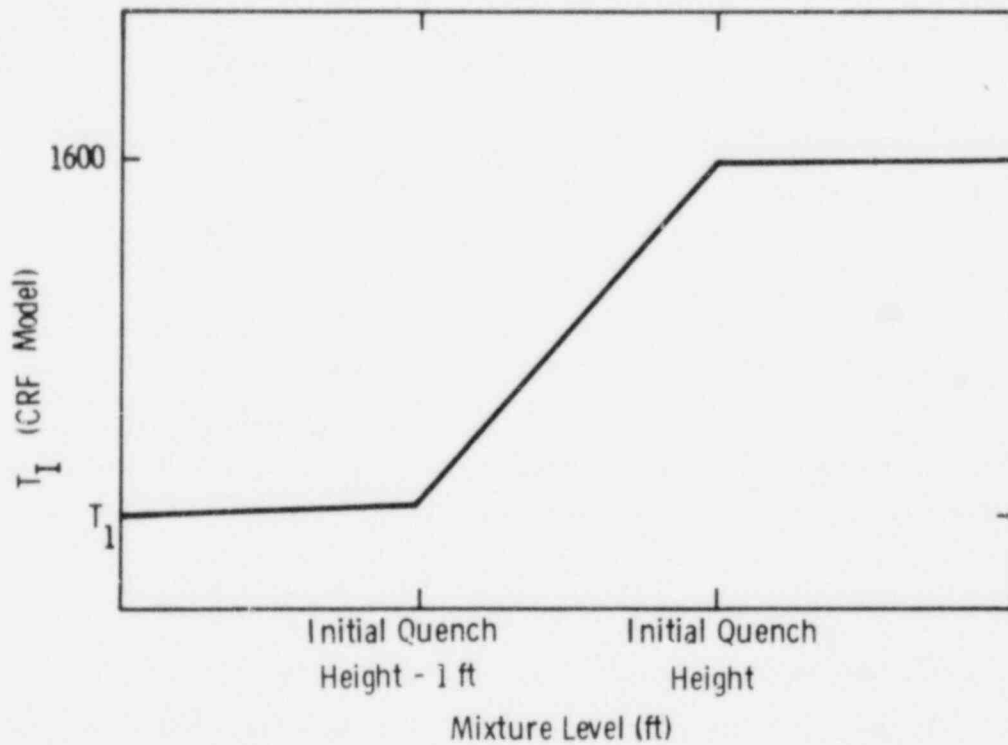


Figure 4-24. Temperature Transition Strategy

4.3.3 Nodalization

An effort was made during this quarter to resolve some questions concerning the FLOOD nodalization. Figure 4.25 shows the present FLOOD nodalization. The areas under investigation include the intact loop (IL) accumulator and the upper plenum initialization.

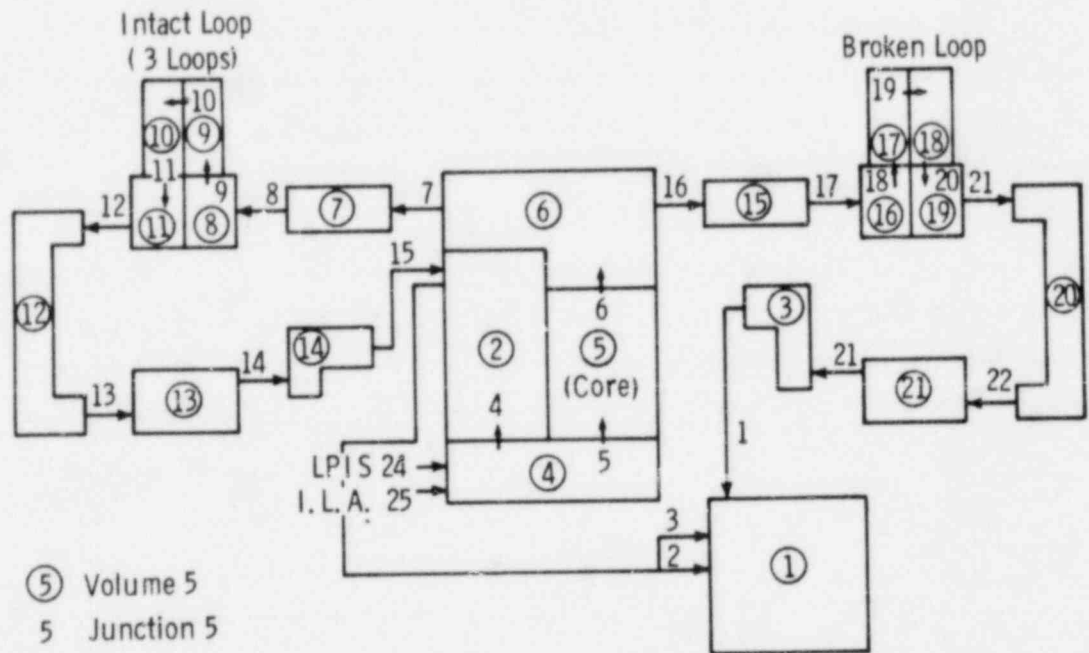


Figure 4-25. RELAP4/MOD5, FLOOD Nodalization

4.3.4 I.L. Accumulator

The location of the fill point of the IL accumulator (i.e., the sum of three individual accumulators) was investigated with regard to computational stability. The results from the blowdown calculation, UHL2G, indicated that this accumulator will contain a nontrivial amount of water (31,600 lbs @ 110 psia at the beginning of reflood. Physically, the IL accumulator and LPIS fills should be connected to volume 14 in Figure 4-25. However, several FLOOD nodalizations performed at other labs^{3 4} as well as by us, gave results that indicated that connecting these fills to the downcomer or lower plenum reduced instabilities. A substantial and sustained downcomer upflow has been observed with this nodalization. Figure 4-26 shows the junction flows from the lower plenum to the downcomer, J4, and the lower plenum to the core, J5. Both are defined as positive for upflow. After initial oscillations, the downcomer flow was approximately twice that of the core flow (IL accumulator fill on). This phenomenon is still under investigation.

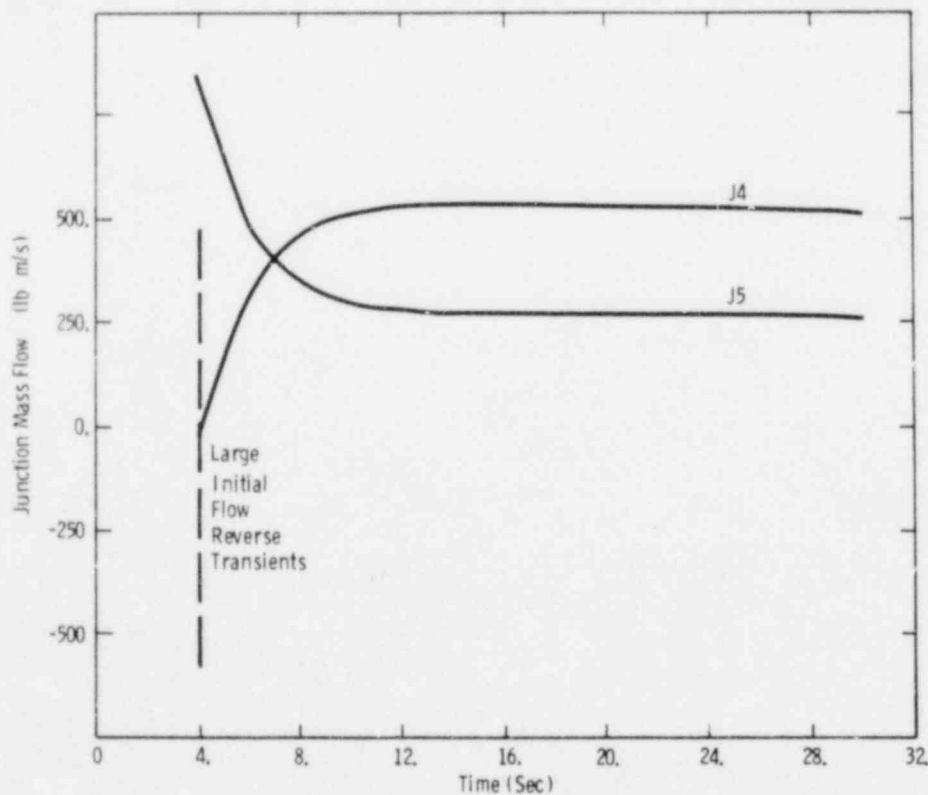


Figure 4-26. Lower Plenum to Downcomer (J4) and Lower Plenum to Core (J5) Junction Mass Flows

4.3.5 Upper Plenum

An analysis was performed concerning the initial condition of the upper plenum and the IL pump discharge line (volumes 6 and 14 in Figure 4-25). Previous quarterlies^{5 6} reported investigations of the effects of the initial water level of the upper plenum. The present investigation revealed that the initial upper plenum water level does not affect the stability of the calculation. This conclusion appears reasonable considering the use of a CRF model. That is, the core outlet junction flow was defined as the inlet flow times the CRF. Therefore, any water in the upper plenum had little effect on the core thermal-hydraulics.

4.3.6 FRAP

The missing LACE options⁷ to FRAP-T4 have been re-coded in a new copy of the code from INEL. This code will provide the input core heat slab temperatures and initial quench height to FLOOD.

4.3.7 Future Work

The investigation of the following items will be completed and reported in the next quarterly.

- An analysis of the W CRF model in light of new information and the NRC modification
- An analysis of the FLOOD heat transfer correlation
- The results from the core exit enthalpy option investigation
- The dependence of the core inlet flooding rate on the initial temperatures of the core and the state of the IL accumulator fill junction

4.4 TRAC Progress

4.4.1 Introduction

A very high priority was given by the NRC contract monitors to performing Semiscale MOD3 calculations with TRAC this quarter. The reason

for that high priority was a planned holdup in performing the Series 8 (UHI) Semiscale tests until a TRAC pretest predictive capability is established for that system. However, as will be discussed below, all of the calculations actually performed this quarter used the Series 7 (non-UHI) configuration. They were performed because the logical first step in generating a good pretest prediction of the Series 8 tests would be an accurate posttest prediction of the Series 7 data to verify the nodalization assumptions.

The original nodalization of the Semiscale MOD3 system was provided by J. J. Pyun, Q-6, LASL. Most of the Semiscale TRAC calculations performed at Sandia this quarter were performed (at the request of NRC) in direct support of LASL's modeling of test S-07-6 since they could not get enough time on their computers to run the problem on a short time frame basis. A few S-07-1 calculations were also continued from last quarter.⁷ The status of TRAC was changing rapidly during this period. Consequently, three different versions (20.3, 20.4 and 21.0) of TRAC were imported and used in performing the Semiscale calculations. Only version 21.0, which is TRAC-PIA, was an official release version.

One calculation for a full-scale, four-loop PWR was also performed with version 20.3 of the TRAC code this quarter.

4.4.2 S-07-6 Calculations

The S-07-6 calculations which were performed this quarter had a slightly different nodalization of the MOD3 system from the one used in the S-07-1 calculations reported last quarter. The basic difference was in the modeling of the downcomer distribution annulus. In the latest nodalization provided by LASL, the transition region of the distribution annulus was modeled as a tee rather than as part of the distribution annulus which is modeled as a vessel. This was apparently changed to avoid reduced time step problems caused by a thin downcomer annulus computational cell. Several nodalization errors discovered at Sandia (involving the break nozzle, the accumulators and the broken loop steam generator) were also corrected for the latest S-07-6 runs.

The changes in the nodalization required many separate runs to be made, with adjustments to friction factors, etc, in order to get a satisfactory steady-state solution. Severe complications were introduced into this process by the abnormal behavior calculated for the pressurizer. When the temperature of the liquid in the pressurizer was set at its proper value, vapor was slowly generated and then transported through the main piping system and vessel. The vapor generation was presumably caused by numerical noise which allowed tiny amounts of hot water from the pressurizer to mix with the colder circulating water in the loop and flash to vapor. It is uncertain why the vapor did not simply recondense. The solution ultimately determined by LASL for this problem was the setting of the pressurizer water temperature equal to the hot leg water temperature while the steady-state calculation was being performed and then resetting the pressurizer liquid temperature to the correct value when the transient was initiated.

After a reasonable steady-state solution was finally achieved, a blowdown transient calculation was performed which was run to about 18 s of transient time. The results were unsatisfactory, however, since the predicted downcomer behavior did not agree with the experimental data.

It should be noted that since LASL was responsible for the S-07-6 calculation, the Sandia contribution to the calculations was merely to provide all assistance possible to expedite the calculations. This included: consultation on possible nodalization errors and their solution; bringing up new versions of TRAC on the Sandia computer system and assisting in making the special code modifications required for the broken loop pump, the downcomer energy source, and some special graphics; setting up the actual card decks to perform the calculations and plot the results; and providing the necessary computing time. All of the decisions on the actual runs to be performed and interpretation of the results were made by LASL. Consequently, no further discussion of the S-07-6 results will be given here.

4.4.3 S-07-1 Calculations

The modeling of test S-07-1 was continued in the first part of this quarter. As discussed in the last quarterly report,⁷ it was being modeled because it was the only Series 7 test for which a complete set of data was available at the time the calculations were begun. Also, the basic nodalization was the same as for test S-07-6 which was of considerable interest.

Much of the work on the S-07-1 modeling involved checking the nodalization originally provided by LASL. Several discrepancies were identified and corrected, as mentioned in the S-07-6 discussion (Section 4.4.2). The concept of using a tee to model the bottom piece of the downcomer distribution annulus was also investigated for the S-07-1 nodalization. Several simple test calculations were run to determine what effect the angle between the primary and secondary tubes of the tee had on the calculated flow. Surprisingly, the effect of varying the angle was not very large, even though the angle was changed from 0° to 90°.

After the corrected nodalization was established, a steady state calculation and a short transient calculation (to about 20 s of transient time) were performed. These calculations were performed with version 20.3 of TRAC. The calculations ran fairly smoothly and no gross errors were detected, but no real comparison of the results with the data was ever made since the S-07-1 work was discontinued at that point. The reason for discontinuing was to allow increased emphasis to be placed on the S-07-6 calculations. Further, a S-07-1 calculation was deemed to be unnecessary if test S-07-6 could be correctly predicted.

4.4.4 Four-Loop PWR

As discussed last quarter,⁷ the sample PWR problem exhibited peculiar behavior with version 19.3 of TRAC. The sample problem was rerun this quarter with version 20.3 of TRAC. Peculiar behavior at the cold leg inlet pipes was again observed, at about 26 s into the transient. The problem was discussed with LASL personnel and they agreed the predicted behavior seemed to be unphysical. They suggested that the problem was

caused by the use of fully implicit primary tubes and semi-implicit secondary tubes of the main piping network tees.

Since the PWR sample problem deck being used was not LASL's normal sample problem deck, we obtained a copy of their current PWR sample problem deck to replace the one we had been using. Unfortunately, no further transient calculations on the full-scale, four-loop PWR problem were performed this quarter. However, as discussed in Section 3.6, a steady-state calculation was made near the end of the quarter with the new input data and the release version of TRAC-PLA.

4.5 References

¹Marshall Berman, ed, Light Water Reactor Safety Research Program Quarterly Report, July-September 1978, SAND79-0359, NUREG/CR-0661, (Albuquerque: Light Water Reactor Safety Department, Sandia Laboratories April 1979).

²Westinghouse Emergency Core Cooling System Evaluation Model Application to Plants Equipped With Upper Head Injection, WCAP-8479-P, Rev 2.

³EXXON Nuclear Company WREM-Based Generic PWR ECCS Evaluation Model (ENC-WREM-11), 4-Loop PWR With Ice Condenser Large Break Example Problem, XN-76-36 (August 1976).

⁴C. A. Dobbe, "Zion Reflood Plant Deck Results" (Idaho Falls: Idaho National Engineering Laboratory, nd). Internal report.

⁵D. A. Dahlgren, ed, Light Water Reactor Safety Research Program Quarterly Report October-December 1977, SAND78-0600, NUREG/CR-0307 (Albuquerque: Sandia Laboratories, June 1978).

⁶Light Water Reactor Safety Research Program Quarterly Report January-March 1978, SAND78-1511, NUREG/CR-0324 (Albuquerque: Sandia Laboratories October 1978).

⁷Light Water Reactor Safety Research Program Quarterly Report October-December 1978, SAND79-0820 (Albuquerque: Sandia Laboratories, July 1979).

5. Two-Phase Jet Loads

(D. T. Tomasko)

5.1 Summary

The purpose of this study is to develop an improved approximate engineering model to characterize two-phase jets emanating from circumferential or longitudinal breaks in a typical PWR piping system. This model would replace the currently used Moody model which assumes asymptotic jet expansion and thermodynamic equilibrium.

This quarterly report addresses the applicability of the last computer code TRAC-PLA to the two-phase jet problem and investigates the magnitude of the air-jet interaction using the Sandia Code CSQ.

The main conclusions of this quarter are summarized as follows:

- TRAC-PLA adequately predicts the thermalhydraulic conditions at the break site. These data can be used to predict steady-state impingement loads or can be used as input to a containment code such as BEACON/MOD2.
- Steady-state impingement loads obtained from TRAC-PLA data are in better agreement with Kraftwerk Union data than Moody Model impingement loads.
- TRAC-PLA steady-state impingement loads agree fairly well with proprietary Japanese data.
- Friction effects are very important in impingement load modeling.
- The air-jet interaction effect seems to be insignificant.

5.2 Break Flow Results Using TRAC-PIA

In carrying out the two-phase jet load program, two computer codes have been previously examined, CSQ and BEACON/MOD2.¹ This quarterly report discusses, in part, the feasibility of using the LASL computer code TRAC-PIA² to obtain pipe exit thermal-hydraulic boundary conditions which could be used to drive a containment code such as BEACON/MOD2, or to directly calculate steady-state impingement loads.

Figure 5-1 shows the TRAC-PIA component diagram used in modeling various Kraftwerk Union (KWU) Tests.³ These tests cover a wide range of initial conditions as shown in Table 5-1. A diagram of the KWU system is shown in Figure 5-2. Results obtained for test NW50-6 (nominal width 50 mm, Test 6) are shown in Figures 5-3 and 5-4.

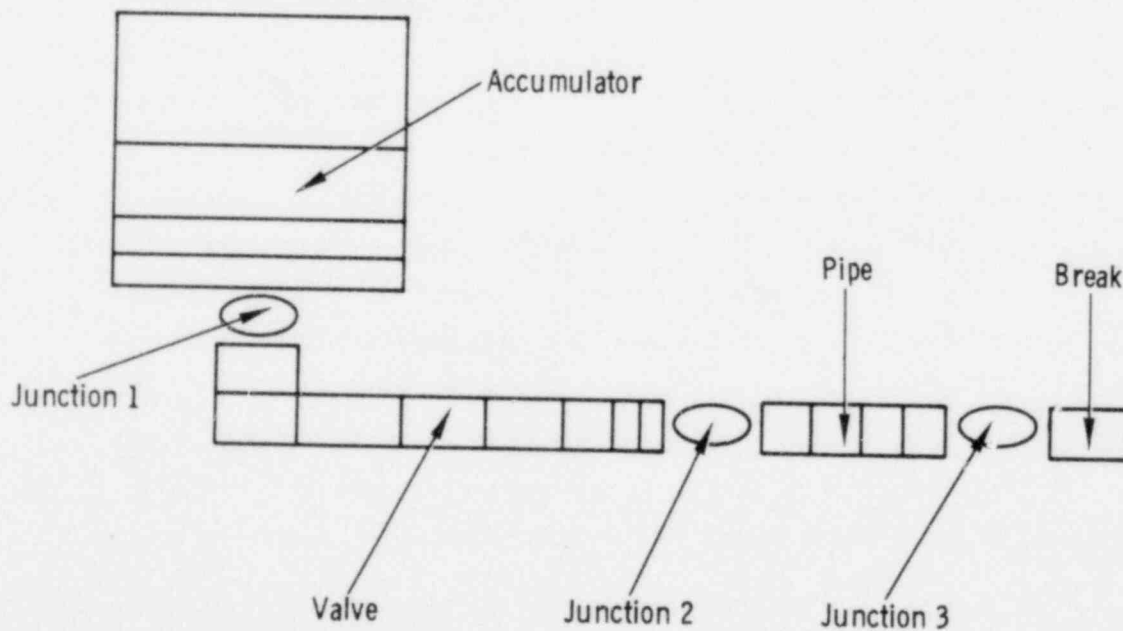


Figure 5-1. TRAC Four-Component Model for Initial Blowdown Studies

Experimental values are plotted as constants in time equal in magnitude to the measured steady-state-values (defined as that value for which a one second change in time didn't appreciably change the magnitude of the measurement). This was done because no transient data is available from KWU due to their 1 Hz sampling frequency. Table 5-II shows comparisons made between the TRAC-PIA results and the KWU steady-state measurements.

Fairly good agreement is seen for the break flows and exit pressures for NW 25 tests in which the coefficient of resistance is small (Table 5-III). For NW 50 and NW 65, the coefficients of resistance are high, and the TRAC-PIA frictionless model overpredicts the data. For NW 50, test 6, a model was constructed using constant friction. The results are seen to be in much better agreement with the data than the frictionless model.

One can conclude from Table 5-II that TRAC-PIA, in general, does a good job in predicting thermal-hydraulic break boundary conditions for KWU initial conditions (saturated blowdown) and that friction plays an important role in blowdown processes.

Current and future work with TRAC-PIA involves the following: determining how to best model friction effects; carrying out nodalization and L/D effect studies; and determining if the vessel component model can be used to simulate a containment structure necessary for detailed two-phase jet analyses.

TABLE 5-I
Initial Conditions for KWU Tests

<u>Test</u>	<u>Nozzle Diameter (mm)</u>	<u>Vessel Pressure (bars)</u>	<u>Vessel Temperature (°C)</u>
<u>NW 25</u>			
3	25	99.4	310.5
5	25	52.4	266.9
<u>NW 50</u>			
6	50	96.2	308.0
<u>NW 65</u>			
3	65	98.7	310.0
4	65	53.1	267.7

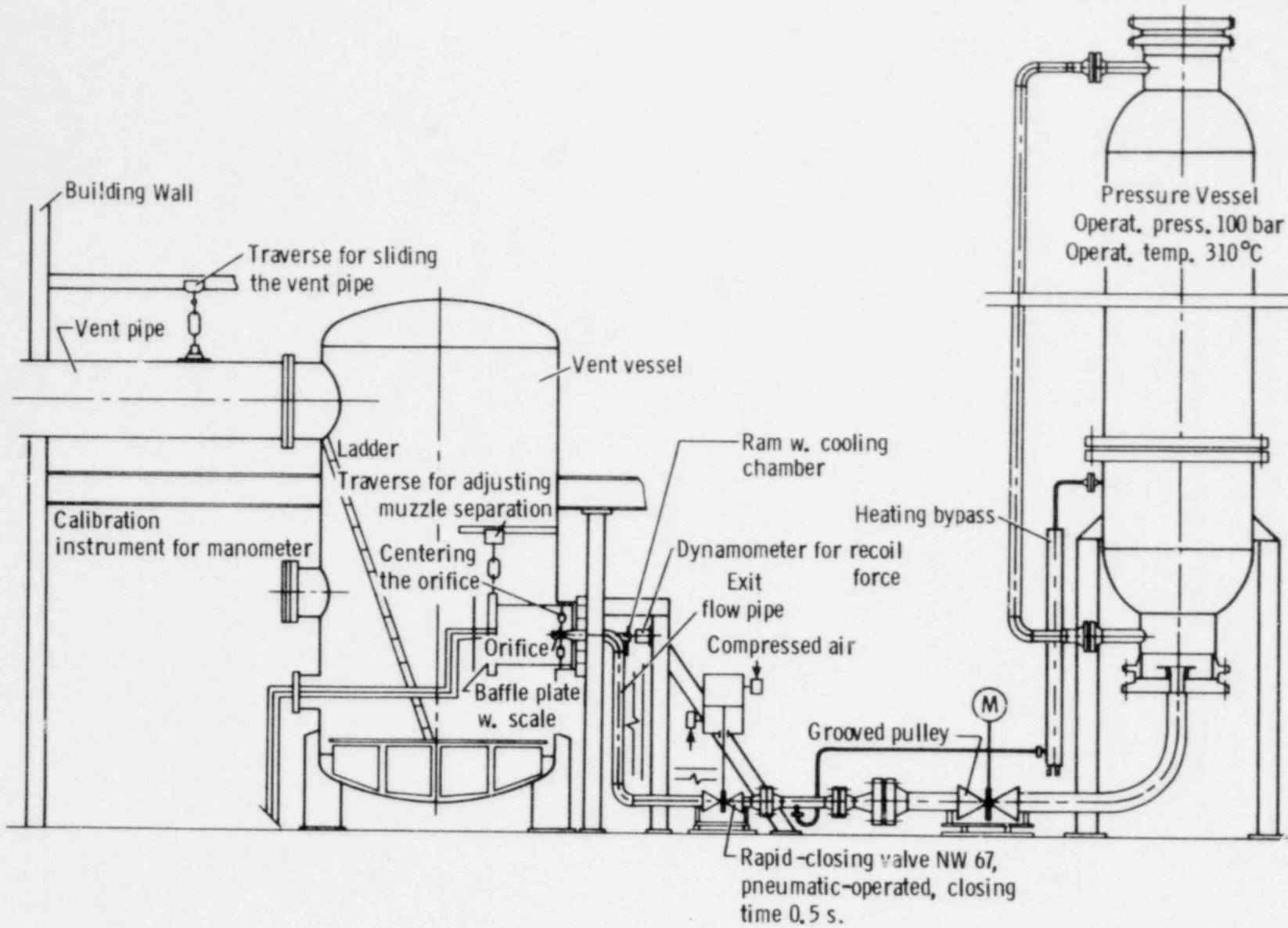


Figure 5-2. KWU Test Facility

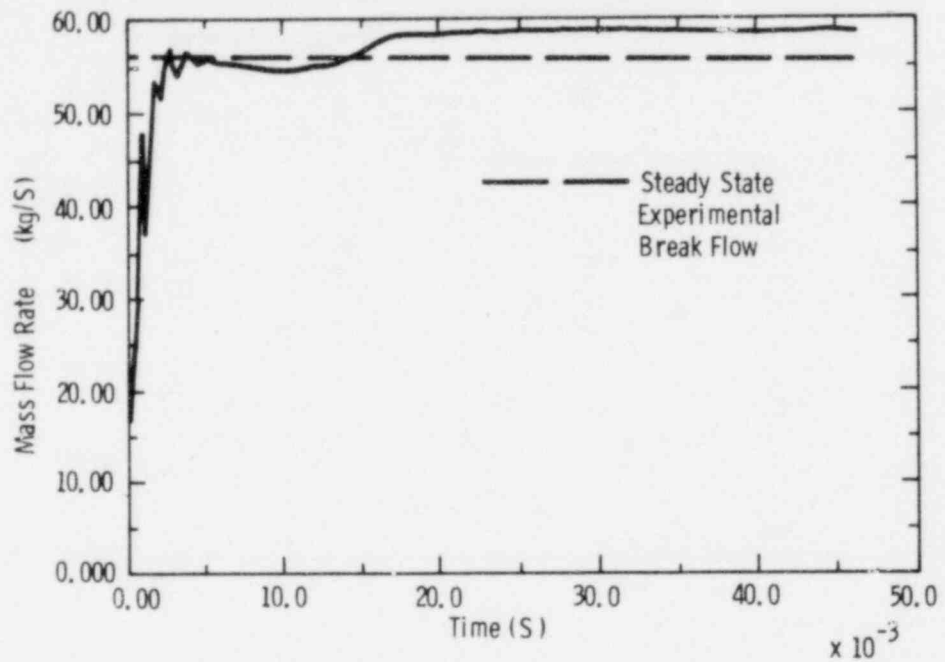


Figure 5-3. TRAC Break Flow for KWU NW 50, Test 6

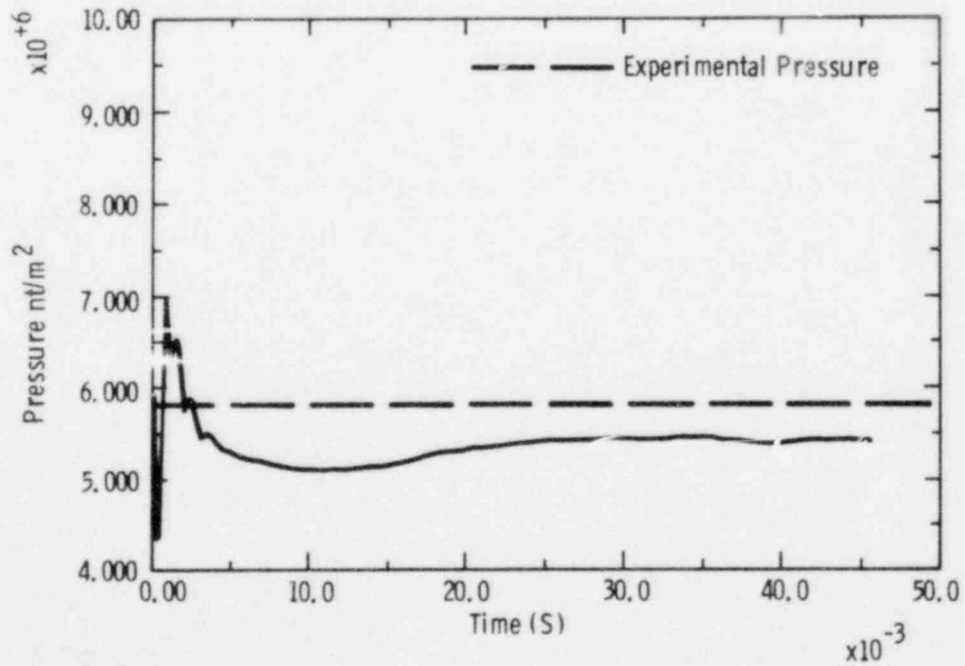


Figure 5-4. TRAC Break Pressure for KWU NW 50, Test 6

TABLE 5-II

TRAC-PIA and KWU Test Comparisons

Test	Break Flow (kg/s)		Exit Pressure (bars)		Steady-State Impingement Load (NT)				
	Exp	TRAC	Exp	TRAC	Exp	Exp	TRAC	Moody Model	
					(Measured Recoil) ^a	(Orifice Force)		Homogeneous Flow	Separated Flow
<u>NW 25</u>									
3	15.7	16.5	67.7	63	2520 ^b	5288	5080	6900	7300
5	12.2	10.2	36.0	32	2765 ^b	3145	2590	3000	3200
<u>NW 50</u>									
6	56.4	63.6 58 ^c	57.4	58.5 55 ^c	15428	19740	19070 17400 ^c	23600 20000 ^d	24900
<u>NW 65</u>									
3	75.4	106.9	51.7	58	26041	28233	32440	41000	42500
4	53.7	70.8	28.8	41	14518	16102	16600	19000	22000

^aRecoil force measured with strain gage of full scale = 50 kn (+2%) for all tests except those of NW 25 which had a full scale of 10 kn (+2.5%).

^bNW 25 recoil forces were obtained at the end of the blowdown tests and are smaller in magnitude due to falling pressure in the non-infinite pressure vessel.

^cModel with friction

^dUsing $fL/D = 0.81$

TABLE 5-III

Coefficients of Resistance for KWU Tests

<u>Test</u>	<u>Coefficient of Friction</u>
<u>NW 25</u>	
3	0.15
5	0.15
<u>NW 50</u>	
6	0.81
<u>NW 65</u>	
3	0.82
4	0.82

5.3 Steady-State Technique for Reaction Force

Using the principles of conservation of momentum, F. J. Moody has shown that the steady-state reaction force, F_N , and the net impingement force, R , for a discharging pipe segment can be written:

$$F_N = R = (P_T - P_\infty)A_T + \dot{m}_T V_T$$

where

P_T = exit discharge pressure

P_∞ = external ambient pressure

A_T = discharge area

V_T = throat mixture velocity

$\dot{m}_T = \rho_T V_T A_T$ and ρ_T = throat mixture density.

Under steady-state conditions, the impingement load and the pipe reaction force can be readily obtained if the exit thermal-hydraulic conditions are known.

The next section of this report compares TRAC-PIA steady-state impingement loads to experimental data obtained from Kraftwerk Union and the Japanese Atomic Energy Research Institute (JAERI).

5.4 Steady-State TRAC Results for JAERI and KWU Data

Several TRAC-PIA computer runs were made with the use of the four-component model shown in Figure 5-1 and the initial conditions given in Table 5-I. Time dependent impingement loads obtained from TRAC-PIA data are shown in Figures 5-5 through 5-9 for the KWU tests (KWU data is again plotted as steady-state constants) and in Figures 5-10 through 5-13 for the JAERI tests. Since the Japanese data are proprietary, initial conditions are not given and the impingement load graphs are shown without numbered scales.

Comparisons between KWU data and results obtained with TRAC-PIA are shown in Figures 5-5 through 5-9, and in Table 5-II. The TRAC-PIA values used for these comparisons were chosen conservatively at the point of maximum difference with the measured value. Actual errors may be somewhat less. Moody steady-state improvement loads outlined by graphical techniques and Figure 5-7 of Reference 4 (both homogeneous and separated flow models with $fL/D=0$) are also shown in this Table.

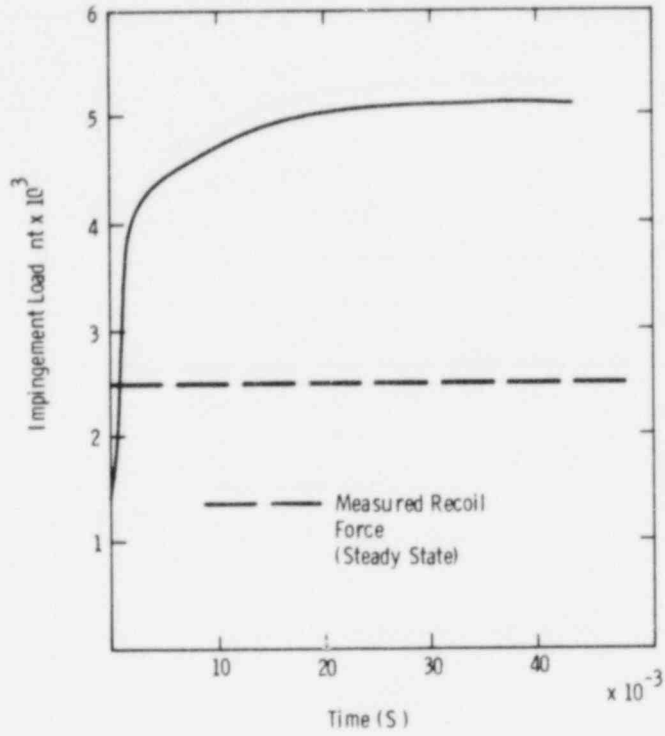


Figure 5-5. TRAC Results for KWU NW 25, Test 3

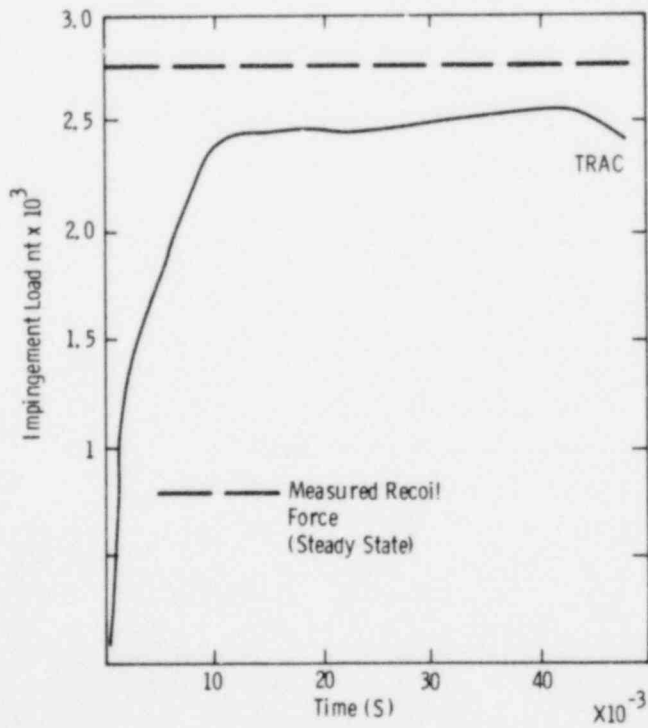


Figure 5-6. TRAC Results for KWU NW 25, Test 5

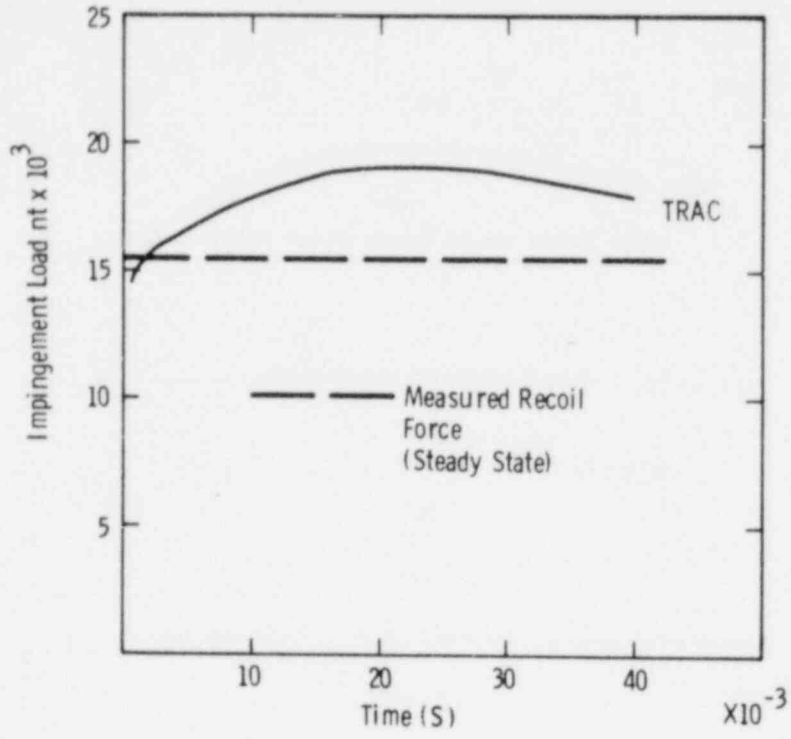


Figure 5-7. TRAC Results for KWU NW 50, Test 6

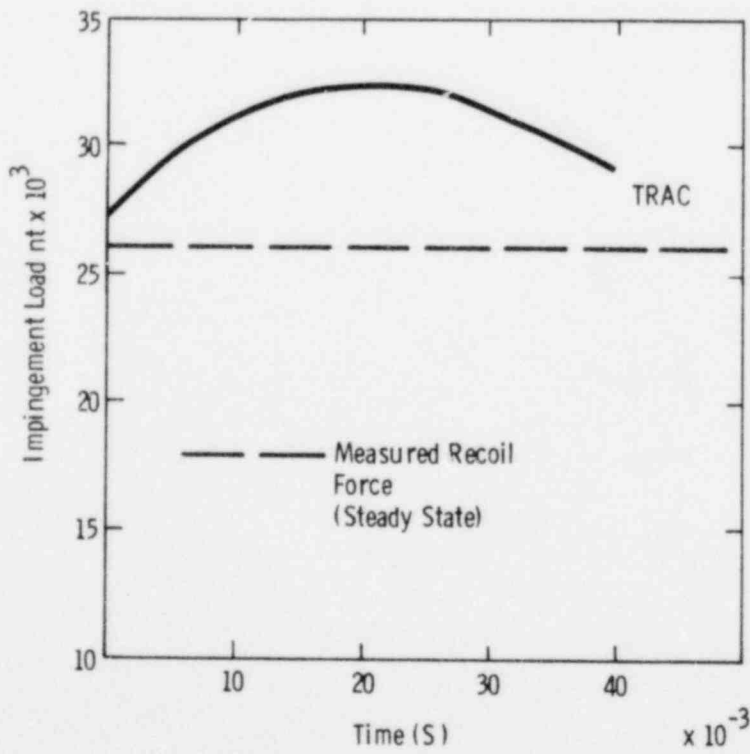


Figure 5-8. TRAC Results for KWU NW 65, Test 3

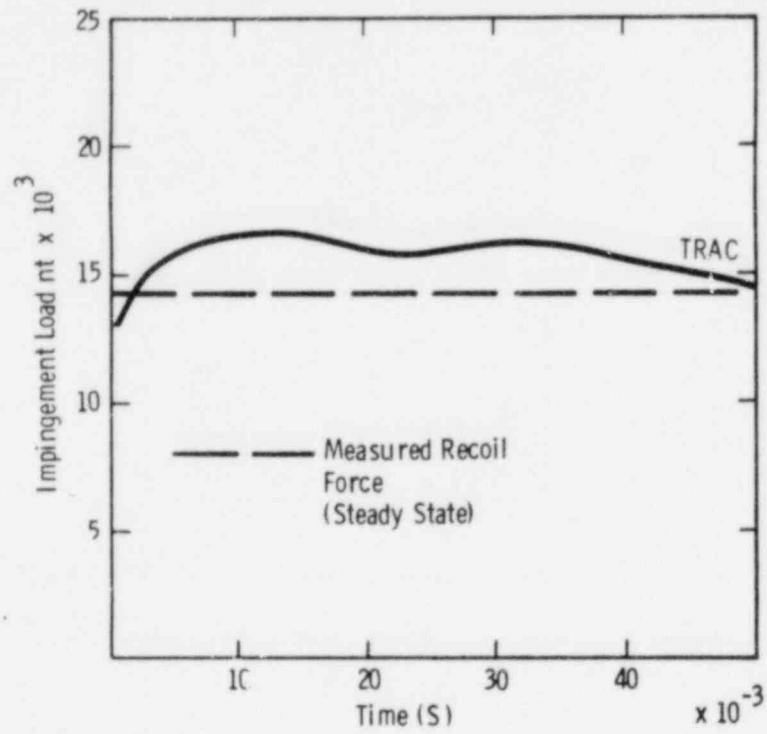


Figure 5-9. TRAC Results for KWU NW 65, Test 4

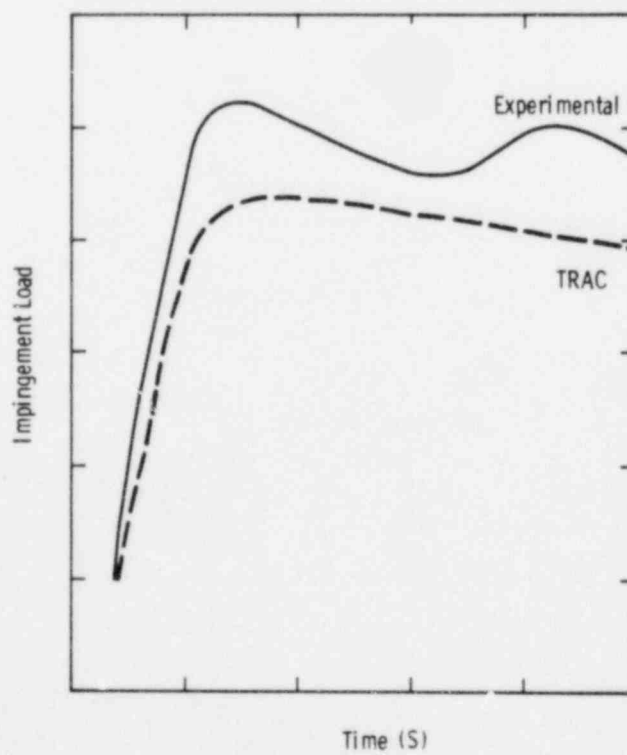


Figure 5-10. TRAC Comparison to JAERI Data, Test 1

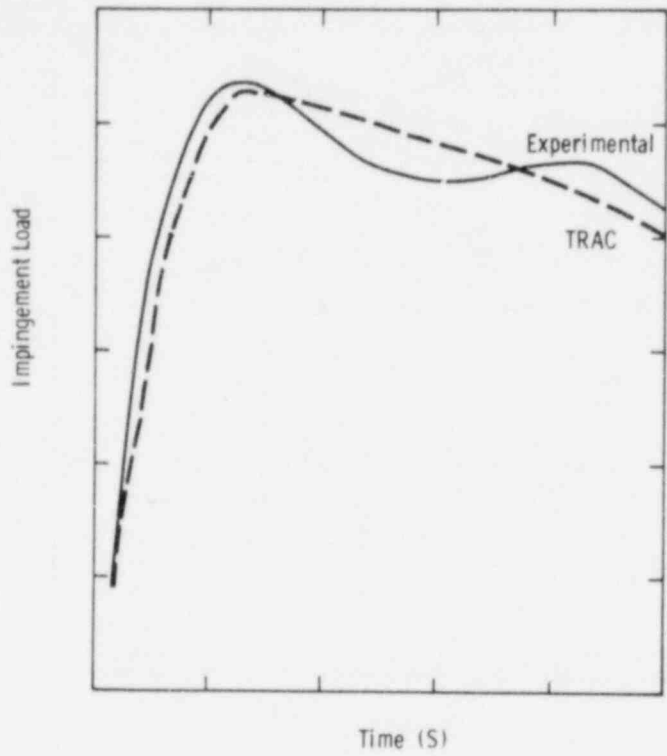


Figure 5-11. TRAC Comparison to JAERI Data, Test 2

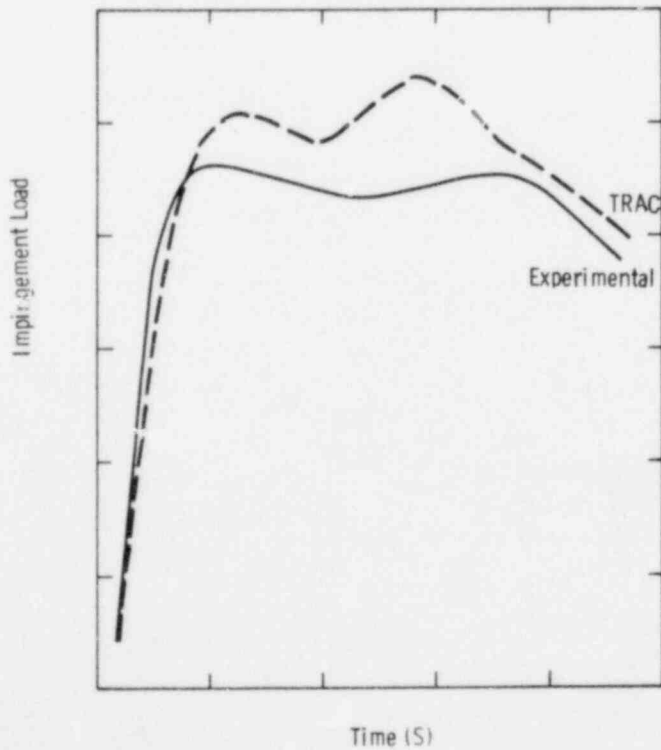


Figure 5-12. TRAC Comparison to JAERI Data, Test 3

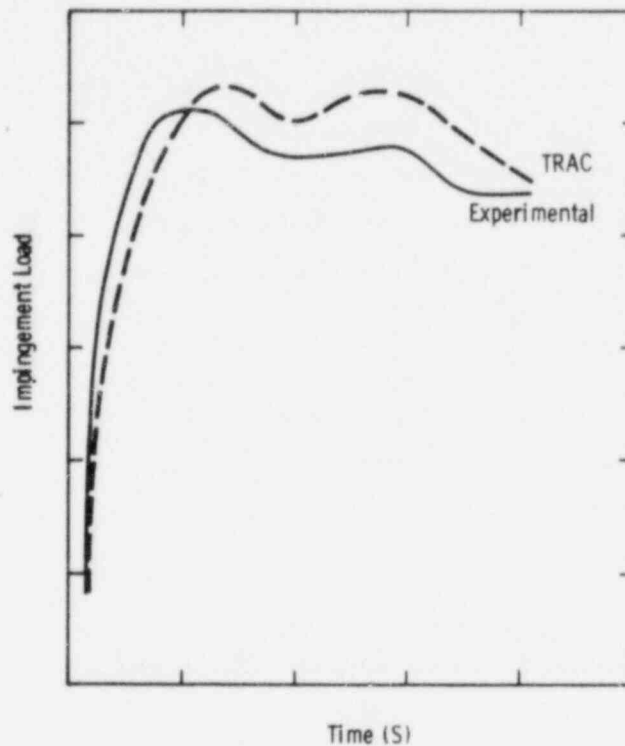


Figure 5-13. TRAC Comparison to JAERI Data, Test 4

Examination of Table 5-II permits several interesting observations to be made:

- The Moody separated flow model consistently predicted the largest impingement loads. This is the model recommended for use in Reference 4.
- The Moody homogeneous flow model produced impingement loads smaller than the separated flow model, but still, in general, significantly larger than the measured recoil forces.
- The measured recoil force was in all cases less than the experimental orifice force, which is the force obtained using experimental exit conditions (pressure, mass flow, and velocity). This result occurred

because the exit pressure used in the orifice force calculation was obtained up to 6 cm upstream of the actual exit location (Table 5-IV). The pressure drop in 6 cm clearly produced a significant variation in the orifice force. If accurately measured, the orifice force and recoil force should be equal under steady-state conditions.

- The TRAC-PIA results, in general, lie between the measured recoil force and the Moody homogeneous flow model.
- The worst agreement between TRAC-PIA and the experimental recoil force occurred for NW 65, test 3 (large diameter, high pressure, and high coefficient of friction). This was also true for the Moody model. (Experimental impingement loads for NW 25 tests are in error due to measurement at the end of blowdown-falling system pressure and should be disregarded.)
- Including friction in the TRAC-PIA model considerably improved the agreement with the experimental data (NW 50, test 6).

TABLE 5-IV

Pressure Measurement Location for KWU Tests

<u>Test</u>	<u>Distance Upstream from Exit to Measuring Point (cm)</u>
<u>NW 25</u>	
3	6.0
5	6.0
<u>NW 50</u>	
6	2.0
<u>NW 65</u>	
3	6.0
4	6.0

Assuming an $fL/D = 0.81$, which is the value of the coefficient of friction for NW 50 test 6, also considerably improved the Moody steady-state value. Based on the above observations, one can conclude that the TRAC-PIA results are, in general, in better agreement with experimental data than either of the two Moody models. In addition, one can readily see the importance of correctly modeling the effects of friction.

Figures 5-10 through 5-13 compare the JAERI data and the TRAC-PIA results. As with the KWU tests, the TRAC-PIA steady-state values are about 10% higher. This difference is probably due to frictional effects. Steady-state TRAC-PIA values were chosen conservatively at the maximum difference point. Actual errors may be lower. (System volumes were not available for this study. Impingement load fall off is probably incorrect.)

In conclusion, for steady-state analysis, TRAC-PIA predicts the impingement load of a two-phase jet fairly well. Also, the need for additional work on friction modeling is apparent.

5.5 Air-Jet Interaction Using CSQ

The interaction effect of air with a two-phase jet was evaluated with the computer code CSQ⁵, the model shown in Figure 5-14, and the initial conditions of KWU NW 50, test 6 (Table 5-1). The evaluation was performed by varying the air density by a factor of 5 under constant pressure. The results of this study are shown in Figure 5-15. From this figure it is evident that the air-density variation affected only the outer wings of the plate pressure profile (at distances greater than 12 cm), with the higher density air producing a flatter pressure profile. Future analysis on two-phase jets can, therefore, ignore variations in containment material density.

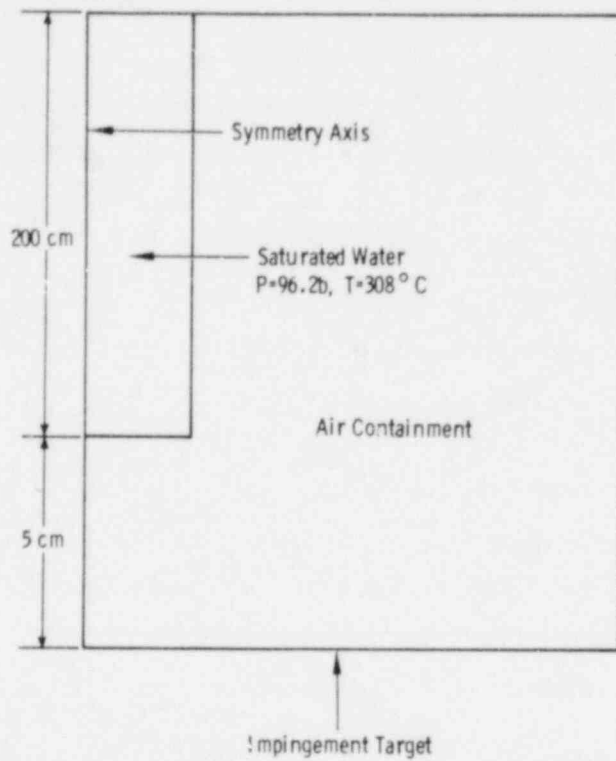


Figure 5-14. CSQ Model for KWU Test Facility

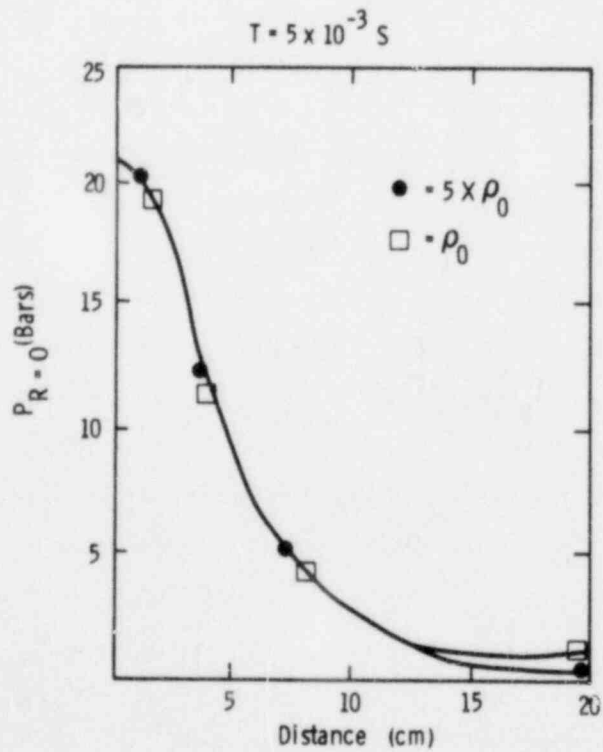


Figure 5-15. Effect of Air Density on Plate Pressure

5.6 Proposed Future Work

Future work in the area of two-phase jet loads involves the following:

1. Performing a friction effects study with TRAC-PIA
2. Determining if TRAC-PIA can be used in a blowdown-containment mode
3. Modeling other systems with TRAC-PIA (Battelle-Frankfurt RS-50)
4. Performing nodalization and L/D effect studies with TRAC-PIA
5. Using TRAC-PIA data as input to drive BACON/MOD2 in a containment mode
6. Continuing the analysis effort, using CSQ

5.7 References

¹M. Berman, ed, Light Water Reactor Safety Research Quarterly Report October-December 1978, SAND78-0820 (Albuquerque: Sandia Laboratories, Light Water Reactor Safety Department, August 1979).

²TRAC-P1: An Advanced Best-Estimate Computer Program for PWR LOCA Analysis Vol. 1. Methods, Models, User Information and Programming Details, LA-7279-MS, (Los Alamos: Los Alamos Scientific Laboratory, Safety Code Development Group Energy Division, June 1978).

³R. Eichler et al, Studies on Critical Two-Phase Flow, NRC-477 (Washington: US Nuclear Regulatory Commission, September 1978).

⁴F. J. Moody, "Fluid Reaction and Impingement Loads," Specialty Conference on Structural Design of Nuclear Plant Facilities, Vol. 1 (Chicago Ill: np, December 1973).

⁵S. L. Thompson, CSQ - A Two-Dimensional Hydrodynamic Program with Energy Flow and Material Strength, SAND74-0122 (Albuquerque: Sandia Laboratories, August 1975).

DISTRIBUTION

US Nuclear Regulatory Commission
(360 copies for R3)
Division of Document Control
Distribution Services Branch
7920 Norfolk Ave
Bethesda, MD 20014

US Nuclear Regulatory Commission (6)
Office of Nuclear Regulatory Research
Washington, DC 20555
Attn: W. C. Lyon
N. Zuber
S. Fabric
C. E. Johnson
R. R. Sherry
M. Vagins

US Nuclear Regulatory Commission (3)
Division of Systems Safety
Office of Nuclear Reactor Regulation
Washington, DC 20555
Attn: B. Sheron
N. Lauben
E. Throm

US Department of Energy
Operational Safety Division
Albuquerque Operations Office
P.O. Box 5400
Albuquerque, NM 87185
Attn: J. R. Roeder, Director

Westinghouse Electric Corporation
Research and Development Center
Churchill Boro
Pittsburgh, PA 15235
Attn: M. Mazumdar
Mathematics Department

Florida International University
Department of Statistics
Tamiami Trail
Miami, FL 33144
Attn: S. S. Shapiro

EG&G - Idaho, Inc. (2)
P.O. Box 1625
Idaho Falls, ID 83401
Attn: N. D. Cox
D. M. Snider

Electric Power Research Institute
3112 Hillview Avenue
Palo Alto, CA 94304
Attn: J. Carey

Offshore Power System
8000 Arlington Expressway
Box 8000
Jacksonville, FL 32211
Attn: D. H. Walker

University of Wisconsin
Nuclear Engineering Dept
Madison, WI 53706
Attn: S. Abdul-Kalik

Northwestern University
Chemical Engineering Dept
Evanston, IL 60201
Attn: S. G. Bankoff

Westinghouse Advanced Reactor Division
P.O. Box 158
Madison, PA 15663
Attn: L. E. Strawbridge

Westinghouse Electric Corp. (2)
Bettis Atomic Power Laboratory
P.O. Box 79
West Mifflin, PA 15122
Attn: W. D. Peterson
F. W. Lincoln

Westinghouse Electric Corp. (2)
Nuclear Energy Systems
P.O. Box 355
Pittsburgh, PA 15230
Attn: R. P. Vijuk
M. Y. Young

Los Alamos Scientific Laboratory (2)
P.O. Box 1663
Los Alamos, NM 87545
Attn: M. McKay
J. Jackson

400 C. Winter
1200 L. D. Smith
1223 R. G. Easterling
1223 I. J. Hall

DISTRIBUTION (cont)

1537 N. R. Keltner
2514 D. E. Mitchell
4400 A. W. Snyder
4410 D. J. McCloskey
4412 J. W. Hickman
4420 J. V. Walker
4422 R. L. Coats
4422 D. W. Varela
4423 J. E. Powell
4425 W. J. Camp
4440 G. R. Otey
4441 M. Berman (10)
4441 L. D. Buxton
4441 R. K. Byers
4441 R. K. Cole, Jr.
4441 B. W. Burnham
4441 D. Tomasko
4441 J. F. Muir
4442 W. A. Von Rieseemann
4443 D. A. Dahlgren
4450 J. A. Reuscher
4533 B. D. Zak
4550 R. M. Jefferson
4732 H. J. Sutherland
5131 W. B. Benedick
5511 D. F. McVey
5511 M. L. Corradini
5512 D. W. Larson
5520 T. B. Lane
5530 W. Herrmann
5532 B. M. Butcher
5534 J. E. Smaardyk
5623 B. M. Bulmer
5641 G. P. Steck
5830 M. J. Davis
5836 L. S. Nelson
5831 N. J. Magnani
5836 D. A. Powers
5836 F. J. Zanner
5846 E. K. Beauchamp
5846 R. A. Sallach
8266 E. A. Aas
3141 T. L. Werner (5)
3151 W. L. Garner (3)
For: DOE/TIC (Unlimited Release)
3154-3 R. P. Campbell (25)
For Distribution to NTIS